UNIVERSITÀ DEGLI STUDI DI MILANO

PhD School in Physics, Astrophysics and Applied Physics

Search for Non-Standard Neutrino Interactions with large-volume liquid scintillator detectors

Cycle XXXI-SSD FIS/04

Supervisor: Professor Lino Miramonti

Co-supervisors: Professor A.G. Olshevskiy
Ph.D. O. Yu. Smirnov

Director of the PhD School: Professor Matteo Paris

Doctoral thesis
by Andrey Formozov

Academic Year 2018/2019

Commission of the final examination:

PhD Thesis Referees:
Prof. Ph.D. Francesco Vissani, D.Sc. Bayarto K. Lubsandorzhiev

Members of the commission:
Prof. Ph.D. Ezio Previtali, Prof. Ph.D. Lino Miramonti, Prof. Ph.D. Giuseppe Salamanna

Final examination:

May, 2019

Università degli Studi di Milano, Dipartimento di Fisica, Milano, Italy

MIUR subjects: FIS/04

PACS: 14.60.Pq, 29.40.Mc, 23.40.Bw, 25.30.Pt, 26.65.+t, 24.80.+y, 25.60.Dz, 12.60.Cn, 13.15.+g, 13.85.Dz, 14.60.St, 02.70.Uu, 29.40.-n, 81.20.Ym, 78.40.-q.

Contents

List of Figures

List of Tables

Abstract

Even though electroweak part of the Standard Model passed decades of testing and precision measurements, there is still a space for the presence of new physics. In particular, the neutrino sector in the last years has been reaching the level of precision oscillometry. However, the current data are not able to exclude many possible extended scenarios, in which new interactions comparable with the standard ones are still possible.

This work is dedicated to beyond-Standard-Model interactions of neutrino and electron called Non-Standard Interactions or shortly NSI. Analogously to standard electroweak interactions, NSI could be charged current (CC) and neutral current (NC) type. Usually, in analyses of experiments, NC and CC NSI are considered separately, and I follow this strategy in the course of this work.

Global search for NSI involves almost all experimental approaches of neutrino physics and goes far beyond the scope of this work. Here, instead, I look at the problem through the prism of the large-scale liquid scintillator experiments and confine the investigation to the search for NC NSI with solar neutrinos. In addition, I review CC NSI with reactor neutrinos at medium baseline.

As a contribution into upcoming JUNO experiment, I investigate liquid scintillator energy response and radiopurity, which are essential for the successful realization of solar and reactor neutrino physics programs and, therefore, for NC and CC NSI search. I analyze in detail non-linearity and energy resolution of liquid scintillator. I develop an experimental Compton coincidence technique with High Pure Germanium gamma spectrometer, provide a conservative measurement of the Birks' ionization quenching constant kB and discuss problems related to its measurement. Throughout the study, I also formulate the optimal characteristics of the experimental apparatus for this improvement.

The ultimate goal of this investigation is separating intrinsic energy resolution, which was never yet robustly measured for liquid organic scintillators. Intrinsic energy resolution may have an impact on the energy response of the new generation large liquid scintillator detectors such as JUNO and have to be carefully investigated.

Applying single photon counting technique, I perform a calibration of PMT charge scale and set apart statistical term from the total liquid scintillator energy resolution. Remaining term significantly differs from zero, indicating the presence of additional contribution associated with the intrinsic energy resolution. As an outlook, the precise estimation of the light collection should be conducted in order to ensure that its contribution is not significant to mimic the observed intrinsic resolution effect.

The analysis of the radiopurity of the liquid scintillator showed that it is close to the one demanded for reactor neutrino program and CC-NSI search. Still, an improvement of purification procedure is necessary to fulfill solar neutrino program requirements for NC NSI search.

Finally, I place the limits to NC NSI $\varepsilon_e^{L/R}$ and $\varepsilon_\tau^{L/R}$ parameters with the Phase II data of Borexino experiment. The limits are quite stringent and compatible with other experiments. The best up-to-date limit to ε_e^L is obtained. The allowed regions could be further significantly reduced by incorporating the current result in a global analysis for $\varepsilon_e^{L/R}$ and $\varepsilon_\tau^{L/R}$. Besides, the same analysis approach is used to measure $\sin^2\theta$ with a precision comparable with reactor neutrino experiments and place the most robust limit on the probability of $\nu_e - \bar{\nu}_e$ conversion in the Sun for solar neutrinos with energies $E_\nu < 1.8$ MeV. I conclude with deliberation on the applicability of solar neutrino NC NSI approach for current JUNO detector configuration.

CHAPTER 1

Theoretical and experimental overview

Neutrino physics and its role in the Standard Model of particle physics

The history of neutrino has many bright moments. In 1914 when experiments of Chadwick demonstrated that the β-ray spectrum was continuous and not monochromatic as it was expected from the kinematics of two-body decay. This event was quite remarkable for the scientific community at that time. It happened in coincidence with the intensive development of quantum mechanics fundamentals and many attempts were made to build a consisted theory of the phenomenon by applying new-coming theory. To doubt the law conservation of energy and momentum was a natural way to resolve the puzzling phenomenon (Ref. [26]). To address the problem in 1930 W. Pauli proposed (Ref. [27]) the existence of a new particle emitted together with an electron which he called "neutron". It should be neutral and have spin 1/2 to conserve electric charge and angular momentum, correspondingly. In principle, it could be a massive particle though with a mass small enough not to be easily visible in the spectral shape of β-decay. The solution was proposed; however it was not clear how this hypothesis could be probed experimentally because of a tiny cross section of hypothesized particle. The ideas of W. Pauli got further development in the work of E. Fermi: the theory of β-decay (Ref. [28]), later extended by G. Gamow and E. Teller. E. Fermi renamed the "neutron" to neutrino when the actual neutron was discovered by J. Chadwick in 1932. Based β-decay theory H.Bethe and R.Peierls estimated the cross section of interaction of neutrino with matter that was found extremely small $\sigma < 10^{-44}$ cm^2 (Ref. [29]). "It is therefore absolutely impossible to observe processes of this kind with the neutrinos created in nuclear transformations" a fair conclusion was derived by authors. The development of the experimental techniques, the invention of nuclear reactors and the progress in neutron physics made neutrino detection much more feasible, and a suitable experiment was proposed in 1953 by F.Reines and C.L. Cowan (Ref. [30]). Pioneering work of these physicists and their successful detection of neutrino opened an era of *experimental neutrino physics*.

The pace of science is fast: the discovery of parity-non-conservation (Ref. [31] and [32]) revolutionized understanding of fundamental interactions (Ref. [33]) and further experimental and theoretical studies lead to the creation of modern electroweak theory (Ref. [34], [35] and [36]). This theory precisely describes all observed electromagnetic and weak phenomena and, united with quantum chromodynamics, forms the framework of the Standard Model.

The observation of the neutral weak current (Ref. [37]) and the discovery of the intermediate vector bosons W and Z (Ref. [38] and [39]) were the triumph of the theory (Ref. [33]). Finally, the recent discovery of the Higgs boson completed experimental prove of the model (Ref. [40] and [41]).

In parallel to the development of the standard model, unexpectedly, a new class of phenomena appeared. After the discovery of oscillations of neutral kaons B. Pontecorvo came with the idea of possible oscillations of leptons (Ref. [42], Ref. [43]). He considered muonium-antimuonium transition and mentioned a possibility of the neutrino oscillations. These ideas get development in his further work (Ref. [44]). At that time only one type of neutrino was known. B. Pontecorvo suggested *the existence of another type of weak interaction* which does not conserve the lepton number. The important conclusion of this paper was that the effect could not be visible in the laboratory due to a large value of oscillation length, "but will certainly occur, at least, on an astronomic scale." In 1967 B.Pontecorvo published the second paper on neutrino oscillations (Ref.[45]). In this paper, he discussed flavor neutrino oscillations $\nu_\mu \nu_e$ and also oscillations between flavor and sterile neutrinos. In this paper, solar neutrino oscillations were considered. Even before the first results of the Davis' solar neutrino experiment appeared, B.Pontecorvo pointed out that because of neutrino oscillations the flux of the solar electron neutrinos could be smaller than the expected one. Thus, he anticipated the solar neutrino problem that was not long in coming. In the late '60s, Davis performed ClAr experiment [1] Homestake to measure the solar neutrino flux. The detector was counting only one-third of the predicted neutrino flux from the Sun. Further development of the theory of oscillations by L.Wolfenstein (Ref. [46]), S.Mikheyev and A. Smirnov (Ref. [47]) led to the full explanation of the solar neutrino problem by matter effect and resonance enhancement of oscillations. Several scenarios were possible within the neutrino oscillation framework though. Moreover, neutrino oscillations were not the only explanation of the observed phenomena. Decades of experimental and theoretical investigation had passed before the unambiguous discovery of neutrino oscillations in the atmospheric (Ref. [48]), solar (Ref. [49]) and reactor neutrino experiments (Ref. [50]) was made.

Electroweak theory

It was well-established that local fermion interactions describe the weak interactions of leptons and quarks. Let us consider muon decay in a framework of the theory of Fermi:

$$\mu \to e^- + \bar{\nu}_e + \nu_\mu \tag{1.1}$$

The decay Lagrangian density could be represented as a multiplication of two fermion currents, where fermion current is a difference of vector and axial currents $(V-A)\times(V-A)$:

$$\mathcal{L}_W = -\frac{G_F}{\sqrt{2}}\bar{\nu}_\mu \gamma^\alpha (1-\gamma_5)\mu \bar{e}\gamma_\alpha (1-\gamma_5)\nu_e \tag{1.2}$$

where $G_F \approx 10^{-5}/m_p^2 \approx (1/300\,\mathrm{GeV})^2$ is a Fermi constant characterizing the strength of interaction. The operator (1.2) describes a large amount of observed processes of scattering and decays of leptons and quarks.

This theory is not renormalizable, since the constant G_F is neither dimensionless or have a dimension of positive power in energy. Being successful on tree level, the theory does not provide any framework for radiative correction calculations (Ref. [51])

In the way the electrodynamics does, one could postulate the interaction by exchanging a boson:

---

[1] also originally proposed by Pontecorvo

$$\mathcal{L}_W = -\frac{g}{2\sqrt{2}}[\bar{\nu}_\mu \gamma_\alpha (1+\gamma_5)\mu + \bar{e}\gamma_\alpha(1+\gamma_5)\nu_e]W^-_\alpha \tag{1.3}$$

To be consistent with Fermi theory we should suppose intermediate vector boson W_α to be heavy. At low energies the propagator of W boson became $1/(k^2 - M_W^2) \to 1/(-M_W^2)$.

Therefore comparing two relations one can get

$$\frac{G_F}{\sqrt{2}} = \frac{g^2}{8M_W^2} \tag{1.4}$$

In this case, the problem with renormalization disappeared since the constant g is dimensionless. However, it appears again if one consider the Lagrangian density of the vector field with a massive term $\frac{1}{2}M^2 A_\mu^2$: in this case the longitudinal polarization of the boson became singular. A straightforward approach to introduce mass to a vector boson does not work.

The alternative way to give mass to vector boson is very similar to the Meissner effect in superconductors that was developed by Ginsburg and Landau (Ref. [51], [52]). They introduce a scalar "order parameter" in addition to a photon field whose nonzero expectation value gives mass to a photon in superconductor. This mechanism was called $SU(2)$ spontaneous symmetry breaking.

Let us introduce scalar doublet $\phi = (\phi_1, \phi_2)$ and consider the following Lagrangian density:

$$\mathcal{L} = |D_\mu \phi|^2 - \frac{1}{2}\lambda^2[\phi^+\phi - \eta]^2 - \frac{1}{2}TrG^2_{\mu\nu} \tag{1.5}$$

where $D_\mu = \partial_\mu + igA_\mu$ - covariant derivative, $G_{\mu\nu} = \partial_\mu A_\nu - \partial_\nu A_\mu - ig[A_\mu, A_\nu]$ is a kinetic term, tensor of the vector Yang-Mills field.

Expanding the Lagrangian density (1.5) with:

$\phi = \begin{pmatrix} 0 \\ \frac{\eta+\xi(x)}{\sqrt{2}} \end{pmatrix}$

for massive terms one gets:

$$\Delta\mathcal{L} = \frac{1}{2}g^2\eta^2\frac{1}{4}[(A^1_\mu)^2 + (A^2_\mu)^2 + (A^3_\mu)^2] \tag{1.6}$$

$$M_{A^1} = M_{A^2} = M_{A^3} = \frac{g\eta}{2} \tag{1.7}$$

There is no massless field anymore. Now there are three massive vector field with the same mass and scalar Higgs boson ξ with a mass defined by a constant λ.

Electroweak theory of Glashow-Weinberg-Salam is based on the local symmetry $SU(2)_L \otimes U(1)$.

Covariant derivative could be written as:

$$D_\mu = \partial_\mu - igA^i_\mu T^i - ig' B_\mu \frac{Y}{2} \tag{1.8}$$

where g is a charge in $SU(2)$ group, g' in $U(1)$ and Y - is hypercharge if the .

Scalar sector of the theory consists of isodoublet of Higgs fields:

$$H = \begin{pmatrix} H^+ \\ H^0 \end{pmatrix} \tag{1.9}$$

with Lagrangian density

$$\mathcal{L} = |D_\mu H|^2 - \frac{1}{2}\lambda^2[H^+H - \frac{\eta^2}{2}]^2 \tag{1.10}$$

that looks similar to (1.5) with covariant derivative (1.8). The mass of the only one scalar particle in the theory, the Higgs boson, is $M_H = \lambda\eta$.

The Lagrangian density of the vector boson is a sum of the kinetic term such as $G_{\mu\nu}$ and massive terms that we get from (1.8). Massive terms naturally gives us the relations for the $W\pm$, Z and γ bosons:

$$W^\pm = \frac{A_1 \mp iA_2}{\sqrt{2}}, M_W = \frac{g\eta}{2} \tag{1.11}$$

$$Z = \frac{gA_3 - g'B}{\bar{g}}, M_z = \frac{\bar{g}\eta}{2} \tag{1.12}$$

$$\gamma = \frac{g'A_3 + gB}{\bar{g}}, M_\gamma = 0 \tag{1.13}$$

$$\bar{g} = \sqrt{g^2 + {g'}^2} \tag{1.14}$$

One can see from these relations that Z and γ are mixed with some angle θ_W (called Weinberg) with respect to the fields A_1 and A_2.

$$\sin\theta_W = g'/\bar{g} \tag{1.15}$$

$$\cos\theta_W = g/\bar{g} \tag{1.16}$$

Neutrino interactions are fully described in the Standard Model framework by (Ref. [53]):

$$\mathcal{L}^{CC} = -\frac{g}{\sqrt{2}} j_\alpha^{CC} W^\alpha + h.c. \tag{1.17}$$

$$\mathcal{L}^{NC} = -\frac{g}{2\cos\theta_W} j_\alpha^{NC} Z^\alpha \tag{1.18}$$

where

$$j_\alpha^{CC} = 2\sum_{l=e,\mu,\tau} \bar{\nu}_{lL}\gamma_\alpha l_L \tag{1.19}$$

$$j_\alpha^{NC} = \sum_{l=e,\mu,\tau} \bar{\nu}_{lL}\gamma_\alpha \nu_{lL} \tag{1.20}$$

Since the charge of neutrino is zero there are three possibilities for neutrino mass term, depending on the presence of right-handed fields ν_R and conservation of the total lepton number: Dirac, Majorana and general term incorporating both types.

If Lagrangian density contains both left-handed and right-handed fields and total lepton number is conserved, mass could be introduced with the following term:

$$\mathcal{L}^D(x) = -\sum_{l\,l'} \bar{\nu}_{l'L}(x) M^D_{ll'} \nu_{lR}(x) + h.c. \tag{1.21}$$

where M^D is 3×3 *non-diagonal* matrix.

Diagonalization of the matrix leads to the Lagrangian density:

$$\mathcal{L}^D(x) = -\sum_{i=1}^{3} m_i \bar{\nu}_i(x) \nu_i(x) \tag{1.22}$$

where $\nu_i(x)$ is a field of neutrino with mass m_i.

Thus, flavor fields $\nu_{lL}(x)$ are expressed though the massive fields $\nu_{iL}(x)$ by relation:

$$\nu_{lL}(x) = \sum_{i=1}^{3} U_{li} \nu_{iL}(x) \tag{1.23}$$

U is the unitary Pontecorvo–Maki–Nakagawa–Sakata (PMNS) mixing matrix, which is characterized by three mixing angles and one CP-phase:

$$\begin{aligned} U &= \begin{pmatrix} 1 & 0 & 0 \\ 0 & c_{23} & s_{23} \\ 0 & -s_{23} & c_{23} \end{pmatrix} \begin{pmatrix} c_{13} & 0 & s_{13}e^{-i\delta} \\ 0 & 1 & 0 \\ -s_{13}e^{i\delta} & 0 & c_{13} \end{pmatrix} \begin{pmatrix} c_{12} & s_{12} & 0 \\ -s_{12} & c_{12} & 0 \\ 0 & 1 & 0 \end{pmatrix} \\ &= \begin{pmatrix} c_{12}c_{13} & s_{12}s_{13} & s_{13}e^{-i\delta} \\ -s_{12}c_{13} - c_{12}s_{13}s_{23}e^{i\delta} & c_{12}c_{23} - s_{12}s_{13}s_{23}e^{i\delta} & s_{23}c_{13} \\ s_{12}s_{13} - c_{12}s_{13}c_{23}e^{i\delta} & -s_{23}c_{12} - s_{12}s_{13}c_{23}e^{i\delta} & c_{23}c_{13} \end{pmatrix} \end{aligned} \tag{1.24}$$

where $s_{ij} = \sin\theta_{ij}$ and $c_{ij} = \cos\theta_{ij}$.

For the Majorana case we have:

$$\mathcal{L}^M(x) = -\frac{1}{2} \sum_{l',l} \bar{\nu}_{l'L}(x) M^L_{l'l} (\nu_{lL})^c(x) + h.c. \tag{1.25}$$

where M^L is a complex symmetrical 3×3 matrix. By diagonalization one get:

$$\mathcal{L}^M(x) = -\frac{1}{2} \sum_{i=1}^{3} m_i \bar{\nu}_i(x) \nu_i(x) \tag{1.26}$$

where massive fields $\nu_i(x)$ with mass m_i satisfy the conditions:

$$\nu_i(x) = \nu_i^c(x) = C\bar{\nu}_i^T(x) \tag{1.27}$$

that is truly natural ($\nu_i \equiv \bar{\nu}_i$).

Flavor fields $\nu_{lL}(x)$ are expressed though the massive fields $\nu_{iL}(x)$ in the same way:

$$\nu_{lL}(x) = \sum_{i=1}^{3} U_{li} \nu_{iL}(x) \tag{1.28}$$

PMNS matrix U is parameterized by three mixing angles and three CP phases.

It is important to note that if neutrinos are Dirac particles, their mass can be generated by the standard Higgs mechanism. However, if the Lagrangian density contains Majorana mass term, it could be generated only by a mechanism *beyond Standard Model*.

The presence of the mass of neutrino leads to a beautiful effect of neutrino oscillations which will be discussed further in detail.

ν_e-Neutrino and electron are forming an isodoublet. Change of the charge by unity is a change of the third projection of isospin T_3 by unity.

$$\frac{gg'}{\bar{g}} = e \equiv \sqrt{4\pi\alpha}, Q = T_3 + \frac{Y}{2} \tag{1.29}$$

Numerical values of three parameters g, g' and η of electroweak theory could be found from the most accurate measured parameters:

$$\alpha^{-1} = 137,035985(61) \tag{1.30}$$

$$G_\mu = 1,16639\,10^{-5}\,\text{GeV}^{-2} \tag{1.31}$$

$$M_Z = 91,188(2)\,\text{GeV} \tag{1.32}$$

Higgs sector contains 15 additional arbitrary parameters: masses of charged leptons (3) and quarks (6), parameters of CKM matrix (4), the mass of Higgs boson and λ.

Using these values and expressions (1.15) and (1.16) we can derive the value of $\sin^2\theta_W$:

$$\sin\theta_W\cos\theta_W = \frac{gg'}{\bar{g}^2} = \frac{\sqrt{4\pi\alpha}}{\bar{g}} \tag{1.33}$$

where we need the expression for $\bar{g}$.

From the equations (1.11) and (1.12) it is easy to get:

$$\frac{M_W}{M_Z} = \frac{g}{\bar{g}} \tag{1.34}$$

If we put this relation in (1.4) we get the relation for $\bar{g}$:

$$\frac{G_\mu}{\sqrt{2}} = \frac{\bar{g}^2}{8M_Z^2} \tag{1.35}$$

If one put (1.35) into (1.33) one can obtain:

$$\sin^2\theta_W\cos^2\theta_W = \frac{\pi\alpha}{\sqrt{2}G_\mu M_Z^2} \tag{1.36}$$

and

$$\sin^2\theta_W = 0.212. \tag{1.37}$$

In the context of NSI interaction studies, Z-boson neutral current interaction has particular importance.

The amplitude of the decay on the pair of two fermions could be written as:

$$A_{Z\to f\bar{f}} = \frac{\bar{g}}{2}\bar{f}(g_V^f\gamma_\alpha + g_A^f\gamma_\alpha\gamma_5)fZ_\alpha \tag{1.38}$$

where $g_V^f = T_3^f - 2Q^f\sin^2\theta_W$ and $g_A^f = T_3^f$ are determined by third projection of the spin and electric charge. Calculated width is [51]:

$$\Gamma_{Z\to ff} = \frac{G_F M_Z^3}{6\sqrt{2}\pi}[(g_V^f)^2 + (g_A^f)^2] = 332[(g_V^f)^2 + (g_A^f)^2]MeV \tag{1.39}$$

Let us look at measured for $Z \to ll$ decay axial and vector constants:

$$g_{Al}^{exp} = -0.5012 \pm 0.0003 \tag{1.40}$$

$$g_{Vl}^{exp} = -0.0378 \pm 0.0004 \tag{1.41}$$

and compare them with the theoretical value obtained with $\sin^2\theta_W$ (expression (1.37)):

$$g_{Al}^{theo} = -0.5 \tag{1.42}$$

$$g_{Vl}^{theo} = -1/2 + 2\sin^2\theta_W = -0.076 \tag{1.43}$$

The reason why the theoretical and experimental values of the vector constant are in disagreement is the use of $\sin^2\theta_W$ calculated with α at low energy region. The difference in electromagnetic and weak scales leads to the logarithmic corrections $ln(M_Z/m_e)$. It is convenient to split these corrections from electroweak corrections at the very beginning and use $\alpha(M_Z) = [128.95 \pm 0.05]^{-1}$. In this case, we will get g_{Vl} fully consistent with the experimental value. The review of on electroweak model and current status of the parameter determination could be found in (Ref. [1]).

For the present work the most relevant question is a determination of $\sin^2\theta_W$ from neutrino-electron scattering experiments. The most precise measurement of $\sin^2\theta_W$ as well as g_A and g_V was provided by CHARM II collaboration with a $\nu_\mu e$ scattering experiment (Fig. 1.1). Much weaker results for LSND and TEXONO for $\nu_e e$ and $\bar{\nu_e} e$ channels are also presented on the plot. The best SM fit $\sin^2\theta_W = 0.23129$ is also provided. Note that the solution for the point $g_A = 0$ $g_V = -0.5$ is eliminated by $e^+ + e^- \to l^+ + l^-$ data under the weak assumption that the neutral current is *dominated by exchange of a single Z-boson*. These results will be discussed in a context of neutrino non-standard interactions as well (Sec. 1.2).

Neutrino oscillations

As we saw in the previous subsection neutrinos are introduced in the Standard Model with mass and flavor eigenstates were represented as a superposition of mass eigenstates via a unitary matrix:

$$|\nu_\alpha\rangle = \sum_{k=1}^{3} U_{\alpha k}^{*} |\nu_k\rangle \qquad (\alpha = e, \mu, \tau). \tag{1.44}$$

The main reason to treat neutrino as a massive particle is the discovery of neutrino oscillations. This phenomenon leads to the transition of one flavor type α of neutrino into another type β during propagation. Its observation was confirmed by a variety of experiments (Table 1.1).

Let us find an expression for the transition probability $P_{\nu_\alpha \to \nu_\beta}$. The massive neutrinos are eigenstates of the Hamiltonian

$$H|\nu_k\rangle = E_k |\nu_k\rangle \tag{1.45}$$

with energies $E_k = \sqrt{\vec{p}^2 + m_k^2}$ therefore evolving as plane waves

$$|\nu_k(t)\rangle = e^{-iE_k t} |\nu_k\rangle . \tag{1.46}$$

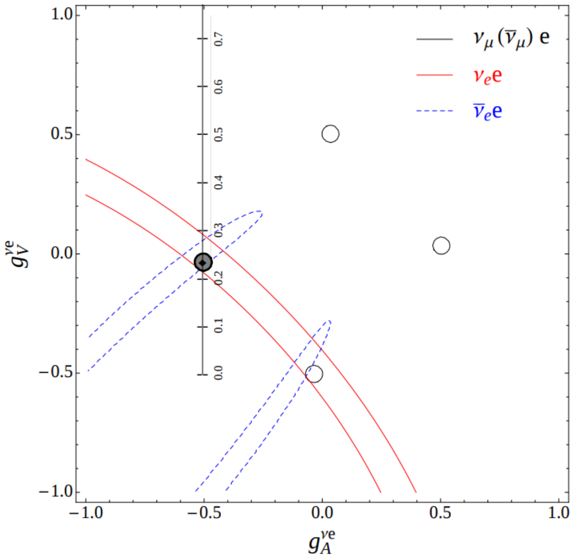

Figure 1.1: Allowed contours for g_V and g_A that were found in neutrino scattering experiments. Results for $\nu_e e$ and $\bar{\nu}_e$ are provided at 1σ. The contour for $\nu_\mu(\bar{\nu}_\mu)e$ are at 90 % C.L. SM best fit value $\sin^2\theta_W = 0.23129$ is indicated by the black dot. The global best fit region (shaded) almost exactly coincides with the result for ν_μ scattering (from Ref. [1])

A flavor state $|\nu_\alpha(t)\rangle$ produced in a flavor eigenstate α at time $t = 0$, $|\nu_\alpha(t=0)\rangle = |\nu_\alpha\rangle$ evolves in time as

$$|\nu_\alpha\rangle = \sum_k U^*_{\alpha k}\, e^{-iE_k t}\,|\nu_k\rangle \tag{1.47}$$

using the unitarity relation, the massive states can be expressed in the basis of flavor states as

$$|\nu_k\rangle = \sum_\beta U_{\beta k}\,|\nu_\beta\rangle \tag{1.48}$$

which allows us to write

$$|\nu_\alpha\rangle = \sum_{\beta=e,\mu,\tau}\left(\sum_k U^*_{\alpha k}\, e^{-iE_k t} U_{\beta k}\,|\nu_\beta\rangle\right) \tag{1.49}$$

one can see that neutrino produced in a flavor eigenstate at $t = 0$ evolves in time as a superposition of different flavor states at $t > 0$.

Expressions for the amplitude and probability:

$$A_{\nu_\alpha\to\nu_\beta}(t) \equiv \langle\nu_\beta|\nu_\alpha\rangle = \sum_k U^*_{\alpha k} U_{\beta k}\, e^{-iE_k t} \tag{1.50}$$

$$P_{\nu_\alpha\to\nu_\beta}(t) \equiv \|A_{\nu_\alpha\to\nu_\beta}(t)\|^2 = \sum_{k,j} U^*_{\alpha k} U_{\beta k} U_{\alpha j} U^*_{\beta j}\, e^{-i(E_k-E_j)t} \tag{1.51}$$

Since in ultrarelativistic case neutrinos propagates with a speed of light $L = t$ $(c = 1)$ and we can approximate the relation $E_k^2 = p^2 + m_k^2$ as

	Experiment	Mode	$\Delta m^2[eV^2]$	Neutrino source
(1)	IMB, Kamiokande, SK, K2K, MINOS, T2K	$\nu_\mu \to \nu_\mu$ $\bar{\nu_\mu} \to \bar{\nu_\mu}$	$\sim \pm 2.5 \times 10^{-3}$	Atmospheric/ Accelerator
(2)	T2K, MINOS	$\nu_\mu \to \nu_e$	$\sim \pm 2.5 \times 10^{-3}$	Accelerator
(3)	Double Chooz, Daya Bay, RENO	$\bar{\nu_e} \to \bar{\nu_e}$	$\sim \pm 2.5 \times 10^{-3}$	Reactor
(4)	Homestake, GNO, GALLEX SAGE, SK, SNO, Borexino	$\nu_e \to \nu_e$	$\sim +8 \times 10^{-5}$	Solar
(5)	KamLAND	$\bar{\nu_e} \to \bar{\nu_e}$	$\sim \pm 8 \times 10^{-5}$	Reactor
(6)	OPERA	$\bar{\nu_\mu} \to \bar{\nu_\tau}$	$\sim \pm 10^{-3}$	Accelerator

Table 1.1: Summary of the $|\Delta m^2|$'s measurements for atmospheric, accelerator and solar neutrino sources (taken from Ref. [23])

$$E_k \simeq p + \frac{m_k^2}{2p} \tag{1.52}$$

$$\tag{1.53}$$

We finally get:

$$P_{\nu_\alpha \to \nu_\beta} = \sum_{k,j} U^*_{\alpha k} U_{\beta k} U_{\alpha j} U^*_{\beta j} \ e^{-i\frac{\Delta m^2_{kj} L}{2E}} \tag{1.54}$$

One can notice that the mass of neutrino is included in expression as Δm^2_{kj}, that is neutrino oscillation experiments are sensitive to the squared mass difference and are not sensitive to absolute masses.

This expression describes well all neutrino oscillation phenomena observed so far[2]. Moreover, a bunch of experiments could use two-flavor approximation to fit their data with one mixing angle θ and one Δm^2. It is easy to calculate probabilities:

$$P_{\nu_\alpha \to \nu_\beta} = \sin 2\theta^2 \sin^2 \frac{\Delta m^2}{4E} L \qquad P_{\nu_\alpha \to \nu_\alpha} = 1 - \sin 2\theta^2 \sin^2 \frac{\Delta m^2}{4E} L \tag{1.55}$$

Looking at expressions (1.55), one may note that the probabilities do not depend on the sign of Δm^2. Therefore, these experiments are not sensitive to relative ordering of the masses.

Mass hierarchy problem

The values Δm^2 for different modes are summarized in Table 1.1. As one may see all that values of Δm^2 have ± sign that indicates unknown ordering with the only exception for solar neutrino experiments (4) that will be discussed later.

All $|\Delta m^2|$ values could be categorized into two distinct ones: $(\Delta m^2)_{sol} \sim 8 \times 10^{-5} eV^2$ (solar) and $(\Delta m^2)_{atm} \sim 2.5 \times 10^{-3} eV^2$ (atmospheric).

In three flavor framework there are three combinations of squared mass differences:

---

[2] Here, we supposed three flavors of the neutrino. However, some experiments indicates the existence of the physics beyond three-flavor oscillation description (see LSND, MiniBooNE and reactor neutrino anomalies)

$$\Delta m_{21}^2 \equiv m_2^2 - m_1^2, \qquad \Delta m_{32}^2 \equiv m_3^2 - m_2^2, \qquad \Delta m_{31}^2 \equiv m_3^2 - m_1^2 \tag{1.56}$$

which are not independent and connected by relation

$$\Delta m_{21}^2 + \Delta m_{32}^2 + \Delta m_{13}^2 = 0. \tag{1.57}$$

The neutrino mass hierarchy is schematically represented in Fig. 1.2 from Ref. [2]. The mass ordering of the states m_1 and m_2 was fixed with MSW effect (see the formula (1.59)). The remaining question is the sign of Δm_{32}^2 (Δm_{31}^2).

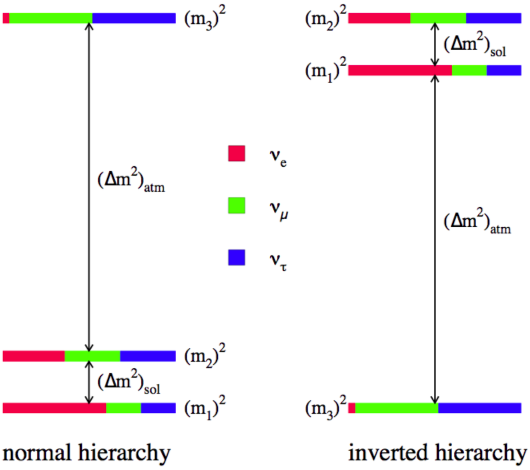

Figure 1.2: Mass scheme for normal and inverted mass hierarchies (from Ref. [2]).

The color scheme in Figure 1.2 represents the relative contribution of mass states m_1, m_2, m_3 in flavor states m_e, m_μ, m_τ. As one may see, the normal hierarchy preserve the mass ordering of charged leptons for neutrino, while for inverted it is not the case. There is no particular reason, why the mass hierarchy of neutrino should be the same as for leptons, so both variants of hierarchies are acceptable in neutrino analysis.

The determination of the MH has profound impacts on the understanding of the neutrino physics, astronomy and cosmology. First of all, it helps to define the goal of neutrinoless double beta decay ($0\nu\beta\beta$), since the chance to observe $0\nu\beta\beta$ is greatly enhanced for an inverted mass hierarchy and the Majorana nature of neutrinos. Second, it is a crucial factor for measuring the lepton CP-violating phase δ, increasing the significance of its measurement by other experiments. Moreover, the mass hierarchy is a crucial parameter of the neutrino astronomy and neutrino cosmology to explain spectral splits in supernova neutrino fluxes (Ref. [54]). Finally, it is essential discriminators for model building of the neutrino masses and flavor mixing. The problem of the mass hierarchy can be resolved with different experimental configurations, involving MSW effect such as solar neutrino experiments, long-baseline accelerator and atmospheric antineutrino $\nu_e \to \nu_e$ experiments or medium-baseline reactor which exploit oscillation interference between $\Delta m_{31}^2$and Δm_{32}^2.

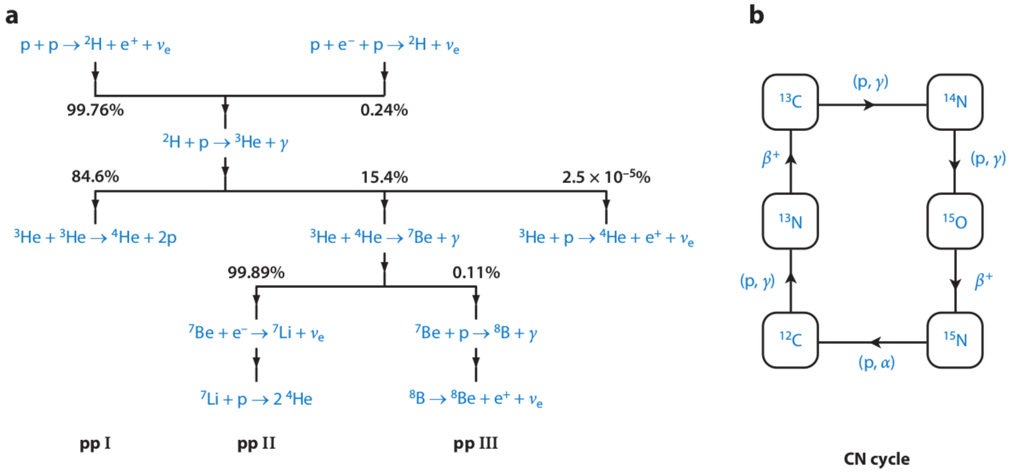

Figure 1.3: *pp* and CNO I cycles. From Ref. [3].

Solar neutrino physics

The Sun produces energy by thermonuclear reactions in which four atoms of hydrogen are forming one atom of helium-4 through the chain of intermediate reactions. Nature gave us many possibilities to perform such transition, which is a quite remarkable fact. The majority of the energy of the Sun is produced in the *pp*-chain (Fig. 1.3 a.). This chain starts from the collision of two protons (so-called *pp*-reaction). This reaction has the smallest rate among others in the chain at solar conditions. It determines the speed of the whole chain and therefore the thermal power of the Sun.

There are four branches of the chain: pp I, pp II, pp III and hep. Moreover, with a probability 0.24%, the chain could start with a three-body reaction of two protons and electron (so-called *pep*).

Apart from the pp I, all other branches produce neutrino with different energies making the spectrum of the solar neutrino very rich. Fig. 1.4 is a classic representation of the solar neutrino spectra.

The spectrum of *pp*-reaction has an end-point at 0.42 MeV and requires the lowest energy threshold for observation. ^{7}Be and *pep* reactions have only two products in the final state, so the neutrino is *monoenergetic*. The ^{8}B spectrum achieves energies up to ~ 16 MeV. The neutrino from these reactions was directly observed by several solar neutrino experiments. The resent results of BOREXINO collaboration includes simultaneous precision spectroscopy of *pp*, ^{7}Be, *pep* and ^{8}B (Ref. [55]). The *hep* reaction is rare and so far directly non-observable, but it produces the most energetic neutrino.

There is an alternative way for generating energy - CNO cycle. It gives about 1% to the total energy production (Ref.[56]). The relative importance of this cycle increases with the mass and temperature of a star. There are several variants of this cycle. The biggest contribution gives CNO I, represented in Fig. 1.3) generating ^{13}N and ^{15}O spectra 1.4. CNO II, being two orders of magnitude less, gives ^{17}F (not shown). Neutrino from CNO-cycle were not yet observed directly (Ref. [55], [57]).

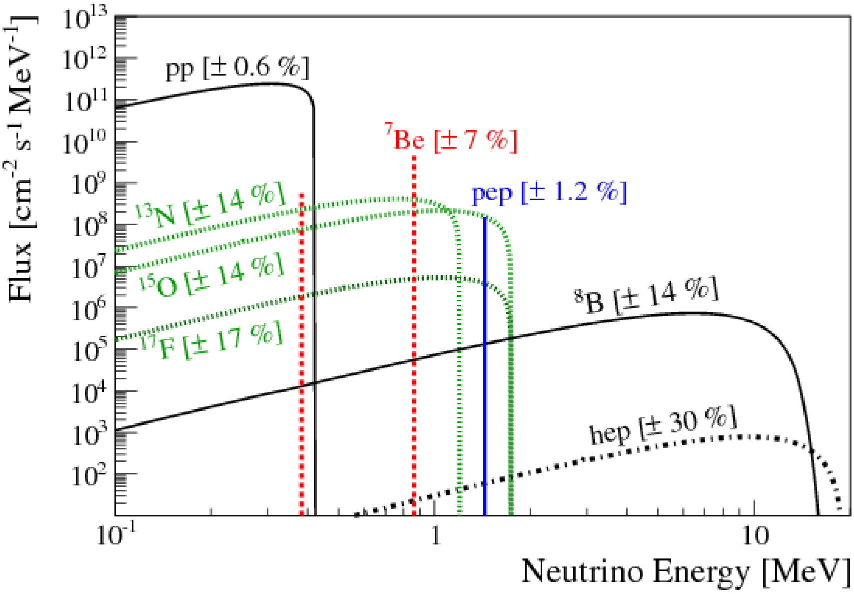

Figure 1.4: Solar neutrino energy spectra (from Ref. [4])

SSM and metallicity problem

Standard Solar Model (SSM) model gives predictions for the neutrino fluxes. At the very first measurements of solar neutrino, the problem of the deficit of the detected neutrino appeared. It forced further intensive verification of the SSM. However, the problem was finally resolved by introducing the neutrino mixing and MSW effect: the measured fluxes became consistent with SSM predictions. The problem of the deficit was closed, but a new problem related to the Sun's chemical composition appeared, the problem of *metallicity*. There are two main complementary sources of information about the chemical composition of the Sun: the solar photospheric spectrum and primordial meteorites. The first gives information about a variety of elements using absorption lines into the solar spectrum. However, the dependence on the solar atmosphere and line formation model restrict the accuracy of the method. The second, model-independent, method permits accurate laboratory measurements, but only with a small sub-sample of meteorites which was not affected by fractionation. Moreover, elements like H, He, C, N, O and Ne are volatile and could not be accumulated in the meteorites (Ref. [58]).

The resent measurements of the heavy elements abundance showed that it was previously overestimated (Ref. [59]). However, models that incorporate this results disagree with helioseismological data. This new class of models was named as low metallicity (LZ). On the contrary, the class of old models became high metallicity (HZ). This problem is relevant to our study since solar models with high and low metallicity predict different neutrino fluxes. Here we will consider both classes of the models (HZ and LZ).

Despite this, the uncertainty in the SSM parameters leads to the uncertainty of neutrino fluxes that are comparable with the difference between high and low metallicity models (so far it is about half of the difference for CNO, ^{8}B and ^{7}Be fluxes). Hence, even in case of a precise neutrino flux measurements the possibility to discriminate between

Table 1.2: Predictions of some solar neutrino fluxes for high (HZ) and low (LZ) metallicity models (from Ref. [5]). Units: 10^{10} (pp), 10^{9} (^{7}Be), 10^{8} (pep, CNO), 10^{6} (^{8}B) cm^{-2}s^{-1}

Flux	B16(GS98)-HZ	B16(AGSS09)-LZ
pp	$5.98(1 \pm 0.006)$	$6.03(1 \pm 0.005)$
pep	$1.44(1 \pm 0.009)$	$1.46(1 \pm 0.009)$
^{7}Be	$4.93(1 \pm 0.06)$	$4.50(1 \pm 0.06)$
CNO	$4.88(1 \pm 0.11)$	$3.51(1 \pm 0.10)$
^{8}B	$5.29(1 \pm 0.20)$	$3.26(1 \pm 0.11)$

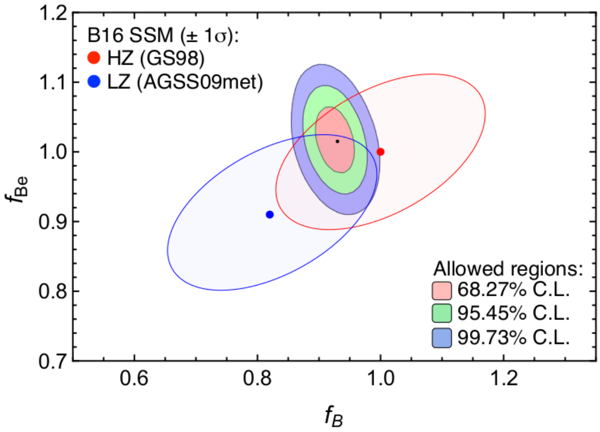

Figure 1.5: Allowed contours obtained with Borexino + KamLAND data for the normalization of the ^{7}Be and ^{8}B fluxes. The experimental uncertainties are less than theoretical one for SSM predictions (from Ref. [5]).

the two models is limited. In fact, the recent Borexino measurement of ^{7}Be flux with precision 2.7 % Ref. [55] clearly demonstrates this (Fig. 1.5).

Further improvements for the precision of neutrino fluxes could be achieved by increasing the accuracy of the ^{3}He + ^{4}He cross section and reducing the systematic uncertainties for the measurements of the surface composition of the Sun (Ref. [59]).

The main error for the ^{7}Be-flux originates from the solar radiative opacity. ^{8}B and ^{7}Be fluxes are both sensitive to the iron abundance. The reduction of its uncertainty may significantly improve the predictions Ref. [59].

Survival probability and MSW effect

The theory of matter effects and resonance enhancement of oscillations developed by L.Wolfenstein (Ref. [46]), S.Mikheyev and A. Smirnov (Ref. [47]) provided an elegant solution of the solar neutrino problem. Incorporating matter effects in the Sun, the survival probability could be written as:

$$P_{ee}^{2\nu} = \frac{1}{2}(1 + \cos 2\theta_m^0 \cos 2\theta), \tag{1.58}$$

where

Table 1.3: Average value of the potential $\bar{V}_K$ for different solar components

K	pp	^{8}B	^{13}N	^{15}O	^{17}F	^{7}Be	pep	hep
V_K, 10^{-12} eV	4.68	6.81	6.22	6.69	6.74	6.16	5.13	3.96
$\Delta V_K^2/\bar{V}_K^2$	0.109	0.010	0.054	0.013	0.012	0.029	0.076	0.165

$$\cos 2\theta_m(V) = \frac{\cos 2\theta - \frac{2EV}{\Delta m^2}}{\sqrt{(\cos 2\theta - \frac{2EV}{\Delta m^2})^2 + \sin^2 2\theta}} \tag{1.59}$$

This formula can describe all current observed data (Ref. [60]). Non-adiabatic corrections could be also considered though they are quite small (and probably below experimental sensitivity). In a presence of the corrections the formula modifies as:

$$P_{ee}^{2\nu} = \frac{1}{2}(1 + (1 - \delta)\cos 2\theta_m^0 \cos 2\theta) \tag{1.60}$$

In three flavor neutrino case the formula is

$$P_{ee}^{3\nu} = c_{13}^4 P_{ee}^{2\nu} + s_{13}^4 \tag{1.61}$$

where $c_{13} = \cos\theta_{13}$ and $s_{13} = \sin\theta_{13}$. In Fig. 1.6 it is represented as MSW-LMA solution. The potential should be modified in this case as well:

$$V \to c_{13}^2 V \tag{1.62}$$

We will use the formula (1.61) in the analysis to obtain expected solar neutrino interaction rates in a detector.

Non-Standard Interactions

Theoretical overview

This study is dedicated to new interactions of neutrino and electron. The Standard Model cross section of this interaction is precisely calculated. In principle, some subclass of the new interactions may modify total and differential cross sections revealing themselves. We denote such subclass of the new interactions as *non-standard* interactions or shortly NSI.

Neutrino sector in the last years has been reaching the level of precision measurements of oscillation parameters. Regardless this fact, the current experiments are not able to exclude many possible scenarios, even for some particular cases (e.g., $\nu_\tau + e$) leaving the possibility of the presence of interactions that are comparable with the standard ones as we see further. Analogously to standard electroweak interactions NSI could be charged current (CC) and neutral current (NC).

The current status of theoretical description of NSI as well as the review on the current limits could be found in Ref. [61], [62], [19] and [63]. Here I illustratively provide several scenarios:

- Gauge symmetries

  Any extension of the symmetry $SU(2)_L \times U(1)_Y$ leads to the appearance of the additional bosons and the modification of the constants of interaction. For example, the theory with E_6-symmetry includes $U(1)_\chi \times U(1)_\psi$ and correspondingly extra additional boson Z'.

- Additional neutral leptons

  Starting with standard gauge group $SU(2)_L \times U(1)_Y$, introducing an additional *neutral* leptons could lead to the modification of $V - A$ interaction.

- Additional scalar particles

  Although NSI interactions save the $V - A$ structure of the theory, it is also possible to include additional scalar interaction.

NC NSI could be probed with a variety of experiments. One of the most particular, strong and natural sources of neutrino that could be used for NSI studies is the Sun. The main advantage it has - neutrinos for ^{7}Be and *pep*-reactions are *monochromatic*. An observed electron recoil spectrum from monochromatic neutrinos is an exact representation of a differential $\nu - e$ cross section convoluted with a detector response function. All experiments that can observe electron recoil spectrum from ^{7}Be reaction become sensitive to NSI, since strong dependence of the differential cross section normalization and shape from the NSI parameters. On the contrary, as we will see for the case of the *pp* electron recoil spectrum the convolution with a continues neutrino spectrum significantly reduces the sensitivity.

The study of non-standard interactions of neutrino and electron in the form which is very close to the one that we are considering appeared in (Ref. [64]). At that time the problem of the deficit of neutrino was not yet resolved. Several scenarios were proposed to resolve the discrepancy between the measured rate of solar neutrinos and Standard Solar Model prediction. One of them included the presence of neutrino oscillations, that could be naturally introduced in the Standard Model, together with the effect of the resonant conversion of neutrinos in matter: Mikheyev -Smirnov-Wolfenstein (MSW) effect.

Another attractive scenario for neutrino oscillations was vacuum oscillations with a baseline comparable with the Sun-Earth distance, so-called *just-so* oscillations (Ref. [64]). This solution required a $\delta m^2 \sim 10^{-10}$ and large mixing angles. The Earth-Sun orbit is elliptical and the distance between Sun and Earth could be described by $L_t = \bar{L}(1-\eta\cos(2\pi t/T))$, where $\bar{L} = 1.5 \times 10^{11}$, $T = 365.2425$ days and $\eta = 0.0167$. Since the distance changes with time, it should imply the time variation of the signal with time or annual time modulation of the survival probability.

It was shown (Ref. [64]) that just-so scenario describes much better the experimental data if we suppose the conversion of solar electron neutrino only in τ-neutrino and the presence of additional interactions of ν_τ with electron described by Lagrangian:

$$\mathcal{L}_{eff} = -\frac{G_F}{\sqrt{2}}\bar{\nu_\tau}\gamma^\mu(1-\gamma_5)\nu_\tau[\varepsilon\bar{e}\gamma_\mu(1+\gamma_5)e + \varepsilon'\bar{e}\gamma_\mu(1-\gamma_5)e] \tag{1.63}$$

The first term ε could be obtained from an exchange of some additional electroweak scalar ϕ. The second term could be an exchange of charged Higgs singlet. However, it should contribute into τ decay, and from this, the limit was obtained $\varepsilon' < 0.05$ The prediction for future neutrino experiments such as SNO, Super-Kamiokande, and Borexino was also provided.

Let us generalize this case. From the phenomenological point of view NSI could be described by four-fermion operator (Ref. [62], [24]):

$$\mathcal{L}_{NSI} = -2\sqrt{2}G_F\varepsilon_{\alpha\beta}^{ff'C}(\bar{\nu}_\alpha\gamma^\mu P_L\nu_\beta)(\bar{f}\gamma_\mu P_C f'), \tag{1.64}$$

where $\varepsilon_{\alpha\beta}^{ff'C}$ are parameters that describe the non-standard interaction of neutrino with flavor $\alpha = e, \mu, \tau$ and lepton f. Note that the index β is indicating the flavor of neutrino in the final state and could be not equal to the initial state. In this case an interaction is classified as flavor-changing. $P_L = (1-\gamma_5)/2$ and $P_R = (1+\gamma_5)/2$ are left and right projection operators and $C = L, R$ is an index of summing.

The structure of the operator was chosen as (V - A)(V - A). Though other (V + A)(V + A), (S ± P)(S ± P) and TT Lorentz-invariant structures are also possible, they are expected to be helicity-suppressed or to be very small due to their contributions by higher order corrections (Ref [65], [66], [67], [68]). NSI with right-handed neutrinos where also neglected due to their suppression by helicity.

Some theories may give the order of magnitude for the parameters:

$$\varepsilon_{\alpha\beta}^{ff'} \sim \frac{m_W^2}{m_X^2}, \tag{1.65}$$

where m_X is the mass of the scalar field. For $m_X \sim 1\,TeV$: $\varepsilon_{\alpha\beta}^{ff'} \sim 10^{-2}$.

In the present work we are discussing the flavor-conserving interactions of neutrino and electron ($f = f' = e$, $\alpha = \beta$), so the following nomenclature will be used:

$$\varepsilon_{\alpha\alpha}^{ffC} = \varepsilon_\alpha^C, \tag{1.66}$$

giving six possible parameters ($C = L/R$, $\alpha = e$,μ,τ).

Although the expression (1.64) gives a general description of NSI's it is possible also to use other approaches (Ref. [63]), depends on if we consider neutrino in the point of production ε_S, propagation ε_m or detection ε_D. In this study, we are concentrating on the detection case, but quite relevant propagation case will also be discussed later. Inside the Sun, the flavor diagonal NSI's under consideration contribute to the production of same-flavor $\nu\overline{\nu}$ pairs via photo-production ($\gamma e \to e\nu\overline{\nu}$), $\nu\overline{\nu}$-Bremsstrahlung (the photon leg in $\gamma e \to e\nu\overline{\nu}$ is anchored on an ion or another electron), etc. [69]. However, the energies of the neutrinos and anti-neutrinos produced by these processes are expected to be in the few keV range, well below the ~50 keV detection threshold of liquid scintillator detectors like Borexino.

It was pointed out that Borexino has a potential for ^{7}Be and *pep* neutrino measurements (a possibility to measure *pp* neutrinos was not yet supposed) (Ref. [64]). The experiment has a unique possibility to see the electron recoil spectrum which in case of ^{7}Be and *pep* neutrinos is step-like, thanks to the mono-energetic spectra of neutrino and energy resolution. It was shown that in the presence of non-standard interactions of τ-neutrino with electron the electron recoil spectrum became much steeper (see Fig.8 in Ref. [64]).

This feature of the spectrum then was exploited in (Ref. [24]) to predict a limit on the parameters of non-standard interactions ε_e and ε_τ (the limit on ε_μ was already set in $\nu_\mu e$ scattering by CHARM II collaboration (Ref. [70]). Later when Borexino Phase-I data was released, based on the values of the signal and background rates from the experimental spectrum the limits on the ε_e and ε_τ were set (Ref. [25]).

$$-0.046 < \varepsilon_L^e < 0.053 \quad -0.206 < \varepsilon_R^e < 0.157 \tag{1.67}$$

$$-0.23 < \varepsilon_L^\tau < 0.86 \quad -0.968 < \varepsilon_L^\tau < 0.716 \tag{1.68}$$

Borexino, with the newly released data set, has the potential to establish the record limit on the parameters of NSI $\varepsilon_e^{L/R}$, $\varepsilon_\tau^{L/R}$. We do not consider here the parameters which come from charged lepton flavor conversion, such as $\mu \to e\gamma$ and $\mu \to e$. They always involve, at some level, a one loop dressing of the neutrino vertex and, therefore, they are always model dependent (Ref. [63]).

Neutrino-electron elastic scattering cross section

The differential cross section of neutrino-electron scattering could be precisely calculated in low energy approximation as (Ref. [71]):

$$\frac{d\sigma_\alpha(E,T)}{dT} = \frac{2}{\pi}G_F^2 m_e\Big[g_{\alpha L}^2 + g_{\alpha R}^2(1-\frac{T}{E})^2 - g_{\alpha L}g_{\alpha R}\frac{m_e T}{E^2}\Big], \tag{1.69}$$

where T - kinetic energy of the electron, E - an incident neutrino energy, $\alpha = e, \mu, \tau$ is a flavor of neutrino.

The maximal energy of electron (Compton-like shoulder of the spectrum) is kinematically determined as:

$$T_{max} = \frac{E}{1+\frac{m_e}{2E}} \tag{1.70}$$

The coupling constants are:

$$g_{\alpha L} = \sin^2\theta_W \pm \frac{1}{2} \tag{1.71}$$

$$g_{\alpha R} = \sin^2\theta_W \tag{1.72}$$

Analyzing expression (4.50) one may see that the first term is a constant and contains only $g_{\alpha L}$. The second one contains $g_{\alpha R}$ only and has an energy dependence, being proportional to $(1-\frac{T}{E})^2$. The last term contains $g_{\alpha L}g_{\alpha R}$ and proportional to $\frac{m_eT}{E^2}$ It does not play such a big role and becoming negligible at $E >> m_e$.

Total cross section could be computed by integration of expression (4.50) over T in a range from 0 to T_{max}:

$$\sigma_\alpha(E) = \frac{2}{\pi}G_F^2 m_e T_{max}\Big[g_{\alpha L}^2 + g_{\alpha R}^2(1-\frac{T_{max}}{E}+\frac{T_{max}^2}{3E^2}) - g_{\alpha L}g_{\alpha R}\frac{m_eT_{max}}{2E^2}\Big] \tag{1.73}$$

For calculations it is quite useful to evaluate:

$$\frac{2}{\pi}G_F^2 m_e = 4.425\,10^{-23}\,\mathrm{MeV}^{-3} = 1.723\,10^{-44}\,\mathrm{cm}^2\,\mathrm{MeV}^{-1}$$

with $G_F = 1.1663787(6)\times10^{-5}\,\mathrm{GeV}^{-2}$, $m_e = 0.5109\,\mathrm{MeV}$ and $\hbar c = 197.327\,\mathrm{MeV\,fm}$.

Since the operator (1.64) has the same structure as the low energy approximation of electroweak operator that describe neutrino-electron elastic scattering, the presence of the non-standard interactions could be introduced as modification of the coupling constants:

$$\tilde{g}_{\alpha R} = g_{\alpha R} + \varepsilon_\alpha^R \tag{1.74}$$

$$\tilde{g}_{\alpha L} = g_{\alpha L} + \varepsilon_\alpha^L \tag{1.75}$$

NSI at propagation

In the Ref. [25], only *pp* and ^{7}Be were only considered. Both of them are in the vacuum-like energy region, and the effects of NSI at propagation are quite small.

In this analysis, CNO and *pep* located in the transition zone (as well as ^{8}B for radiochemical constraint), are also considered. For them the effect of the NSI at propagation is relevant and may affect the analysis. NSI leads to the modification of the survival probability $P_{ee}(E)$ and contributes in the modification of predicated Borexino's rates together with cross section modifications at interaction point. The description of the NSI-at-propagation framework could be found in Ref. [72] and [73]. From the practical point of view the modification into $P_{ee}(E)$ is introduced as a redefinition of the potential $V(x)\rightarrow(1-\varepsilon')V(x)$, where $\varepsilon' = \sin^2\theta_{23}\varepsilon_\tau^V - \varepsilon_e^V$ and $\varepsilon_\alpha^V = \varepsilon_\alpha^L + \varepsilon_\alpha^R$.

In the Fig. 1.6, the modification of the survival probability for three values of ε' is shown. The positive ε'-parameter corresponds to the higher survival probability and negative - to the lower. As it was expected the largest effect is presented in the transition energy zone, while it is $\sim 5\%$ for *pp* and ^{7}Be neutrinos. NSI-at-propagation effect was included in the analysis, but it was found to be negligible.

In principle, this effect should be included in the predicted rates for radiochemical experiments. However, since radiochemical constraint did not demonstrate particular sensitivity, the effect of NSI at propagation was not investigated for this case.

Current limits on non-standard neutrino interactions with electron

Current limits on the constants of interaction with electron are given in the review Ref. [63] Table (1.4). In addition, further limits from Ref. [19] with some comments are provided. Each limit was obtained keeping all other parameters at zero. It is necessary to be

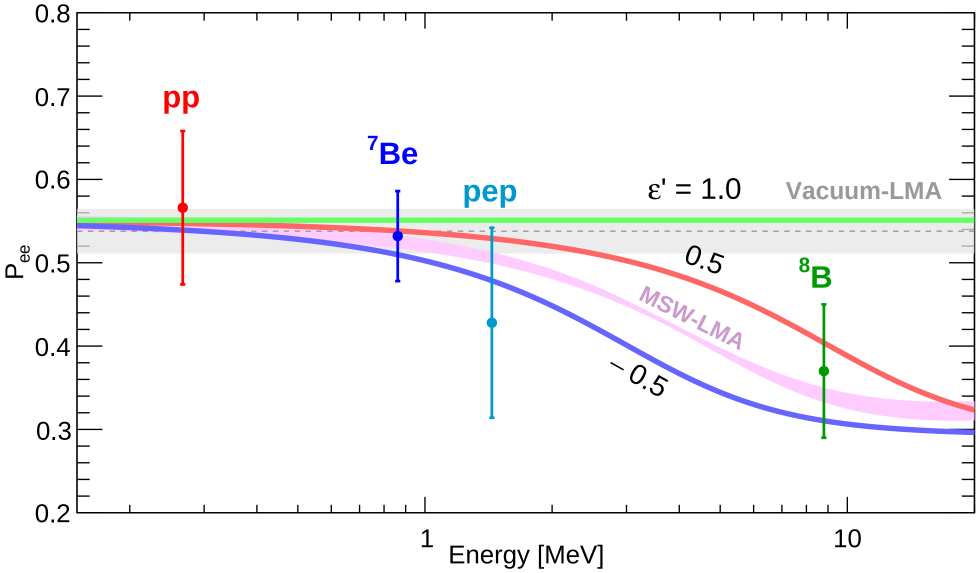

Figure 1.6: Electron neutrino survival probability $P_{ee}(E)$ for LMA-MSW solution with uncertainties of oscillation parameters taken into account (pink band), and LMA-MSW + NSI solutions for $\varepsilon' = -0.5, 0.5, 1.0$ and average values of oscillation parameters. Note that $P_{ee}(E)$ is enhanced for $\varepsilon' > 0$ and reduced for $\varepsilon' < 0$. When $\varepsilon' \to 1$ the $P_{ee}(E)$ tends to Vacuum-LMA solution (grey band). To illustrate the capability of the detector to sense NSI's at propagation, experimental points for $P_{ee}(E)$, obtained by Borexino with HZ-SSM assumption, are also provided (Ref. [6]). ^{8}B and pp data points are set at the mean energy of neutrinos that produce scattered electrons above the detection threshold. The error bars include experimental and theoretical uncertainties. Note that for the range $\varepsilon' = (-0.5, 0.5)$ mostly relevant for the analysis, $P_{ee}(E)$ is within the error bars of the experimental measurements, suggesting that the effects of NSI's at propagation are not particularly strong.

ε_{ee}^{eL}	(-0.021,0.052) (Ref. [72])	
ε_{ee}^{eR}	(-0.07,0.08) (Ref. [74])	(-0.08,0.09) (Ref. [63])
.$\varepsilon_{\mu\mu}^{eL}$	(-0.03,0.03) (Ref. [19] and [22])	
$\varepsilon_{\mu\mu}^{eR}$	(-0.03,0.03) (Ref. [19] and [22])	
$\varepsilon_{\tau\tau}^{eL}$	(-0.16,0.11) (Ref. [72])	(-0.46,0.24) (Ref. [22])
$\varepsilon_{\tau\tau}^{eR}$	(-0.25,0.43) (Ref. [22])	

Table 1.4: Current limits on the parameters $\varepsilon_{e,\mu,\tau}^{L/R}$ (Ref. [24])

aware of the direct comparison of the results since different groups may have different approaches and assumptions.

ε_e^L parameter

The most accurate measurement of $\nu_e e \to \nu_e e$ [3] cross section was provided by LSND (Ref. [19]):

$$\sigma(\nu_e e \to \nu_e e) = (1.17 \pm 0.17)\frac{G_F^2 m_e E_\nu}{\pi} \tag{1.76}$$

SM prediction gives 1.0967 for the coefficient. Based on this measurements, one can easily get constraints:

$$-0.07 < \varepsilon_e^L < 0.052$$

$$-1 < \varepsilon_e^R < 0.5$$

As it was expected the limit on ε_e^L is much stronger since it dramatically changes the total cross section (see more information in Sec. 1.3.1).

ε_e^R parameter

The strongest direct limit was performed by TEXONO collaboration. TEXONO is a reactor neutrino experiment. It consists of three types of the detectors CsI(T) crystals (187 kg, analysis range 3-8 MeV), HPGe detector (1.06 kg, low background $1\ \mathrm{kg}^{-1}$: keV^{-1} day^{-1}), ultra low energy germanium (ULEGe) detector array (total mass 20 g, threshold 220 ± 10 eV).

Since coupling constants of antineutrino are complementary to the couplings of neutrino TEXONO is the most sensitive to ε_e^R (see more information in Sec. 1.3.1):

$$-0.07 < \varepsilon_e^R < 0.08$$

---

[3] In (Ref. [19]) the flavor of outgoing neutrino was not specified since the authors considered flavor-changing interactions as well

$\varepsilon_{\mu}^{R/L}$ parameter

CHARM II collaboration (Ref. [70]) determined the g_V^e and g_A^A (this measurement is quoted in PDG Ref. [1]) and derived (Ref. [70]):

$-0.025 < \varepsilon_L^{\mu} < 0.03$ $-0.027 < \varepsilon_R^{\mu} < 0.03$

This limit is already firm, therefore we do not consider ν_μ-case in further analysis with Borexino.

$\varepsilon_{\tau}^{R/L}$ parameters

To observe NSI related with τ neutrino is quite problematic. In Ref. [24] it was proposed to use LEP data (the reaction e^+e^-). In Ref. [19] the data SNO, KamLAND and Super-Kamiokande was used to put a constraint.

$-0.6 < \varepsilon_L^{\tau} < 0.4$

$-0.4 < \varepsilon_R^{\tau} < 0.6$

Weinberg angle

The problem of the establishing NSI-limits is equivalent to the measurement of $\sin^2\theta_W$ at low energies. The square of the sine of the Weinberg angle is included linearly in (1.71) and (1.72). The variation of $\varepsilon_L = \varepsilon_R$ with fixed $\sin^2\theta_W$ value is the same as variation of $\sin^2\theta_W$ without NSI parameters included.

As we will see further the NSI-exclusion-contour for Borexino is pulled out along the diagonal limiting the overall sensitivity.

For detailed information on $\sin^2\theta_W$ look Ref. [1] and small PDG booklet 2016. p 202-203. (Ref. [20]).

Astrophysics and Cosmology

In Ref. [19] some considerations about impact of NSI interactions in cosmology were also summarized. The presence of NSI of neutrino modifies cosmological scenarios and observations. First, it could keep neutrino in thermal equilibrium with ordinary matter for a longer time of nucleosynthesis.Stronger interactions with matter in the core of supernova keep neutrinos trapped for a longer time disturbing the duration of the neutrino pulse. They could also contribute to the energy losses of the star due to plasmon decay $\gamma \to \nu\bar{\nu}$ that determines the evolution of red giants. To destabilize the SM results one should modify some of these interactions by a factor more than one. Laboratory data already placed better limits.

Coupling with quarks. Coherent $\nu - N$ scattering. Matter effects

An additional possibility for NSI of neutrino could be realized with modifications of coupling constants with quarks. The study of that kind of interactions is outside of the scope of this work, and here we provide only the most relevant theory and examples. Coherent $\nu - N$ scattering experiments firstly proposed in (Ref. [75]) are very promising for the search for NSI. For neutrino energies below a few tens of MeV, coherent scattering occurs when the momentum transfer Q is comparable to the inverse of the nuclear radius R, i.e., $QR << 1$.

Cross section of the coherent scattering is given by an expression:

$$\frac{d\sigma}{dT} = \frac{G_F^2 M}{\pi} F^2(Q)[(g_V + g_A)^2 + (g_V - g_A)^2(1 - \frac{T}{E_\nu})^2 - (g_V^2 - g_A^2)\frac{MT}{E_\nu^2}] \tag{1.77}$$

where E_ν is the neutrino energy, T - nuclear recoil energy, M - nuclear mass, $F^2(Q)$ is a nuclear form factor and $Q = \sqrt(2MT)$ - transfer of the momentum.

$$g_V = g_V^p Z + g_V^n N$$

and

$$g_A = g_A^p(Z_+ - Z_-) + g_A^n(N_+ + N_-)$$

are vector and axial constants with $g_V^p = 0.0298$, $g_V^n = -0.5117$, $g_A^p = 0.4955$ and $g_A^n = -0.5121$.

Vector constant G_V dominates while G_A is small for most of the nuclei and zero for spin-zero.

For $T << E_\nu$ and neglecting axial terms:

$$\frac{d\sigma}{dT} = \frac{G_F^2 M}{2\pi}\frac{Q_W^2}{4}F^2(Q)(2 - \frac{MT}{E_\nu^2}) \tag{1.78}$$

with

$$Q_W = N - (1 - 4\sin^2\theta_W)Z$$

Since since $\sin^2\theta_W = 0.231$, $Q_W \approx N$ and $\frac{d\sigma}{dT} \propto N^2$ that is number of protons is not important.

The cross section for coherent detection is large $10^{-39} - 10^{-37}\text{cm}^2$, but it is quite difficult to detect an interaction due to tiny nuclear recoil energies $T_{recoil}^{max} = \frac{2E_\nu^2}{M}$. For example for 30 MeV neutrino scattering on Ge nuclei $T_{recoil}^{max} = 25$ keV.

Current bounds for $\varepsilon_{ee}^d - \varepsilon_{ee}^u$ and $\varepsilon_{\mu\mu}^d - \varepsilon_{\mu\mu}^u$ are represented in Fig. 1.7 from Ref. [76] and [7].

Search for CC NSI with reactor neutrino

The possibility to study NSI-effects at medium-baseline reactor antineutrino experiments was considered in [8] and [77]. It was shown that NSI effects may lead to the effects large enough to exclude true value of $\sin^2\theta_{12}$ at more than 3σ level with NSI parameters $\varepsilon_{e\mu}$ $\varepsilon_{e\tau}$. However, the discovery reach of NSI effects has been found to be small depending crucially on the CP-violating phase. The discrimination power of the JUNO experiment to Mass Hierarchy may also be enhanced or reduced with NSI.

In this case NSI effects may occur simultaneously in production and detection point and NSI effects could be incorporated as admixture of the another flavor neutrino states represented as [78]:

$$|\bar{\nu}_\alpha^s\rangle = \frac{1}{N_\alpha^s}(|\bar{\nu}_\alpha\rangle + \sum_\beta \varepsilon_{\alpha\beta}^s |\bar{\nu}_\beta\rangle) \tag{1.79}$$

with normalization

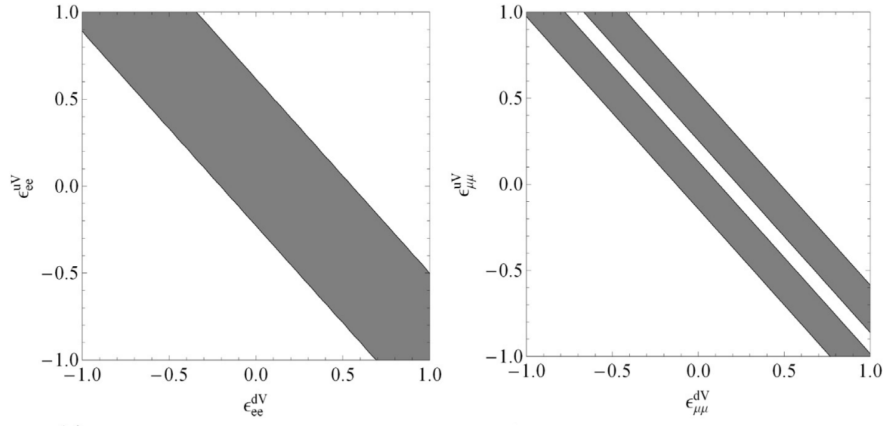

Figure 1.7: Current bounds for $\varepsilon^d_{ee} - \varepsilon^u_{ee}$ and $\varepsilon^d_{\mu\mu} - \varepsilon^u_{\mu\mu}$ based on the result of COHERENT collaboration. (From Ref. [7])

$$N^s_\alpha = \sqrt{\sum_\beta |\delta_{\alpha\beta} + \varepsilon^s_{\alpha\beta}|^2} \tag{1.80}$$

$$N^d_\beta = \sqrt{\sum_\alpha |\delta_{\alpha\beta} + \varepsilon^d_{\alpha\beta}|^2} \tag{1.81}$$

NSI parameters, in general, do not preserve unitary of the mixing matrix. As it was pointed out in Ref. [79], heavy neutrino states responsible for neutrino mass generation may decouple from oscillation process, so the unitarity of the leptonic mixing could be slightly violated.

The effect of non-unitarity could be significant in low-scale seesaw models and could be considered as NSI with $\varepsilon^s = \varepsilon^{d\dagger}$. Additionally, since the leading order NSI's are $V \pm A$ type as long as CPT is conserved we could suppose:

$$\varepsilon^s_{e\alpha} = \varepsilon^{d*}_{\alpha e} = \varepsilon_{e\alpha} e^{i\phi_{e\alpha}}$$

and skip superscripts *s* and *d*.

Straightforward calculations of the amplitude $A_{ee}(L)$ and survival probability give:

$$P(\bar{\nu}_e \to \bar{\nu}_e) = \sum_{i,j} R_i R_j - 4 \sum_{i>j} R_i R_j \sin^2 \frac{\Delta^2_{ij} L}{4E} \tag{1.82}$$

with

$$R_1 = c^2_{12} c^2_{13} - 2 s_{12} c_{12} c_{13} \varepsilon_\phi - 2 c^2_{12} s_{13} c_{13} \varepsilon_\delta + \mathcal{O}(\varepsilon^2)$$

$$R_2 = s^2_{12} c^2_{13} + 2 s_{12} c_{12} c_{13} \varepsilon_\phi - 2 s^2_{12} s_{13} c_{13} \varepsilon_\delta + + \mathcal{O}(\varepsilon^2)$$

$$R_3 = s^2_{13} + 2 s_{13} c_{13} \varepsilon_\delta + \mathcal{O}(\varepsilon^2)$$

and with auxiliary parameters that are defined as:

$$\varepsilon_\phi \equiv c_{23}\varepsilon_{e\mu}\cos\phi_{e\mu} - s_{23}\varepsilon_{e\tau}\cos\phi_{e\tau}$$

$$\varepsilon_\delta \equiv s_{23}\varepsilon_{e\mu}\cos(\phi_{e\mu} - \delta) + c_{23}\varepsilon_{e\tau}\cos(\phi_{e\tau} - \delta)$$

One may notice that the in the limit $\varepsilon \to 0$, we have $R_i \to |U_{ei}|^2$. For medium-baseline neutrino experiments we have

$$P(\bar{\nu}_e \to \bar{\nu}_e) \approx 1 - 4s_{12}c_{12}c_{13}^3\eta_1\sin^2\frac{\Delta m_{12}^2 L}{4E} - 4s_{13}c_{13}\eta_2\sin^2\frac{\Delta m_{31}^2 L}{4E} - 4s_{13}c_{13}\eta_3\sin^2\frac{\Delta m_{32}^2 L}{4E} \tag{1.83}$$

with

$$\eta_1 = s_{12}c_{12}c_{13} + 2(\cos 2\theta_{12}\varepsilon_\phi - \sin 2\theta_{12}s_{13}\varepsilon_\delta)$$

$$\eta_2 = s_{13}c_{13}c_{12}^2 - \sin 2\theta_{12}s + 13\varepsilon_\phi + 2c_{12}^2\cos 2\theta_{13}\varepsilon_\delta$$

$$\eta_3 = s_{13}c_{13}s_{12}^2 + \sin 2\theta_{12}s_{13}\varepsilon_\phi + 2s_{12}^2\cos 2\theta_{13}\varepsilon_\delta$$

Results of simulation of the reactor antineutrino spectrum are presented in Fig. 1.8. One may see a clear difference in the observed amount of events: positive $\varepsilon_{e\mu}$ may reduce, while positive $\varepsilon_{e\tau}$ increase them. Unfortunately, such difference can be fully absorbed by deviation of the $\sin^2\theta_{12}$. The amplitude of high-frequency oscillations increases for both cases that lead to larger values of θ_{13}. The results of the simulations and the fit of the reactor antineutrino spectrum of a medium baseline experiment are presented in Ref. 1.9 and 1.10. They clearly demonstrate above-mentioned deviations of the $\sin^2\theta_{12}$ and $\sin^2\theta_{13}$ from its true values.

Reactor antineutrino spectrum is observed through the energy reconstruction of final state particles in detection point. At practice, one deal with the spectrum of positrons produced in Inverse Beta Decay reaction. More details on how IBD experimental spectrum could be obtained in Appendix.

In principle, the presence of NSI can moderate the experimental power in discriminating neutrino mass hierarchies. However, with the current bounds applied, such effect becomes *insignificant* (Ref. [8]).

As it is easy to see the expression for ε_δ the maximum of this parameter could achieved for $\phi_{e\mu} - \delta = 0$ and $\phi_{e\tau} - \delta = 0$. As a consequence the sensitivity to $\varepsilon_{e\mu}$ and $\varepsilon_{e\tau}$ is maximal. The discovery reach for the $\varepsilon_{e\mu}$ and $\varepsilon_{e\tau}$ is represented in Fig. 1.11, here $\phi_{e\mu}$ and $\phi_{e\tau}$ are supposed to be zero. As one may see for $\varepsilon_{e\mu}$ the limit stronger than experimental sensitivity is set, for $\varepsilon_{e\tau}$ factor two improvement could be achieved.

As one may see the possibility for CC NSI search at large volume liquid scintillator detector at medium baseline strongly depends on resolving power of oscillation patterns with IBD spectrum. The resolving power is determined by the energy resolution and uncertainty of the energy scale as well as the presence of backgrounds which could mimic the coincidence tag of the IBD reaction. Radiopurity of the liquid scintillator is one of the factors that govern background coincidence rate. These questions are elaborated in the following chapters.

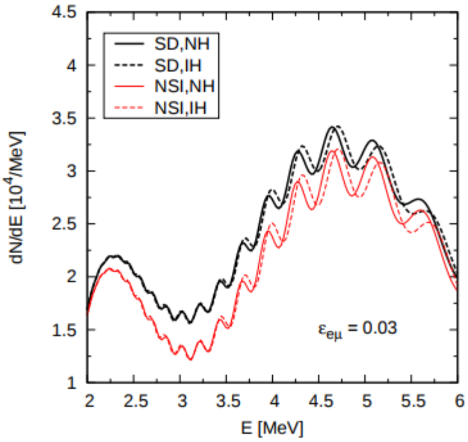

Figure 1.8: Comparison of normal (solid) and inverse (dashed) hierarchy expected antineutrino energy spectrum for the Standard Model (black) and NSI (red) cases (3 % energy resolution applied). From Ref. [8]

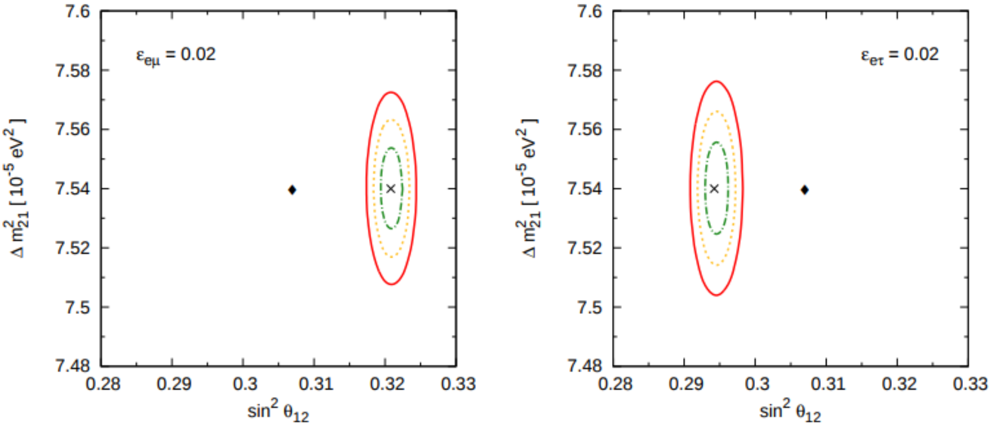

Figure 1.9: Comparison of the $\sin^2\theta_{12}$-Δm^2_{12} result of the fit of the NSI modified spectrum with fitting function w/o NSI. True value of $\sin^2\theta_{12}$ is represented by the black dot. Greed, yellow and red curves stand for the 1σ, 2σ and 3σ C.L. From Ref. [8]

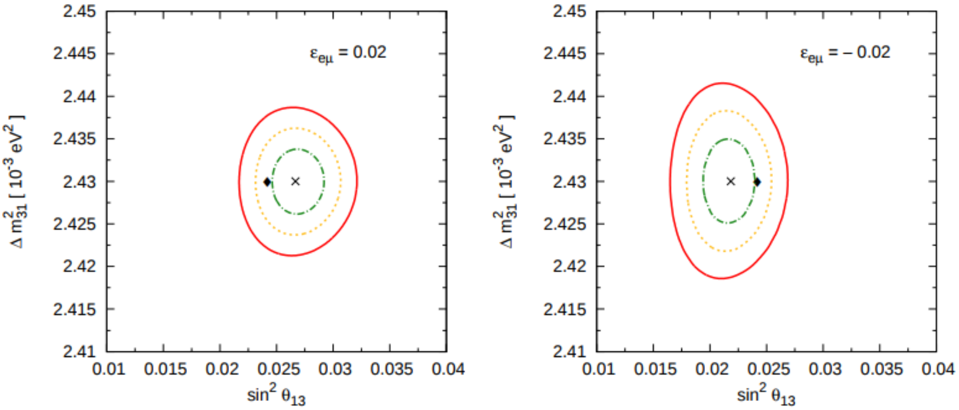

Figure 1.10: Comparison of the $\sin^2\theta_{13}$-Δm^2_{13} result of the fit of the NSI modified spectrum with fitting function w/o NSI. True value of $\sin^2\theta_{13}$ is represented by the black dot. Greed, yellow and red curves stand for the 1σ, 2σ and 3σ C.L. From Ref. [8]

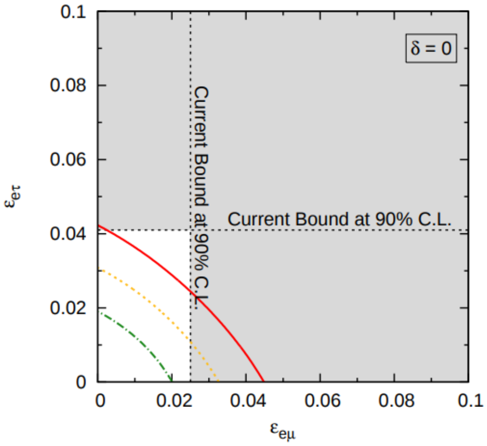

Figure 1.11: The discovery reach for the $\varepsilon_{e\mu}$ and $\varepsilon_{e\tau}$ for the case of maximal sensitivity $\delta = 0$. $\phi_{e\mu} = \phi_{e\tau} = 0$. Excluded 90 % C.L. region is represented by gray. Green, yellow and red curves stand for the 1σ, 2σ and 3σ C.L. From Ref. [8]

Borexino experiment and Solar neutrino physics

The Borexino detector is a unique scientific tool that able to study solar neutrinos with energy as low as 150 keV. Scientific goals of the detector together with the problem of solar neutrinos are, in fact, on the intersection of particle physics and astrophysics, since the predicted neutrino rates on the Earth depends both on the internal organization of the Sun and on the mechanism of oscillations. The Borexino detector is installed in Hall C of the Laboratori Nazionali del Gran Sasso (LNGS) in Italy. It is placed at 3800 m water-equivalent depth underground to reduce cosmogenic background. The sketch of the detector is shown in Fig. 1.12. It has onion-like geometry with a neutrino target in the very center. It consists of the 4.25-meter radius acrylic vessel (called inner vessel) filled with 278 ton of liquid scintillator (pseudocumene with PPO at a concentration of 1.5 g/l). Liquid scintillator has an unprecedented radiopurity that permits to detect neutrino using neutrino-electron scattering, the reaction that does not have a coincident tag. The vessel is surrounded by 2212 photomultipliers fixed on the stainless steel sphere. The position of the event could be determined by the time-of-flight algorithm, so one can choose the very internal volume, called fiducial volume, for the analysis. The external background has the smallest effect in this part of the detector. The space between the inner vessel and PMTs is separated by another vessel and filled with a buffer (pseudocumene + dimethyl phthalate as a quencher of scintillation). This liquid forms a passive shield from the external radioactivity.

All this construction is immersed in the water tank, that protects from surrounding radioactivity and serves as a Cherenkov detector for muon vetoing. 208 PMTs install on the outside surface of the steel sphere and walls of the tank to detect Cherenkov photons.

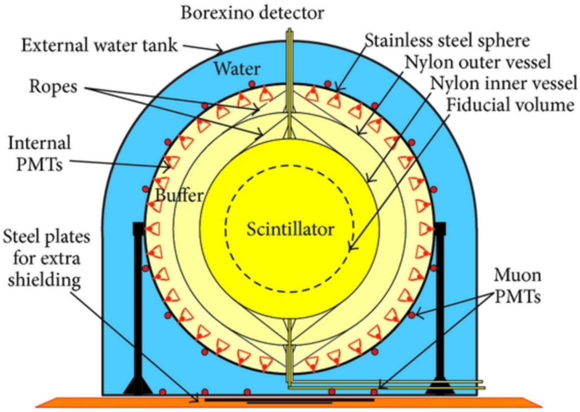

Figure 1.12: Sketch of the Borexino detector.

Borexino has a unique ability to observe neutrino-electron scattering of many solar reactions at the same time. It requires a full understanding of possible backgrounds. The correlations between backgrounds and electron recoil spectra may significantly reduce sensitivity. For different electron recoil spectra, different backgrounds are relevant.

First of all let us look at the neutrinos from primary pp-reaction at low energies ($E_\nu <$ 0.42 MeV) . Beta-emitter ^{14}C with $Q = 156$ keV is the main background for observing

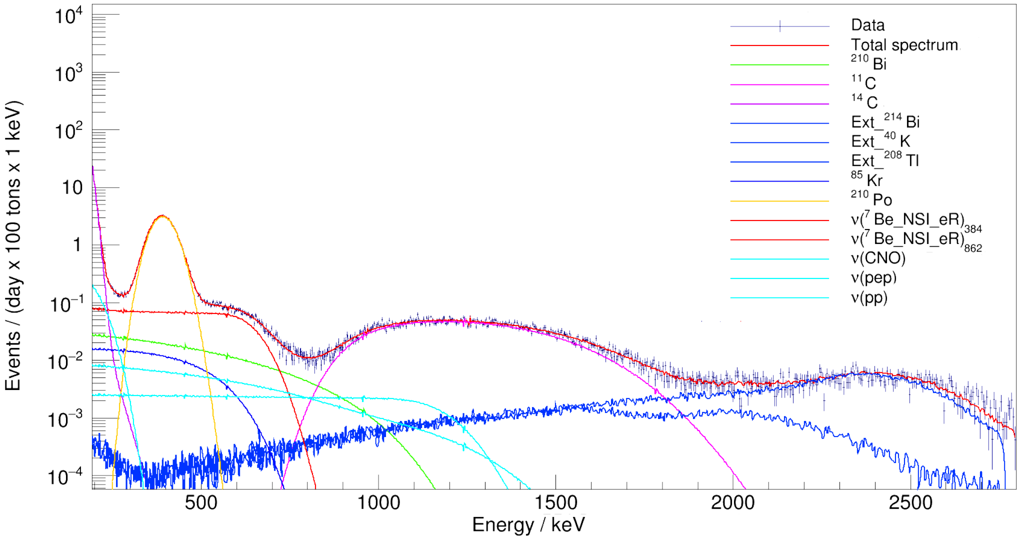

Figure 1.13: Example of fit of the energy spectrum obtained using the analytical method. The fit was performed using the $N_p^{dt_1}$ energy estimator (see text). The horizontal axis has been converted from $N_p^{dt_1}$ into units of keV.

this reaction. Since the rate of ^{14}C is quite high, the background from pile-up events [4] should be also taken into account.

Two mono-energetic lines $E_\nu = 384$ MeV and $E_\nu = 862$ MeV of ^{7}Be reaction are accompanied with backgrounds from ^{85}Kr ($\beta^-, Q = 687$ keV), ^{210}Bi ($\beta^-, Q = 1160$ keV) and from ^{210}Po ($\alpha, E = 5.3$ MeV).

The background from ^{85}Kr is quite serious since the shape of β-spectrum and its end-point are quite close to the step-like spectrum of ^{7}Be. It is possible to independently constraint the rate of ^{85}Kr based on the $\beta - \gamma$-coincidence technique with fast reaction:

$$\begin{aligned} ^{85}\mathrm{Kr} &\to {}^{85m}\mathrm{Rb} + e^- + \bar{\nu}_e \quad (Q = 0.173\,\mathrm{MeV}) \\ ^{85m}\mathrm{Rb} &\to {}^{85}\mathrm{Rb} + \gamma \quad (Q = 0.514\,\mathrm{MeV}, t_{1/2} = 10^{-6}\,\mathrm{s}) \end{aligned} \tag{1.84}$$

The position on energy scale of the peak from ^{210}Po is quenched in liquid scintillator by factor of about 10. Since the decay time ($T_{1/2} = 138.376(2)$ days) of the ^{210}Po is comparable with the scale of the data acquisition the decay profile could be observed. The events of ^{210}Po could be tagged by $\alpha - \beta$-discrimination. Some part (i) of events originate from the polonium dissolved in the liquid scintillator (ii), some part from the reaction:

$$^{210}\mathrm{Pb} \xrightarrow{\beta} {}^{210}\mathrm{Bi} \xrightarrow{\beta} {}^{210}\mathrm{Po}$$

where ^{210}Pb is a quite long-lived ($T_{1/2} = 22$ years) isotope of the ^{222}Rn chain dissolved in the liquid scintillator. So, potentially, if the ^{210}Po achieves enough small level

---

[4] Pile up consists of two decays that may happen at close time and could not be distinguished by read out electronics and reconstruction algorithm

one may separate i and ii and make an estimation of ^{210}Pb dissolved which is important for the constraint on ^{210}Bi rate. However, due to convective movements of the liquid scintillator, some new fractions of the ^{210}Po can enter into fiducial volume making the analysis more complicated. In order to reduce the mass transfer inside of the inner detector, the thermoregulation and control of the detector should be implemented.

The mono-energetic pep ($E_\nu = 1.44$ MeV)and CNO ($E_\nu < 1.74$ MeV) spectra are comparable in size, but shape is different. It gives an ambition to find the rates of these reactions separately. The shape of the CNO spectrum is very similar to the shape of the ^{210}Bi background discussed above. The independent information about ^{210}Po rate can break the ^{210}Bi- CNO correlation and may permit the measurement if secular equilibrium between the ^{210}Bi and ^{210}Po is achieved (which is not the case so far).

The main background at the endpoints of these reactions is cosmogenic ^{11}C. The isotope ^{11}C is produced by muon in reaction of spallation from ^{12}C. This reaction associated

The correlation between three events (muon, neutron capture by a hydrogen atom and ^{11}C decay) is a basis of Three-Fold-Coincidence technique. The TFC-algorithm evaluates the likelihood that an event is TFC candidate, considering the distance in space and time from a parent muon, distance from neutron and its multiplicity, muon dE/dx and the number of muon clusters in an event.

Based on this probability the data set is divided into two subsets: TFC-subtracted and TFC-tagged. They are fitted simultaneously in the multivariate fit.

Also the external gammas from isotopes ^{208}Tl, ^{214}Bi, and ^{40}K could penetrate inside of fiducial volume.

Electron recoil spectrum in the detector

The electron recoil spectrum in the detector is given as an integral of the solar neutrino spectrum and the differential cross section. Without taking into account the detector response, the spectrum is given by:

$$\frac{dR}{dT}(T) = A \times \sum_i \phi_i \int dE \lambda_i(E) \Big[\frac{d\sigma_e}{dT} P(E) + (c_{23}^2 \frac{d\sigma_\mu}{dT} + s_{23}^2 \frac{d\sigma_\tau}{dT})(1 - P(E)) \Big] \qquad (1.85)$$

where the constant $A = (N_{electrons}/[100 \text{ ton}])$ 86400 s day^{-1} includes the number of target electrons in 100 tons of the liquid scintillator mass and converts the rate from s^{-1} to day^{-1}. For the analysis of the Borexino spectral rates the unit *counts per day per 100 ton* is used ([cpd/100 ton]). So, $S(T)$ has a dimension [cpd/(100 ton MeV)].

ϕ_i - solar neutrino flux for the $i = pp$, ^{7}Be, pep, CNO in [cm^{-2} s^{-1}] and $\lambda_i(E)$ - solar neutrino spectrum normalized by unity. $\frac{d\sigma_\alpha}{dT}$ - differential cross section for different types of neutrino.

$P(E) \equiv P_{ee}(E)$ - survival probability for the electron neutrino with energy E. $c_{23} = \cos^2\theta_{23}$, $s_{23} = \sin^2\theta_{23}$ factors that take into account mixing between ν_μ and ν_τ.

^{7}Be electron recoil spectrum

^{7}Be flux is consist of two mono-energetic lines with $E_\nu^H = 0.862$MeV and $E_\nu^L = 0.384$MeV with relative contributions into total ^{7}Be-flux $\eta_H = 89.6\%$ and $\eta_L = 10.4\%$.

In this case $\lambda_{H/L}(E) = \delta(E - E_\nu^{H/L})$ and one may easily integrate exp. (4.53) over the neutrino energy E:

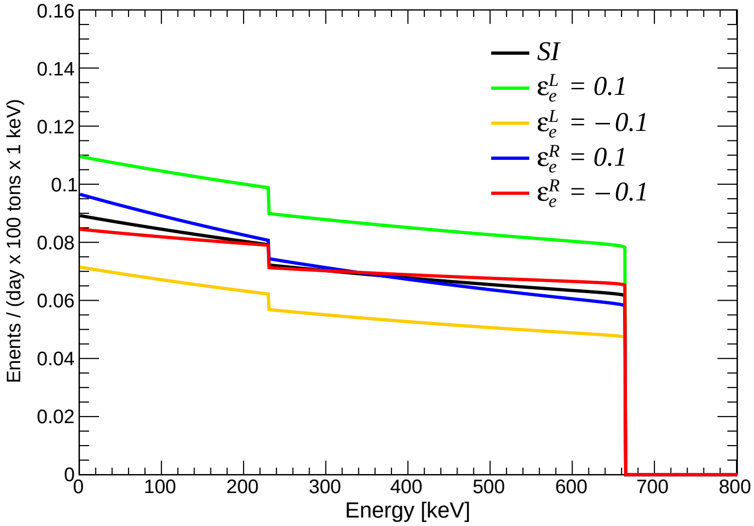

Figure 1.14: The distortion of the electron recoil spectrum, Eq. (4.53), for the two monochromatic ^{7}Be neutrino lines ($E_\nu = 0.384\,\mathrm{MeV}$ and $0.862\,\mathrm{MeV}$) due to non-zero values of ε_e^L and ε_e^R. The effect of limited energy resolution of the detector is not shown.

$$\frac{dR}{dT}(T) = A \times \sum_i \phi_i \Big[\frac{d\sigma_e(E_i,T)}{dT}P(E_i) + (c_{23}^2\frac{d\sigma_\mu(E_i,T)}{dT} + s_{23}^2\frac{d\sigma_\tau(E_i,T)}{dT})(1-P(E_i))\Big] \tag{1.86}$$

where $i = L/H$.

If we can denote the combination in brackets as $\langle\frac{d\sigma_i}{dT}\rangle$ and use the fact that $\phi_{^7Be} = \phi^H_{^7Be} + \phi^L_{^7Be} = \eta_H\phi_{^7Be} + \eta_L\phi_{^7Be}$:

$$S(T) = A \times \phi_{^7Be} \times (\eta_H\langle\frac{d\sigma_H}{dT}\rangle + \eta_L\langle\frac{d\sigma_L}{dT}\rangle) \tag{1.87}$$

This expression is used as a theoretical one to fit the data of Borexino. It should be converted from energy units into one of the observables by analytic detector energy response model (non-linear transformation of the energy scale and convolution with resolution). Then it should be normalized by unity to obtain the total number of events in the detector in cpd/100 ton as a normalization factor.

The modification of the ^{7}Be electron recoil spectrum for non-zero NSI constants are shown in Fig. 1.14. As one can see the right parameters ε_e^R modifies mostly the shape of the spectrum, while the left ε_e^L mostly the normalization (the total cross section).

pp-electron recoil spectrum

The next step is a modification of the *pp* neutrino electron recoil spectrum. It is important due to several reasons. Although this modification does not have such a strong effect as for ^{7}Be line, it could still improve the result; moreover, it has an influence on the correlations with background events (mainly on Krypton). It should be noted that in the analysis performed in Ref. [25] the pp-spectrum was not considered at all. However, experimental rates that were used in this analysis were observed including carbon and pp spectra into the fit as essential components (Ref. [80]).

In Fig. 1.15 two modified spectra are presented for left (a) and right (b) constants of NSI. Similarly to ^{7}Be-line, the left constant corresponds to the normalization and only slightly modifies the shape of the spectrum (a). At the same time, the right constant (b) changes the spectrum shape, banding it.

For the case of pp-neutrino spectral shape difference is quite small for a broad range of NSI parameters and, of course, is smeared by the energy resolution of the detector. However, the modification changes the relative number of events below and under the threshold of the detector (the choice of the lower range value of the fit). It leads to the change of the total event rate even if the shape under the threshold remains the same.

To study the role of pp-spectrum for the limits and study its interaction with other spectral components, the intermediate analysis of the χ^2-profile was conducted for $\varepsilon_{L/R}$ in case, when only pp spectrum was modified, and spectrum ^{7}Be had a standard form. As a limit on the flux, the High Z model value and uncertainty for the pp-flux was used. The uncertainty is only 0.6% which is less then FV systematic uncertainty that should also be included in the penalty term.

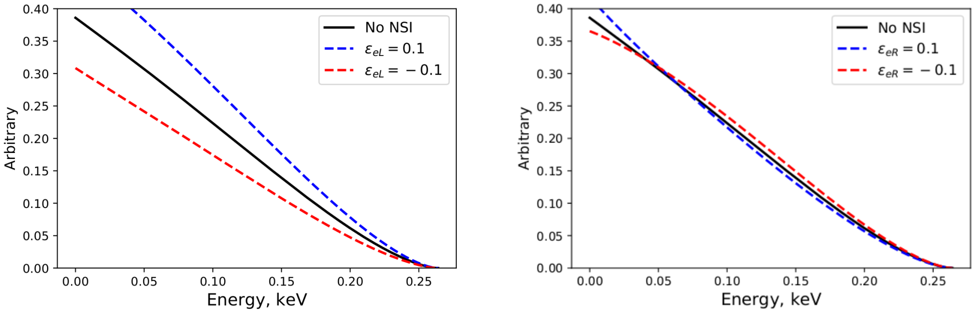

Figure 1.15: Modification of pp spectrum of recoil electrons for $\varepsilon_L = \pm 0.1$ (left) and $\varepsilon_R = \pm 0.1$ (right).

θ_{23} mixing angle

The question of the octant of the θ_{23} is not yet resolved. From the formula (4.53) it is evident that θ_{23} regulate the relatives contribution of the μ and τ neutrino into total signal. Being not relevant for the solar analysis, since $\frac{d\sigma_\mu}{dT} = \frac{d\sigma_\tau}{dT}$ in SM, it became important for the NSI analysis. Introducing this angle as a free parameter in the electron recoil spectrum may reduce the sensitivity to $\varepsilon_\tau^{L/R}$.

If we chose the "negative spectra" approach then we can split the standard and non-standard part for τ-lepton:

$$c_{23}^2 \frac{d\sigma}{dT} + s_{23}^2 \frac{d\sigma}{dT} + s_{23}^2 \frac{d\sigma_{NSI}}{dT} \tag{1.88}$$

$$\frac{d\sigma}{dT} + s_{23}^2 \frac{d\sigma_{NSI}}{dT}$$

If we make a recalculations into the flux, then the uncertainty of the θ_{23} goes into the ration of the cross-sections:

$$R \to \frac{\sigma(\varepsilon)}{\sigma(0)} \to \phi$$

We can, in principle, add uncertainty into systematic error or probably try to add the uncertainty of cross section into the total uncertainty of the sum of the flux.

In Ref. [25] article, the authors fixed at maximum mixing which was a simplification. We can choose the unfavorable mixing angle $\theta_{23} < \pi/2$, when the contribution of the τ neutrino in the total cross section is less than μ.

Rate calculation

The total rate could be obtained by integrating the expression (4.53) over kinetic energy of the electron. Note that even though the detector has a hardware threshold, the bottom limit of integration is 0. It means that the total rate contains the events below the threshold as well. This choice is quite convenient since performing the fit of the experimental spectrum we would like to obtain the values that are independent of the threshold choice.

The Jiangmen Underground Neutrino Observatory

JUNO (Jiangmen Underground Neutrino Observatory) is a multipurpose reactor experiment to study antineutrino oscillations with a baseline about 53 km (Ref. [9]). The main goals of the experiment are to determine the neutrino mass hierarchy, accurate measurement of the oscillation parameters and the study of reactor neutrino fluxes. Besides, it is also possible to deal with a large number of other physical problems, such as the study of solar, atmospheric and geoneutrino, detection of neutrinos from the supernova and search for exotic particles and processes, such as sterile neutrinos and the study of non-standard interactions. The experiment will be located at a depth of 700 meters underground in southern China in the county Kaiping District Tszyanmyn and will observe a flow of antineutrinos from a reactor complex Tai (Taishan) and Yangjiang (Yangjiang) using 20 kt liquid scintillation detector with a designed energy resolution of 3 % (1 MeV).

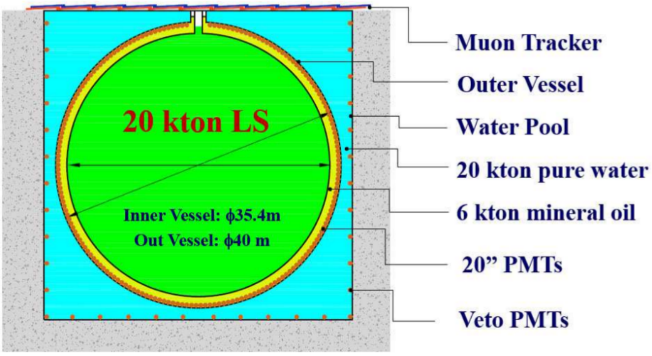

Figure 1.16: A schematic view of the JUNO detector. Taken from Ref. [9] and modified to represent the current changes in design.

One of the first experiment of such configuration for the neutrino mass hierarchy measuring was proposed in Ref. [81] and [82]. As was shown in [82] reactor experiments with intermediate A baseline can determine both Δm^2_{sol} and θ_{sol} with high precision if the solution of solar neutrino problem is high-LMA. It was shown that if the resolution and statistics of the experiment is good enough, the experiment became sensitive to Δm^2_{atm} as well and that an "interference" between the Δm^2_{sol} and θ_{sol} driven oscillations can be used determine the neutrino mass hierarchy: a choice of the mass hierarchy appears as a difference in the phase of the oscillation. Spectra for the case of the normal and inverse hierarchies are presented in Fig. 1.17.

Linear alkylbenzene (LAB) is used as a detection target mixed with 3 g/L PPO and 15 mg/L bis-MSB as fluor and wavelength shifter, respectively. Liquid organic scintillators could be purified to achieve high transparency and very low radioactivity.

Liquid scintillator is placed in the spherical acrylic vessel ($r = 17.7$ m) forming the Central Detector. The light emitted by the liquid scintillator is registered by 17000 20-inch photomultipliers installed on another spherical stainless steel structure ($r = 19.5\,\mathrm{m}$) the gap between the acrylic sphere and PMT's support sphere is filled by the ultra-pure liquid water as a buffer to protect them from the intrinsic radioactivity of the PMT, electronics and support components. The support structure is built on the bottom of a pool with ultra-poor water that serves as a Water Cherenkov Detector and as a protection

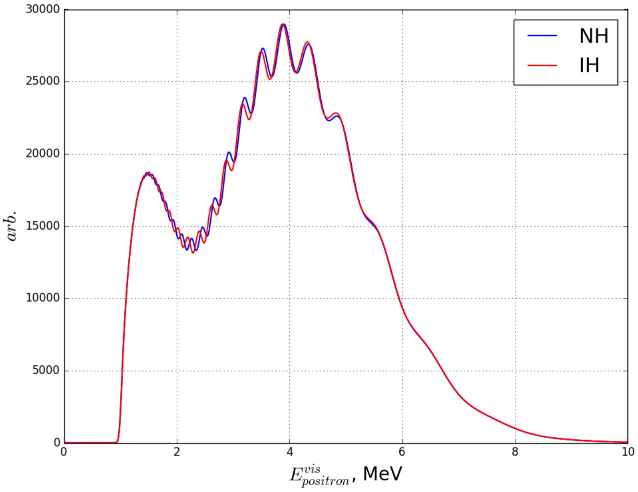

Figure 1.17: Visible spectrum of positrons produced in IBD reaction with antineutrino from a reactor for the cases of normal (NH) and inverse (IH) hierarchies. The distance reactor-detector $L = 52474$ m. Oscillation parameters: $\Delta m^2_{21} = 7.54 \cdot\ 10^{-5}$, $\Delta m^2_{ee} = 2.43 \cdot\ 10^{-3}$, $s^2_{12} = 0.307$ and $s^2_{13} = 0.0242$ (Ref. [10]). Energy resolution was modeled by (1.5) with $a = 0.03$ and $b = 0, c = 0$.

from the external rock radioactivity. An additional array of PMT's is arranged on the walls of the pool to register Cherenkov light emitted by muons. On the top, plastic scintillator strips detector is placed for muon's direction determination. A Water Cherenkov Detector, Top Tracker as well as Central Detector are forming the system for muon detection and stud the background induced by muons. More information on the detector could be found in Ref. [9],[83],[84].

The main challenges for JUNO are technological. In order to achieve the declared energy resolution, the requirements on PMT photocathode coverage, photocathode quantum efficiency and transparency are high. JUNO is very similar to KamLAND in design, but twenty times larger in mass (20 kton). The JUNO experiment aims are to increase photon statistics up to 1200 photoelectrons per MeV to achieve 3 % at 1 MeV resolution by increasing the scintillator light yield (× 1.5 bigger as compared to KamLAND), increasing the total photo-cathode coverage (× 2.3), and by increasing the efficiency of each photo-multiplier (× 2.0) relative to those of KamLAND. The number of 20-inch PMTs in the inner detector is 18000. Their stable and homogeneous operation is quite nontrivial engineering problem (Ref. [83],[9] and [84]).

As it was mentioned in Ref. [2] the constraints on detector uniformity and linearity will likely require the development of new methods to calibrate the detector response to positrons. As we will see further these effects leads to deformation of the energy scale of positrons and therefore distort observed reactor neutrino spectrum, making impossible a conclusion about experimental spectrum whether the neutrino mass hierarchy is normal or inverted. The declared value of the energy resolution (3 %) is a threshold of sensitivity. Deterioration of energy resolution or/and uncertainty of the energy scale will lead to the impossibility of separating the neutrino mass hierarchy (Ref.[9] and [2]).

Currently, an experimental hall and the JUNO facility are under construction. Data acquisition is scheduled in 2020.

The visible spectrum is smeared by an energy response of the detector which could

Table 1.5: The meaning and the typical range of the parameters from expression (1.89).

Parameter	Meaning	Definition	Typical value at 1 MeV
a	Statistical term	$\frac{1+v_m}{\sqrt{N^{1\ \text{MeV}}_{p.e}}}$	0.029-0.036
b	Spatial/temporal variations	-	-
c	Dark noise	$\frac{DCR\times\Delta t_{window}\times N_{PMT}}{N^{1\ \text{MeV}}_{p.e}}$	~ 0.0001

be parameterized as

$$\frac{\sigma_E}{E} = \sqrt{(\frac{a}{\sqrt{E}})^2 + b^2 + (\frac{c}{E})^2} \tag{1.89}$$

and it is supposed to be less then $3\%/\sqrt{1\ \text{MeV}}$. Often in analysis only one "effective" term $a = 0.03$ is used as a reference.

The meaning and typical range of the parameters is listed in Table 1.5. The a constant is mainly determined by the average relative variance of PMT's gain v_m and the number of collected photoelectrons per 1 MeV of released energy (so-called photoelectron yield) $N^{1\ \text{MeV}}_{p.e.}$ as:

$$a \simeq \frac{1+v_m}{\sqrt{N^{1\ \text{MeV}}_{p.e.}}}$$

For JUNO we expect $v_m \simeq 0.1 - 0.3$ (typical values for PMTs) and $N^{yield}_{p.e.} \simeq 1100 - 1200$ p.e./1 MeV Ref. [83]. Finally we have:

$$a \simeq 0.029 - 0.036$$

The value of the non-stochastic constant b is not well defined. It includes a variety of factors such as the detector uniformity and vertex resolution, detector stability and others (Ref. [9]).

Constant c is related to the dark counts of PMTs ($N_{PMT} = 17000$) and could be estimated as:

$$c \approx \frac{DCR \times \Delta t_{window} \times N_{PMT}}{N^{1\ \text{MeV}}_{p.e}} \sim 0.01,$$

with typical $DCR \approx 2$kHz and readout time window $\Delta t_{window} = 200$ ns.

The studies of the sensitivity of the detector to the neutrino mass hierarchy determination showed the relative importance of the energy resolution terms a, b, c: the influence of b term is 1.6 times larger than the a term, and c is less significant than a by factor of 1.6 (Ref. [9]).

JUNO detector has a potential for searching NSI with different strategies: solar neutrino, experiments with reactor antineutrino that we will discuss further as well as experiments with internal compact neutrino sources which are outside of the scope of this work. The first possibility is the solar neutrino approach discussed above for Borexino and improvement of the result obtained in this work. This approach will crucially depend on the realization of the solar neutrino program in JUNO and measurement of the flux of ^{7}Be.

CHAPTER 2

Energy response of the large liquid scintillator detectors

Importance of energy scale and energy resolution for large-scale liquid scintillator experiments

This chapter is dedicated to some specific questions related to the large-scale liquid scintillator detectors: energy scale and energy resolution. They are highly relevant to the detector performance being important parameters for many physical problems.

In the last 20 years, the technologies associated with the construction of the large-scale liquid scintillator detectors made a big step forward opening a new frontier on the field of particle physics, in particular in neutrino physics. New, challenging scientific programs encourage researchers to study the detector energy scale and energy resolution in detail and deeply examine phenomena which are at the base of particle detection. Advanced analysis techniques and accurate MC simulations are of high demand. Further, we will discuss factors which determine energy scale and energy resolution. In particular, we will focus on the fundamental contribution of liquid scintillator into them. In case of a liquid scintillator detector non-linearity of the energy scale for a given type of particle depends on *how* the particle *deposes* its energy in the liquid scintillator and *how* its energy is transferred to the light that could be detected. Basic processes of deposition of the energy are ionization and radiative energy losses (Sec. 2.2). Transfer of energy into visible light is guided by two processes: scintillation and Cherenkov radiation. Both of them contain non-linearity and will be discussed further (Sec. 2.4 and 2.5).

Until the model of the energy scale of the detector is constructed the fit of the experimental spectrum can not be performed. The energy resolution is another crucial characteristic of the detector. With assumption that the number of detected photons (number of photoelectrons) follows Poisson distribution with mean $N_{p.e.}$ and standard deviation $\sqrt{N_{p.e.}}$, usually relative energy resolution is estimated by means of the number of photoelectrons at 1 MeV of particle's energy as:

$$\frac{dE}{E} \sim \frac{1}{\sqrt{N_{p.e.}}} \tag{2.1}$$

Hence the more photoelectrons is collected the better energy resolution is. We can find theoretical limit for organic liquid scintillators [1]. The characteristic light yield for such scintillators is about 10^4 phot/MeV. Supposing ideal unrealistic 100 % light detection efficiency we get the same amount of photoelectrons 10^4 p.e. Following the expression (2.1) we can find a theoretical limit on the energy resolution:

$$\frac{dE}{E} \sim \frac{1}{\sqrt{N_{p.e.}}} =\sim \frac{1}{\sqrt{10^4}} = 0.01$$

that is 1 %. Considering practical estimation for the most advanced photon detection devices (2018 year) with quantum (detection) efficiencies 43 % for PMT and 60 % for Si-PM (Ref. [85] Table 1) and high light collection efficiency 70-80 % , one can achieve 3000-4800 p.e./MeV and 1.4-1.8 % energy resolution.

However, other non-Poissonian factors may introduce additional contributions to resolution. Previously the effective formula for the energy resolution was illustrated by expression (1.89) in the context of JUNO detector description.

Theoretical aspects of the model of the energy resolution will be discussed further in Sec. 2.7. Section 2.8 is dedicated to experimental investigation.

---

[1] such as pseudocumene for Borexino and linear alkylbenzene for JUNO

Energy resolution smears registered energy spectrum making its distinct features less visible. To have a good energy resolution is especially important in the presence of background spectra when distinct spectral features of the signal and background facilitate its separation.

A very vivid illustration is the spectrum of Borexino (Fig. 1.13). Looking at the experimental points one may notice the clear presence Compton-like shoulder of $\nu(^{7}\text{Be}) - e^{-}$ scattering. The better energy resolution is the more distinct a sharp edge of this step-like spectrum. It is especially important in the presence of background such as ^{85}Kr (β^{-}-emitter) to distinguish two spectra. A little bit less evident, but still of high importance, is a distinction between spectral shapes of ^{14}C ($E_{end-point} \sim 156.5$ keV) and electron recoil spectra from pp neutrino ($E_{end-point} \sim 263$ keV). Smeared by energy resolution, the endpoints of the spectra are almost identical though spectral shapes are different. Thanks to an excellent energy resolution of the detector this small difference could be utilized for spectral separation in the fit. Finally, for pep and CNO spectra energy resolution issue is also highly relevant since the energy resolution smears step-like pep spectrum and it becomes very similar to CNO spectrum.

Sometimes distinct spectral features determine physical parameters of interest. A bright example is the JUNO experiment that has neutrino mass hierarchy determination as a primary goal. The ability to discriminate between two hierarchies strongly depends on the resolution of the detector. As a final benchmark, the value 3 % at 1 MeV is used. The detector detection efficiency should be significantly increased as compared to all previous liquid scintillator experiments to achieve this resolution. Any additional contribution of non-Poisson nature may reduce sensitivity, even if nominal light detection efficiency is achieved. Hence the energy resolution of the detector should be carefully examined.

Special attention deserves a non-Poisson contribution into the total energy resolution from the liquid scintillator by itself called *intrinsic energy resolution*. Being well known and robustly measured in inorganic solid scintillators [86] it is still an open question for liquid organic scintillators. As a working hypothesis, we assume that two main factors generate an intrinsic resolution are the production of secondary particles (delta-electrons) [2] with different energy and non-linear response to each secondary particle. In this study, we consider an experimental approach to intrinsic energy resolution investigation. The size of the intrinsic energy resolution effect, along with Poisson statistics of detected photons, determine a theoretical limit for the energy resolution for a given liquid scintillator with expression (2.1).

As it was shown in Ref. [87] the presence of uncounted residual non-linearity could degrade the possibility for determination and even, in the worse case may lead to the wrong mass hierarchy determination. A proper understanding of the response of the detector can fix the energy scale and significantly reduce uncertainties. Independent laboratory measurement of liquid scintillator non-linearity may serve as complementary to detector calibrations. The same experimental technique as for intrinsic resolution measurement could be used for non-linearity measurement as well.

In this chapter we describe [3] the energy model of the detector and propose the method for independent laboratory measurement of the parameters for non-linearity and energy resolution.

---

[2] For high-Z scintillators production of X-rays is also possible

[3] Strictly speaking here I consider the system (liquid scintillator - PMT) in a most general way. For the description specific for large liquid scintillator detectors see Ref. [88]

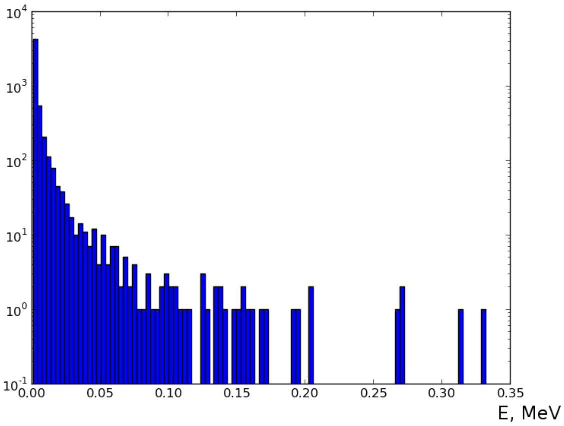

Figure 2.1: The distribution of the secondary delta-electrons for 1 MeV electron in benzene (100 electrons were generated)

Interaction of electrons, positrons and gamma with the media

Electrons and positrons

Ionization losses

Propagation of the particles of different types significantly differs from each other. Let us first have a look at energy losses for electrons. Due to a small mass of electron the change of its momentum is large and could significantly change its direction during the propagation as well as emit radiative gamma quanta.

The Bethe-Bloch formula for ionization losses:

$$-\frac{\overline{dE}}{d(x\rho)} = \frac{K}{2}\frac{Z}{A}\frac{1}{\beta^2}(ln(\frac{m_e^2\beta^2\gamma^2(\gamma-1)}{2I^2})+ln2(2\sqrt{1-\beta^2}-1+\beta^2)+1-\beta^2+\frac{1}{8}(1-\sqrt{1-\beta^2})^2) \tag{2.2}$$

Energy loss (stopping power) for electrons in benzene is shown in Fig. 2.6. Energy loss for electrons and positrons are similar in a wide range of energies and only for energies smaller then 1 keV they are significantly different [89]. Therefore the formula basically could be applied to both of them. Another difference between energy losses of electron and positron is that for positrons there is some probability to annihilate on-flight before achieving thermalization (Ref. [90]).

Delta-electrons

Some secondary electrons may receive a significant part of the energy during the ionization losses. Such electrons are called δ-electrons. These electrons produce ionization as well, and their tracks are visible in emulsion or a cloud chamber.

Fig. 2.1 shows the distribution of the delta-electrons produced by 1 MeV electron in benzene. As one can see the delta-electrons with energy higher than 10 keV (first 4 bins) are relatively rare.

The fluctuations of the number of the high energetic delta-electrons may give the contribution in intrinsic resolution.

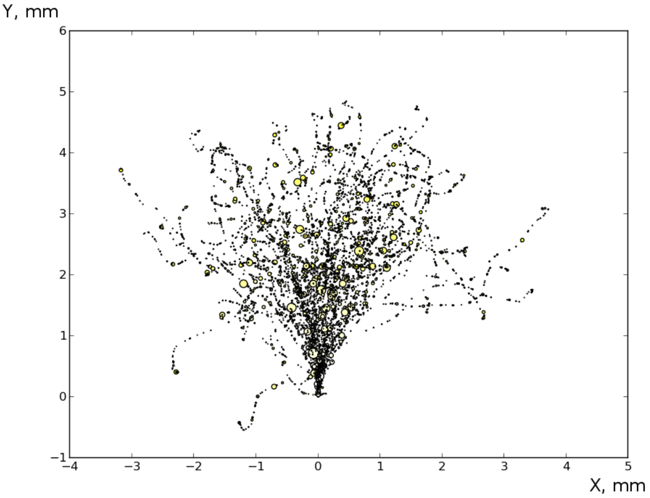

Figure 2.2: Simulated spatial distribution of the events of ionization for 100 electrons with the energy 1 MeV (GEANT 4 Penelope physics model)

In Fig. 2.2 spatial distribution of secondary electrons (centers of ionization) for 1 MeV electrons in the liquid scintillator is presented. The propagation length is less than 5 mm.

Radiative losses (bremsstrahlung)

At higher energies collisions of electrons with atomic nuclei and electrons of the shells lead to the emission of the electromagnetic radiation. The bigger the energy of electron the more significant the contribution from the electromagnetic radiation into the total energy losses (Fig. 2.6). The specific kinetic energy of electron when ionization and radiative energy losses are equal is called critical energy. It is approximately:

$$T_{crit} \approx \frac{800\ \mathrm{MeV}}{Z+1.2}, \tag{2.3}$$

where Z is an atomic number of the media.

Liquid organic scintillators mainly consist of hydrogen ($Z = 1$) and carbon ($Z = 6$). So the critical energy should lie in the interval 110-670 MeV.

The maximal part of the radiative losses could be estimated by well known empirical approximation:

$$\frac{(-\frac{dE}{dx})_{rad}}{(-\frac{dE}{dx})_{ion}} \approx \frac{T[\mathrm{MeV}]Z}{800}, \tag{2.4}$$

and it is 0.6-3.75 % for the energy 5 MeV in liquid scintillator.

Gamma

The way how gamma rays interact with the media is determined by four processes: photoelectric effect, Compton scattering and pair production.

Photoelectric effect

is a process of interaction of the photon with one of the internal electrons of the atom (bounded with energy I_b) when all energy of the photon E_γ is transmitted to the electron:

$$T_e = E_\gamma - I_b \tag{2.5}$$

The photoelectric effect is impossible on the free electron because it breaks the law of the energy-momentum conservation: for the photoelectric effect, it is significantly important the connection of the electron with the atom. The cross section for given energy has a maximum for the electrons of the K-shell and decreasing for L, M and so on.

$$\sigma_{phot} \sim Z^5 \tag{2.6}$$

The photoelectric effect is very relevant for the light gamma in the high-Z materials such as lead. In the liquid organic scintillator, it is relevant for the energies below 100 keV.

Compton effect

While the energy of gamma increases, the Compton scattering process became more relevant. It is the main process in the energy region 0.1-1 MeV. In sizeable liquid scintillation detectors gamma quanta usually experience several Compton scattering until it reaches the energy of the photoelectric dominance.

$$\sigma_{phot} \sim \frac{Z}{E} \tag{2.7}$$

Pair production

The threshold of the electron-positron pair production is equal to 1.02 MeV and how one can see from the relation the cross section logarithmically grow with the grows of energy:

$$\sigma_p \sim Z^2 \log(E) \tag{2.8}$$

Energy and spatial distribution of secondary particles

Energy distribution for Compton and photo-effect electrons are shown in Fig. 2.4.

The length of the track of the gamma quanta with the energy 1 MeV in liquid scintillator could be up to 1.5 m long, but the Compton scattering significantly reduces the effective distance of propagation. Fig. 2.3 illustrates the interaction of 1 MeV gamma with the media, the majority of the events could be located in the sphere with a radius 0.5 m.

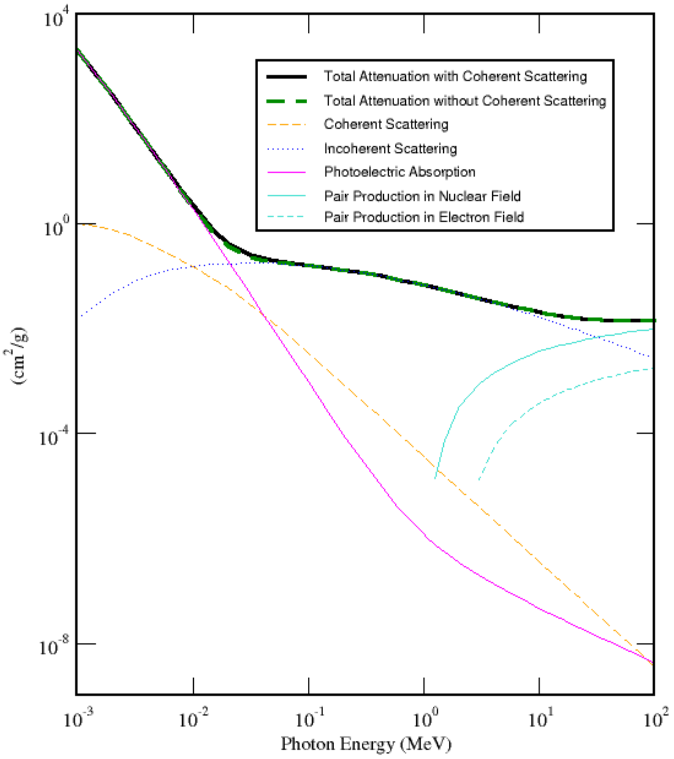

Figure 2.3: Attenuation coefficients for gamma interaction in water (adopted from Ref. [11])

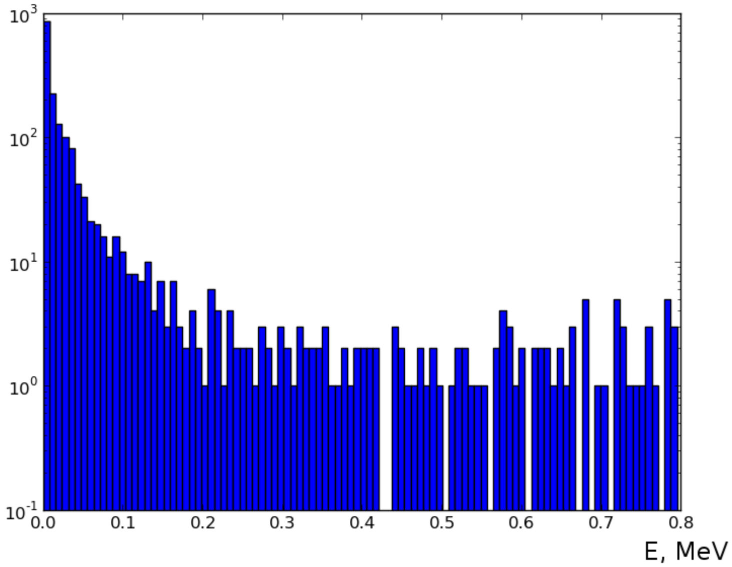

Figure 2.4: The distribution of the secondary electrons for 1 MeV 100 gamma

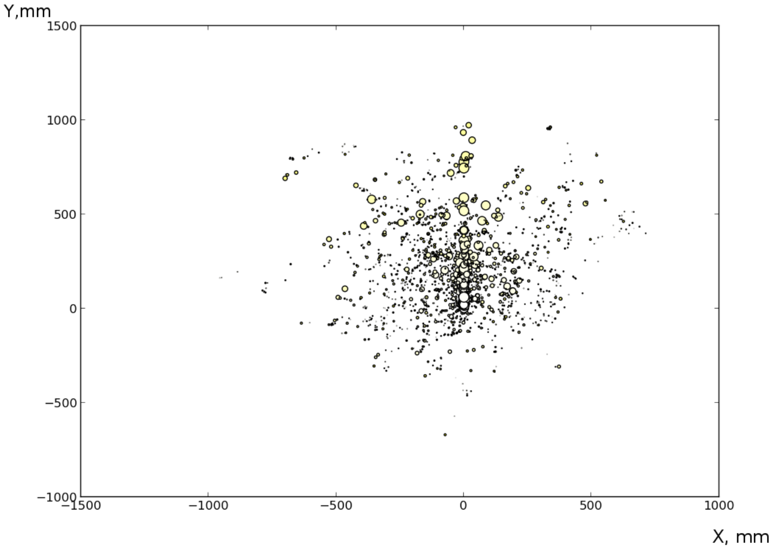

Figure 2.5: Spatial distribution of Compton events and photoelectron effect (6 % from the total event number) for 100 photons with the energy 1 MeV in benzene (simulated in GEANT4)

Neutrino energy estimation

The energy of incident neutrino could be reconstructed from the products of reactions of neutrinos with matter, where in case of elastic neutrino scattering and IBD an electron (positron) is a final-state particle. The incident electron loses its energy in the liquid scintillator through collisions with other electrons, which causes ionization of the media. The energy of the electron is not measured directly, but rather *estimated* through some physical processes: the collection of the ionization charges (for projection chambers), amount of scintillation light or Cherenkov emission, and other processes. We denote it as E_{vis}.

For liquid scintillator and Cherenkov detectors one can choose the total light yield (number of registered photons) as an estimator E_{vis} (visible energy). The relation between the energy of an incident particle E_{true} and the energy estimator E_{vis} is determined by the detector energy scale that, in principle, could be parameterized analytically [91]. In case of an ideal detector energy scale, the estimator is strictly proportional to the energy.

In the real case, several effects make energy estimation more complicated, and electrons with different energies have different coefficients of proportionality with the estimator: the model became nonlinear.

One may construct an analytical model $E_{vis}(E_{true})$ of the energy scale of the liquid scintillator or Cherenkov detector, incorporating the effects of the quenching and Cherenkov emission.

Ionization quenching

Ionization quenching leads to a non-linear dependence of the number of photons per unit of the track length from the differential energy losses:

$$\frac{dL}{dE} \backsimeq Y_p \frac{1}{1 + kBdE/dx} \tag{2.9}$$

Here the dL indicates the number of photons per unit of deposed energy, Y is a light yield, dE is energy losses of the particle and kB in [cm/MeV] is a characterizing Birks' quenching constant [4]

The value of kB constant for heavy particles and low energy electrons depends on many factors: type of scintillator, the presence of dopants, temperature, type of particle and its energy as well as conditions of measurements [93].

In Fig. 2.6 the stopping power for benzene is presented. As one may see the stopping power is much higher for low energy electrons. It leads to suppression of the light emission at lower energies. In the zone about 1.5 MeV the total losses achieve the minimum and then steadily increase.

---

[4] it is a multiplication of two constants k and B, but they are indistinguishable in this experimental case (see Ref. [92])

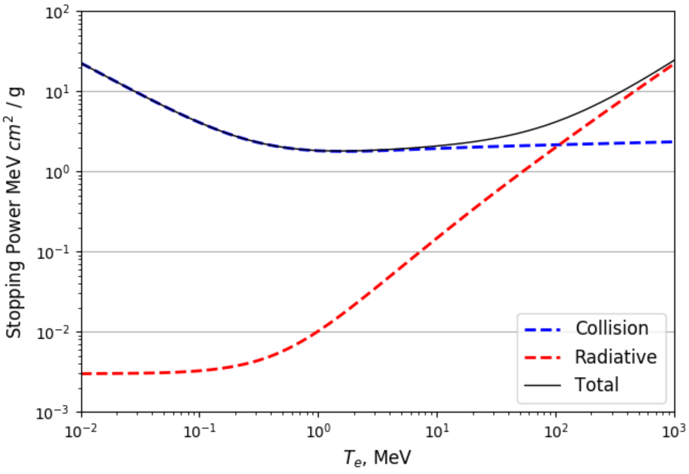

Figure 2.6: Ionization (blue dotted line) and radiative (red dotted line) stopping powers in benzene that determine energy losses of electrons. At low energies (< 1 MeV) ionization losses are maximal. In the middle and high range they are almost constant. At higher energies radiative losses become relevant. Adopted from Ref. [12]

The main problem of the verification of the expression (2.9) is that is has a differential form, while the observable values is an integral of this expression:

$$L(T, kB) = Y_p \int_0^L dx \frac{dE/dx}{1 + kBdE/dx} = Y_p \int_0^T \frac{dE}{1 + kBdE/dx} \tag{2.10}$$

Note that the derivative of (2.10) is exactly expression (2.9). [5]

Theoretical curves of energy scale determined by liquid scintillator $L(T, kB)$ for different values of kB in the range 0.0011 - 0.03 cm/MeV are shown in Fig. 2.7 and arbitrary light yield. The $kB = 0.011$cm/MeV was reported by Borexino collaboration in Ref. [91]. As one may see the effect is very small and practically for energies higher than 100 keV the response became linear (try to compare it with plot Fig. 8 from Ref. [91]). The smaller kB constant, the faster linear response is restored. Though curves in the range with energy higher than 100 keV are linear, they do not cross the origin of coordinates and should be parameterized with a function $L(T, kB) = aT + b$. The presence of the constant term could be erroneously treated as "non-linearity" of the response (for example, error in baseline determination or dark pulses subtraction). It is easy to demonstrate that the ratio a/b doesn't depend on the light yield and it is a function of only kB.

An important conclusion could be derived: the energy range of quenching non-linearity presence depended on the value kB, being relevant in the range $T < 100$ keV for practically important $kB < 0.03$ cm/MeV.

---

[5] It is more often to use the function $Q_\beta(E, kB)$ for quenching non-linearity parameterization which could be defined as [91] :

$$L(T, kB) = Y_p Q_\beta(T, kB) T \rightarrow Q_\beta(T, kB) = L(T, kB)/(Y_p \times T) \tag{2.11}$$

Though the function $Q_\beta(T, kB)$ may create a wrong impression about the linearity of the energy response and overestimation of the energy range of its presence. Compare Fig. (2.7) with $L(T, kB)$ and Fig. 8 from Ref. [91] with $Q_\beta(T)$.

This conclusion has a significant impact on the strategy of the measurement of kB in laboratory suggesting the range up to 100 keV to be sufficient for examination.

It is a critical observation since at energies higher than approximately 200 keV Cherenkov radiation contribution also became relevant. Small kB value guarantee that two effects could be completely decoupled and studied separately.

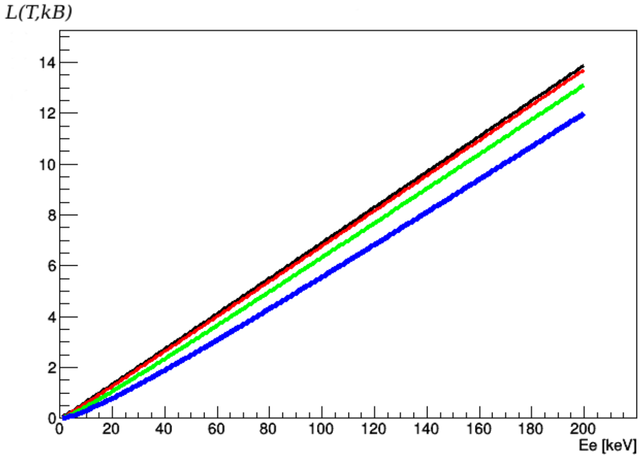

Figure 2.7: Curves for the quenching model (expression (2.10)) for different values of kB (in cm/MeV; 0.0011 - black, 0.003 - red, 0.011 - green (Borexino), 0.03 - blue)

Also, the experimental spectrum by itself could provide information about an energy scale and energy resolution if the "true" energy spectrum for a given process is known.

For large liquid scintillator experiments the parameter kB of non-linearity could be extracted from calibrations. In Ref. [91] kB in pseudocumene was determined with 6 % relative experimental error by means of analytical and Monte Carlo methods: $kB = 0.0109 \pm 0.0006$ cm/MeV and $kB = 0.0115 \pm 0.0007$ cm/MeV, correspondingly, in full agreement between them.

An independent laboratory measurement could be of particular importance. One may guaranty a good understanding of the liquid scintillator response if the results of calibration and laboratory measurement are consistent. Several attempts of laboratory measurement and such comparison (Ref. [94]) were performed, but no stable result was reported yet.

Cherenkov effect

A charged particle starts to emit light when it propagates with speed higher than the speed of light in a media. This phenomenon is called Cherenkov (Vavilov-Cherenkov) effect (Ref. [95]). Cherenkov effect also contributes to the non-linearity and intrinsic resolution of the scintillator. The question about the Cherenkov contribution into the total light yield is both important for the analysis and Monte Carlo since it dramatically influences the energy scale of positrons, electrons and gamma quanta. As it was told in the previous section, we stand by the idea of an effective decoupling of the Cherenkov light from the scintillation light in order to measure the quenching induced non-linearity by itself.

The condition for Cherenkov emission of the photon with a given wavelength λ is related to the value of the refractive index $n(\lambda)$ of the media and velocity of the charged particle $\beta = v/c$ (Ref. [96]).

$$n(\lambda) > 1/\beta \tag{2.12}$$

Since $n(\lambda)$ depends on the wavelength of the emission λ the threshold, in general, will be different for different wavelengths.

The spectrum of the Cherenkov emission could be found by the formula for an average number of photons emitted in the photon energy interval ϵ while the particle is moving the distance dx (Ref. [97], [96]):

$$\frac{dN}{dxd\epsilon} = \frac{\alpha z^2}{\hbar c}(1 - \frac{1}{n^2\beta^2}) \approx 370 z^2 \frac{\text{photons}}{\text{eV cm}}(1 - \frac{1}{n^2\beta^2}) \tag{2.13}$$

To find the final emission spectrum and number of photons for a light charged particle such as an electron one needs to integrate this relation over the particle track and energy of photons.

Fig. 2.8 helps to understand the evolution of the Cherenkov emission spectrum with energy. Two subplots are illustrating how condition (2.12) works for the different kinetic energy of the particle T and different wavelengths λ. On the right panel, the red line represents the dependency of the factor $1/\beta$ from the kinetic energy T. This plot corresponds to the right part of the condition (2.12). The left subplot represents the dependency of the refractive index from wavelength λ of the photon and corresponds to the left part of the condition (2.12). To obtain the spectrum of the Cherenkov emission for a given kinetic energy T one needs to find the corresponding point $1/\beta(T)$ by the right subplot and plot the horizontal line through this point. Some peace of plot of the left subplot may be above the horizontal line. It means that the condition (2.12) is satisfied in this range.

As one may see the emission starts from the energy about 80 keV for wavelength 200-300 nm. While energy increases the condition (2.12) became valid for longer wavelengths until the spectrum covers the range of the PMT's sensitivity entirely at approximately 180 keV ($1/\beta \approx 1.5$) and then the spectrum remains unchanged at higher energies.

As we see the spectrum of the Cherenkov light could be calculated if the measurement for refractive index $n(\lambda)$ as a function of wavelength λ is provided. However, based on these calculations it is not possible to calculate the contribution of the Cherenkov light into the total registered light expressed in photoelectrons. Depending on the λ the propagation of photons became different. The liquid scintillator is entirely transparent to the long-wavelength part of the Cherenkov spectrum, and the photons of this wavelength have a chance to achieve the photo-cathode directly. The liquid scintillator absorbs shorter-wavelength part of the Cherenkov light and then re-emits it with some probability (Ref. [98]). The fact that the liquid scintillator is multi-component systems of the solvent and wave-sifters makes a proper description complicated. Therefore, even if the initial number of the photons is known as the estimation of the contribution into the light- and photo-electron yields is quite problematic. The absolute light yield of the liquid scintillator by itself is also hardly measurable value [6]. On the small setup scale, the directionality of the Cherenkov light may become relevant (though only for the part that is not absorbed-re-emitted in the liquid scintillator, since re-emitted light is isotropic).

---

[6] Usually Cherenkov photons are also included into the absolute light yield of the scintillator because in most practical cases they are not distinguishable from scintillation photons. Here we underline that we use this term as a property of the liquid scintillator by itself, so Cherenkov photons are excluded from it

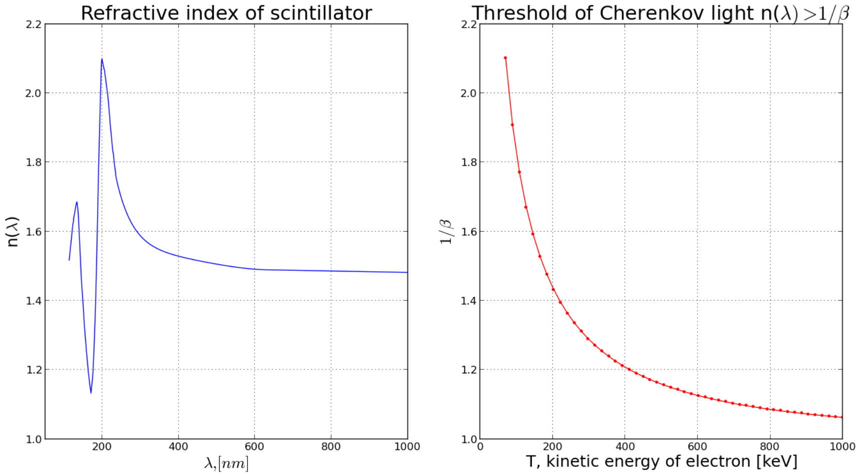

Figure 2.8: Refractive index of the liquid organic scintillator (left) and $1/\beta$ for electrons as a function of kinetic energy (right). Refractive index is reproduced from [13] and was obtained by joining of measurements for pseudocumene (PC) and benzene (in the region 150-210 nm) as an approximation.

Thus, the relative contribution of Cherenkov and scintillation photons is quite hard to determine. The situation became even more dramatic since the photon's propagation, and evolution of the spectrum in small experimental setup and a large scintillator detector is different. It makes Cherenkov emission non-invariant from one setup to another. As a consequence, measurements of this contribution on a small scale could not be directly applied on a large scale. For Borexino experiment the contribution of Cherenkov into the total light yield was found to be about 5 % at 1 MeV (in pseudocumene + PPO 1.5 g/l) (Table XVI in Ref. [91]) . Let us take this value as a reference to the order of magnitude.

The dependence of the number of detected Cherenkov photons on energy $L_{cher}(T, n)$ (Cherenkov factor) could be found analytically. However, as it was told to scale this dependence with respect to scintillation is not trivial: abovementioned re-emission probability depends on the wavelength [7] and Cherenkov evolution depends on the kinetic energy of the particle.

The Cherenkov factor $L_{cher}(E, n)$ could be found by integrating $\frac{dN}{dx d\epsilon}$ over electron track and radiated photon energy $d\epsilon$. Two main factors determine the nonlinearity of the $L_{cher}(E, n)$. Non-linearity of the Cherenkov factor could be expressed as a derivative df/dE. From the point a) until the point b) the spectral range of Cherenkov spectrum is growing, increasing the contribution of the Cherenkov (df/dE increases). However, there is another even more important mechanism generating non-linearity: the dependency of the df/dE on the ionization stopping power dE/dx (Fig. 2.6). Actually,

$$df/dE \propto dN_{cher}/dE = \frac{dN_{cher}}{dx}\frac{dx}{dE} \qquad (2.14)$$

---

[7] Fortunately, it was found to be quite constant in the range 300-400 nm where the refractive index of organic liquids has the most complicated shape (Ref. [98]). It makes analytically calculated $L_{cher}(T, n)$ quite close to the one obtained from more detailed simulations.

therefore df/dE is not constant until dE/dx changes. Finally, Cherenkov response df/dN becomes linear when the stopping power dE/dx reaches a plateau at about $1.5MeV$.

Energy scale model

An analytical energy model could be constructed incorporating two non-linear effects: scintillation quenching and Cherenkov radiation. The total amount of light (collected charge) for an electron of a given energy can be obtained:

$$E_{vis}(T) = L(T, kB) + L_{cher}(T, n) \tag{2.15}$$

Note that relative contribution of these two terms are detector-dependent. To include this dependency in the model we scale the function $L_{cher}(T, n)$ with a factor f_{cher} to increase the relative contribution of Cherenkov light into the total light yield (energy estimator E_{vis}):

$$E_{vis}(T) = L(T, kB) + f_{cher} L_{cher}(T, n) \tag{2.16}$$

Varying f_{cher}, we can study the whole range of liquid scintillator detectors, which due to different scintillator compositions have different Cherenkov contributions. Here the role of the quenching effect is not considered explicitly and $L(T, kB)$ is kept fixed.

As a measure of the importance of the Cherenkov effect one can define a value of the relative contribution of Cherenkov light at 1 MeV:

$$\eta_{cher} = f_{cher}\, f(1\,\mathrm{MeV}, n)\, / L(1\,\mathrm{MeV}, kB) \tag{2.17}$$

In extreme case of a pure Cherenkov detector ($\eta_{cher} = 1$, $f_{cher} \to \infty$) the model simplifies to:

$$E_{vis} = L_{cher}(T, n) \tag{2.18}$$

A more detailed description of the energy model may be found in [91].

Table 2.1: Contributions in the relative variance of the energy resolution.

Notation	Origin of the term	Typical values for 1 MeV electron
v_{st}	statistical	~ 0.0064 (Daya Bay) [99] ~ 0.0025 (BOREXINO) [100] ~ 0.001 (JUNO expected) [9]
v_p	light collection	~ 0.0023 (CTF) [88]
v_{int}	intrinsic energy resolution	~ 0.01 [18]
v_d	dark noise	$\sim 3 \times 10^{-7}$ (BOREXINO) [91]

Energy resolution

In this section, we derive the expression for the energy resolution from the first principles where intrinsic energy resolution term naturally appears.

Energy resolution is represented by relative variance of collected charge (energy estimator):

$$\left(\frac{\sigma_E}{E}\right)^2 \approx \left(\frac{\sigma_Q}{Q}\right)^2 = v_{st} + v_p + v_{int} + v_d, \tag{2.19}$$

where v_{st} is the statistical relative variance, v_p is the light collection term, v_{int} is the intrinsic energy resolution term and v_d is the dark noise term. As an example, the typical values of terms for different experiments are presented in Table 2.1. Further, the definition of each term is provided and the expression (2.19) is derived. The second part of this chapter is dedicated to the experimental investigation of this relation.

The v_{st} term is a square of the statistical resolution term (2.1) that was discussed above:

$$v_{st} = \frac{1 + v_m}{N_{pe}}$$

As you may see there is an additional term v_m in the numerator which represents fluctuations of the gain. For modern PMTs:

$$v_m \approx 0.1 - 0.3$$

.

The term v_p is mainly related to light collection probability. Indeed, light collection probability in different points of the detector could be different. It generates an additional variation of the signal. MC simulations and calibrations of the detector may provide useful information about this term. In principle, if the position of an event in a detector is precisely known this term could be corrected.

The term v_{int}, called intrinsic energy resolution (IER), is associated with an intrinsic variation of light emitted by the liquid scintillator. A consistent theory of this phenomena for liquid scintillators was not developed yet. Measurement of v_{int} is one of the main aims of the laboratory experiment that will be discussed in this work. Since, in general, the experiment provides $\left(\frac{\sigma_Q}{Q}\right)^2$, other contributions should be reduced, estimated or also measured.

v_d - dark noise term. It rapidly falls with the increase of energy and could be measured. This term is presented only in large-scale experiments due to a large amount of PMTs. It is completely negligible when a small amount of PMTs is used.

On the derivation of the expression (2.19)

In order to understand better the structure of the expression (2.19) as well as the meaning of the intrinsic resolution term it is very useful to derive it from the first principles.

Resolution in case of the fixed number photons

Let us first consider a fully abstractive case: the source is emitting exact amount of the photons N_{phot} and define η, the probability for a photon to produce the photoelectron that reaches the first dynode. This value could be factorized in the probability for the photon to reach the photocathode, probability to produce a photoelectron and the effectiveness of electron collection on the first dynode. If the coefficient of the multiplication of the photoelectrons M is constant, the mean charge collected by PMT could be written as:

$$Q = N_{phot} \times \eta \times M \tag{2.20}$$

The process of the registration of the photons is Poissonian. In this case, the relative variance of the number of photoelectrons could be found as
$\sigma^2_{p.e.} = N_{phot}\eta(1-\eta)$.
The relation for the relative resolution in this case:

$$\frac{\sigma^2_Q}{Q^2} = \frac{N_{phot}\eta(1-\eta)M}{\eta^2 N^2_{phot} M} = \frac{1-\eta}{\eta N_{phot}} = \frac{1}{\eta N_{phot}} - \frac{1}{N_{phot}} = \frac{1}{N_{p.e}} - \frac{1}{N_{phot}} \tag{2.21}$$

Since it is a binomial process, η could also include the probabilities of the transmission of the light through the glass of the photomultiplier or some filters, reflections and so on: the formula will be the same.

Now let us consider that emitted photons follows Poissonian statistics with a variance $1/N_{phot}$. Summing up with the previous result we get:

$$\frac{\sigma^2_Q}{Q^2} = \frac{1}{N_{p.e.}} \tag{2.22}$$

Therefore the charge resolution has a form $\frac{1}{N_{p.e.}}$ in the case if the source has a Poissonian nature.

Variation of the light collection: v_p term

Since light collation is not isotropic and homogeneous in a vessel that contains scintillator, the probability for the photon to reach the photo-multiplier may depend on some other conditions, for example from the coordinate of the event. Thus, an average amount of the photons for the events with the same energy in the different points of the detector is different, and η is not a constant and depends on the coordinate: $\eta = \eta(x, y, z)$. For example, in large liquid scintillation detectors, the amount of photons that reaches the photo-multipliers depends on the position of the event inside of the detector: the events in the center and events on the periphery give on average different amount of the photoelectrons. On a small scale, an important role plays the reflective properties of the surrounding materials. It also induces the variation of the signal for the events that happened in different places of the cell. This fact should be taken into account by additional term v_p in the formula for the resolution. Note that variation of the light collection, in general, could be not Gaussian.

Intrinsic resolution: v_{int} *term*

In general case an amount of the emitted photons obeys the Gaussian distribution with relative variance $v(N_{phot}) = \frac{\sigma^2_{phot}}{N^2_{phot}}$. In this case the term $1/N_{phot}$ doesn't vanish. Instead we have:

$$\frac{\sigma_Q^2}{Q^2} = \frac{1}{N_{p.e}} - \frac{1}{N_{phot}} + v(N_{phot}) = \frac{1}{N_{p.e}} + v_{int}$$

where

$$v_{int} = v(N_{phot}) - \frac{1}{N_{phot}}$$

is so-called *intrinsic energy resolution*. In other words the intrinsic resolution is a measure of the deviation of the statistics of the photon emission from the Poissonian.

Statistical term and dynode system

The coefficient of the amplification M is a multiplication of the secondary particles produced at the *i*th-dynode at each stage δ_i.

$$M = \delta_1 \delta_2 ... \delta_n$$

Of course, this value δ_i fluctuates at each dynode. It leads to fluctuations of the amplification factor M. Let us estimate them.

For simplicity suppose that $\delta_i = \delta$ for any i. Also, suppose that the statistics of the electron emission is Poissonian.

Intuitively it is clear that the most important fluctuations are on the first dynode. The process of the amplification is a cascade process. We consider it step by step:

1. Photoelectron collides with the first dynode and produce on average $M_1 = \delta$ secondary electrons with the spread $\sigma_{M_1} = \pm\sqrt{\delta}$.

2. Each from the secondary electrons also produce $\delta \pm \sqrt{\delta}$ electrons. It gives $M_2 = \delta^2$ for the average. Applying the central limit theorem the spread could be determined as $\sqrt{N\delta}$, where N is the number of the incident electrons. Since on the previous step δ electrons were produced on average, $N = \delta$ and hence $\sigma_{M_2} = \delta^2$.

3. Repeating the same calculations we can find on the next step $M_3 \pm \delta_{M_3} = \delta^3 \pm \sqrt{\delta^3}$. Further by induction, the average amount of electrons and their spread on the *n*-th dynode is equal to $M_n \pm \delta_{M_n} = \delta^n \pm \sqrt{\delta^n}$.

Relative variance $(\frac{\sigma_{M_i}}{M_i})^2$ on each step will be equal to $1/\delta^n$.

So, the relative variance of the coefficient of the amplification is equal to

$$(\frac{\sigma_M}{M})^2 = (\frac{\sigma_{M_1}}{M_1})^2 + ... + (\frac{\sigma_{M_n}}{M_n})^2 = 1/\delta + 1/\delta^2 + 1/\delta^3 + ... + 1/\delta^n$$

If the amount of the dynodes is big and $\delta >> 1$ this series could be approximated as a sum of the geometric progression (Ref. [101]):

$$v_m = (\frac{\sigma_M}{M})^2 = 1/\delta + ... + 1/\delta^n = 1/\delta(1/\delta + ... + 1/\delta^{n-1} \approx \frac{1}{\delta}(\frac{1}{1-1/\delta}) = \frac{1}{\delta}(\frac{\delta}{\delta-1})$$

In general case, δ_i on each stage could be different. Usually, only the δ_1 of the first dynode is different. It is to show that in this case the relative variance equal to $v_m = \frac{1}{\delta_1}(\frac{\delta}{\delta-1})$. Analyzing this expression one may see the fundamental role of the first dynode amplification factor δ_1: an increase of this factor leads to the reduction of the v_m, therefore improvement of the resolution of PMT. For modern PMT the value of v_m is about 0.1-0.3.

In principle, the value v_m could be measured. The laser system discussed above could be adapted to do this. For pulses of the different amplitudes, the mean value of the charge Q as well as ΔQ could be determined. Using the calibration of the PMT charge Q in the number of photoelectrons we then could extract the factor $(1+v_m)$ from the measurements using the formula:
$\frac{\Delta Q}{Q} = \frac{1+v_m}{N_{p.e.}}$

In above calculations of $(\frac{\sigma_Q}{Q})^2$ we supposed $M = const$. In this case the relative variation of the collected charge is equal to the relative variation of the number of photoelectrons $(\frac{\sigma_{N_{p.e.}}}{N_{p.e}})^2 = (\frac{\sigma_Q}{Q})^2$.

In reality M for each photoelectron is different and each has its own cascade process. Let us assume $N_{p.e.}$ were produced on the photo-cathode. Then each photoelectron will be multiplied and give on average give M electrons with some variation. Applying the central limit theorem the general amount of the amplified photoelectrons will be equal to $N_{multi} = N_{p.e.}M$ and their standard deviation $\sigma_{multi} = \sqrt{N_{p.e.}\sigma_M}$. That is $N_{p.e.}M \pm \sqrt{N_{p.e.}\sigma_M}$.

$$(\frac{\sigma_{N_{multi}}}{N_{multi}})^2 = (\frac{\sqrt{N_{p.e.}}\sigma_M}{N_{p.e.}M})^2 = \frac{v_m}{N_{p.e.}}$$

Finally, the relation for the relative variance of the collected charge:

$$(\frac{\sigma_Q^2}{Q^2})^2 = (\frac{\sigma_{N_{p.e.}}}{N_{p.e.}^2})^2 + (\frac{\sigma_{N_{multi}}}{N_{multi}})^2 + v_p = \frac{1}{N_{p.e.}} + v_p + v_{int} + \frac{v_m}{N_{p.e.}} = \frac{1+v_m}{N_{p.e.}} + v_p + v_{int}$$

Dark noise term v_d

To add the term v_d associated with dark noise we note that the total number of collected electrons from the photocathode $N^{\Delta t}_{collected}$ in the time interval Δt consists of two parts: photoelectrons ($N^{\Delta t}_{p.e}$) and dark count electrons ($N^{\Delta t}_{dark} \pm \sqrt{N^{\Delta t}_{dark}}$) due to thermal emission from the surface.

$$N^{\Delta t}_{collected} = N^{\Delta t}_{p.e.} + N^{\Delta t}_{dark}$$

with the standard deviation:

$$\sigma^2_{collected} = \sigma^2_{p.e.} + \sigma^2_{dark} = N^{\Delta t}_{p.e.} + N^{\Delta t}_{dark}$$

Since the mean value of dark current is known $< N_{dark} >$, number of photoelectrons could be found as:

$$N_{p.e.}^{\Delta t} = N_{collected}^{\Delta t} - < N_{dark}^{\Delta t} >$$

The standard deviation of the collected signal is consist of two parts as well:

$$\sigma_{p.e.}^{2} = \sigma_{collected}^{2} = N_{p.e.}^{\Delta t} + N_{dark}^{\Delta t}$$

So to take into account one need to add the term $v_{dark} = N_{dark}^{\Delta t}/(N_{p.e.}^{\Delta t})^2$

Experimental determination of non-linearity and intrinsic energy resolution

The linearity of the energy scale and energy resolution are highly relevant to the performance of large-scale liquid scintillator detectors. In the last 20 years, the technologies associated with the construction of the large-scale liquid scintillator detectors made a big step forward opening a new frontier on the field of particle physics, in particular in neutrino physics. New, challenging scientific programs encourage researchers to study the detector energy scale and energy resolution in detail and deeply examine phenomena which are at the base of particle detection.

The main characteristics of any scintillator are energy resolution and linearity of the energy scale. Accurate spectroscopy and data analysis should take these characteristics into account. The knowledge of them gives a possibility for accurate Monte Carlo simulations. The detector response depends on these characteristics as well. For the JUNO detector response has stringent requirements: uncertainty on non-linearity $< 1\%$ and energy resolution 3% for 1 MeV.

The primary goal of the experiment described in this chapter is the non-linear response and intrinsic energy resolution measurements. These parameters are determined by analytical procedure, detector calibrations and Monte Carlo simulations (Ref.[91]). However, a more detailed separate investigation is needed for better understanding of the detector response.

The first measurements of non-linearity of liquid scintillator were performed many years before the large liquid scintillator detectors started operation. In '60s the non-linear response of electrons were already under discussion (Ref. [102]). Experimental data on non-linearity and intrinsic energy resolution for liquid organic scintillators are poor. One can easily find several attempts for measuring non-linear response of liquid scintillator (Ref. [103], [94], [104], [105]).

Recently the measurements of Linear AlkylBenzene (LAB) scintillator non-linear response for Daya Bay collaboration by classic Compton coincidence technique was performed in Ref. [103]. This method has several limitations. First of all, it requires a powerful radioactive source (0.1 mCi). To increase event rate, seven crystals were used simultaneously. The measurement was performed for energies up to 1 MeV, but as it was discussed in Sec. 2.4 all valuable information about quenching non-linearity is in the range below 100 keV.

In Ref. [18] a new technique with HPGe detector was presented, and both non-linearity and intrinsic energy resolution were measured. It was the only attempt to measure intrinsic energy resolution of liquid scintillator. However, the result of this measurement could be criticized. The detailed study of light collection term v_p was not provided. At higher energies, the contribution into non-linearity and energy resolution due to Cherenkov effect was also not studied. The results could be treated in the way that they are valid only for the particular setup that was used and they could not be applied to another laboratory setup or a large scale liquid scintillation detector. Another group of authors also introduced the same technique for LAB non-linear response measurements (Ref. [105]). Two fundamental problems were indicated: multiple Compton scattering (mostly double scattering) in the LS-detector and the non-uniformity of light collection within the liquid scintillator volume were discussed. However, the quantitative analysis of these effects was not performed.

Despite the lack of direct measurements, there are some indications on the presence of intrinsic resolution. The analytical model function that describes the response of the Borexino detector consists of 13 parameters; among them, there is a term that is respon-

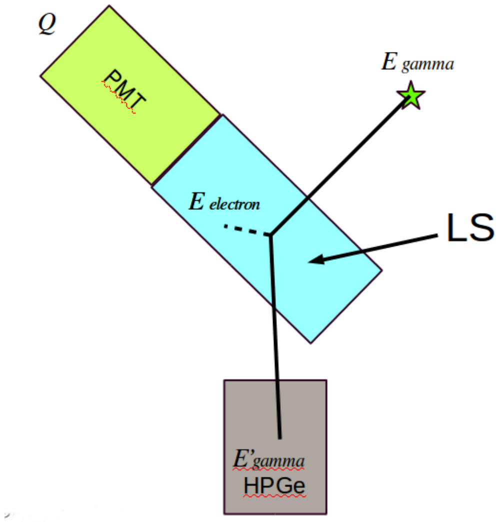

Figure 2.9: Sketch of experimental setup for liquid scintillator (LS) response study.

sible for the presence of intrinsic energy resolution at low energies. After the fitting procedure, the term was found to be different from zero (Ref. [100]).

For both energy non-linearity and energy resolution measurements, Compton coincidence technique with High Purity Germanium (HPGe) detector gives promising results. However, to overcome limitations related to double Compton scattering and variation of the light collection, standard methods of nuclear spectroscopy should be complemented by detailed spectral analysis and intensive Monte Carlo studies.

The concept design of the setup is shown in Fig. 2.9. It consists of a quartz cell covered with reflective material coupled with a photomultiplier, radioactive monochromatic gamma source and HPGe detector. To protect PMT from the light the system was placed in a dark box.

Superb energy resolution of the HPGe detector provides a possibility to reconstruct the energy of Compton electron directly from the difference between initial energy E_γ and energy deposed in HPGe detector E_{HPGe}:

$$E_e = E_\gamma - E_\gamma^{'} \tag{2.23}$$

With this method, the energy of scattered electron could be reconstructed regardless of the scattering angle. Acquiring the coincidence events in HPGe detector and PMT one can measure energy response of the liquid scintillator to low energy electrons.

It is a significant advantage compared with Compton coincidence experiment where the energy of the electron is reconstructed using scattering angle. The formula that links the energy of the incident gamma with scattered one is:

$$E_\gamma' = \frac{E_\gamma}{1 + \frac{E_\gamma}{m_e}(1 - \cos\theta)} \tag{2.24}$$

The energy of the Compton electron could be represented as:

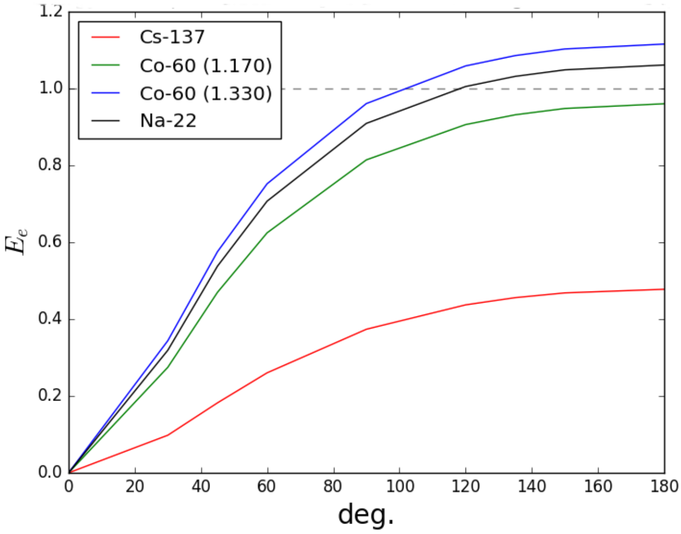

Figure 2.10: Electron energy E_e as a function of the angle of the scattered gamma. ^{137}Cs (661.657 keV) , ^{60}Co (1173.228 keV, 1332.492 keV), ^{22}Na (1274.537 keV).

$$E_e = E_\gamma - E'_\gamma = \frac{\frac{E_\gamma^2}{m_e}(1-\cos\theta)}{1+\frac{E_\gamma}{m_e}(1-\cos\theta)} \tag{2.25}$$

The maximum energy that could be transferred to the electron is called E_{edge}. It corresponds to the energy of the electron E_e for the value $\cos\theta = -1$, when gamma quanta are scattered in the opposite direction to the incident gamma.

$$E_{edge} = \frac{\frac{2E_\gamma^2}{m_e}}{1+\frac{2E_\gamma}{m_e}} \tag{2.26}$$

For the energy of the gamma of 661.66 keV (^{137}Cs) one has:

$$E_{edge} = \frac{2E_\gamma^2}{m_e + 2E_\gamma} = \frac{2\times 0.662^2}{0.511 + 2\times 0.662} = 477.4\,keV \tag{2.27}$$

Formula (2.25)s could be used for electron energy reconstruction only if the scattering angle is well determined. In Fig. 2.10 the dependence of the electron energy E_e from the angle θ of the scattered gamma is shown. Usually, this could be achieved by collimating incident and scattered gammas. Once the angles are fixed, the energy of the electron is within a small energy range that could be found from kinematics. However, collimation reduces dramatically in and out gamma fluxes. To collect enough statistics, one needs a longer time of exposition and more powerful gamma source. The longer time of explosion makes measurement less reliable due to setup instability. On the other hand, the absence of collimators provides a possibility to observe many incidental particles with different angles at the same time and perform measurements at shorter times and using

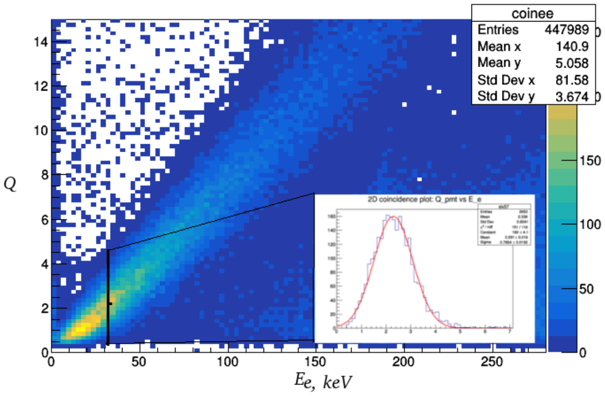

Figure 2.11: Coincidence 2d histogram. x-axis is a reconstructed energy of electron E_e. y-axis is charge collected by PMT. An example of the fitted slice is also shown.

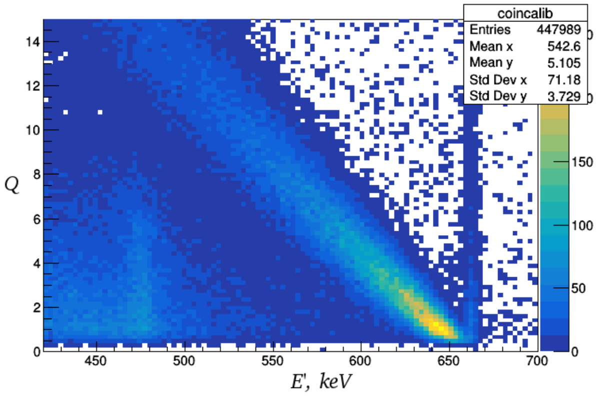

Figure 2.12: Coincidence 2d histogram. x-axis is the energy of scattered gamma deposed in HPGe. y-axis is charge collected by PMT.

weaker sources. In this case, set up is more compact and could be operated with sources of activity less than 10 μ Ci (370 kBq).

The coincidence 2d-histogram is shown in Fig. 2.12. The diagonal structure includes all information about non-linear response and energy resolution of the scintillator.

Applying relation (2.23) one can invert histogram 2.12 and get the histogram 2.11 in terms of E_e and Q. The coincidence matrix can be cut on small slices with a certain energy of electron E_e detected by HPGe. Each slice-histogram can be analyzed and fitted. The mean value $Q(E_e)$ of the peak gives us information about non-linearity. In order to extract the information about non-linearity and determine Birks' ionization quenching constant kB, one needs to fit with previously discussed function $L(T, kB)$.

The standard deviation σ_Q or more accurately relative variance $v_Q = \frac{\sigma_Q^2}{Q^2}$ gives an information about total energy resolution. In order to measure intrinsic energy resolution contribution other terms should be separated:

$$v_{int} = v_Q - v_p - v_d$$

HPGe detector

The big success of purification was achieved for germanium detectors. The appearance of the ultra-pure germanium crystals revolutionized the gamma spectroscopy. To achieve the higher active volume at the fixed depletion depth the close-ended coaxial geometry is used. Also it has an advantage in sensitivity due to smaller capacitance which is given by relation $C = \frac{2\pi\epsilon}{ln(r_2/r_1)}$. To achieve better efficiency and energy resolution one should increase the depletion depth by moderating the voltage applied to the crystal.

For the experimental setup High Purity Germanium (HPGe) detector *Gem30P* by ORTEC was used. The optimal voltage recommended by producer was 4000 V. The front corners as well as the hole of the germanium crystal are rounded to eliminate possible low-field regions. The volume of the crystal is $146.0\,\mathrm{cm}^3$ ($R = 32.35\,\mathrm{mm}$ and $l = 45\,\mathrm{mm}$; axial hole $R_h = 4.45\,\mathrm{mm}$ and $l_h = 31.1\,\mathrm{mm}$). Close-cycle refrigerator is used for cooling. It is equipped with a thermistor for interlocking. The preamplifier is a part of the cryostat package and it is placed as close to HPGe as possible to reduce induced capacitance.

The charge collection in HPGe is inherently slow: it takes about 100 ns for charge carriers to travel 1 cm. It implies the principal limit on a front edge of a signal. As compared to a rising time of PMT signal $\sim$ 5 ns it is a larger value, so HPGe pulse shape dictates the coincidence time spread. The detailed shape of the pulse depends on the place in the detector where an event occurs. Applying higher voltage may increase the speed of charge carriers until it saturates (at $77K$ it is 10^5 m/s for both electrons and holes, that could be achieved at $10^5\,\mathrm{V/cm}$ and $3 \times 10^5\,\mathrm{V/m}$, respectively). Unlike the case of electrons and ions in ion-chambers, the speeds for electrons and holes are of the same order, but the difference in speed implies the difference in the pulse shape and collecting process: for event that happens near the negative electrode the full collection time will be shorter, since holes will be collected first. The presence of trapping and release of carriers may further complicate the pulse shape introducing the slow component (due to release) and the additional contribution into energy resolution (due to not complete charge collection).

Germanium has a small atomic number compared to the NaI, so its photo-effect cross section is one order of magnitude smaller, making the detector more transparent for gamma rays. Consequently, the effects of escaping gammas and X-rays become more relevant. The spectrum of the acquired background is shown in Fig. 2.14. The shape of the full absorption peak significantly deviates from the Gaussian. It has a tail at lower energies as illustrated in Fig.2.13. To characterize this effect the Full Width at 10 % of the Maximum $FW0.1M$ is usually specified (for Gaussian distribution $FW0.1M = 1.823 \times FWHM$).

As it was told the energy of the Compton electron is reconstructed from $< E_e >= E_\gamma - < E'_\gamma >$. To link the energy pulses and deposed gamma energy in HPGe the detector should be properly calibrated. The information about calibration (linearity of the scale and energy resolution) then is used in the analysis and Monte Carlo simulations to model the detector response.

HPGe preamplifier has two outputs. One was connected via an amplifier to the data acquisition module (DAQ). Another passed by a discriminator to form a trigger pulse for coincidence.

It was found that HPGe detector had excellent linearity, superb resolution and showed good stability on a long timescale. All these three properties make HPGe detector unique for liquid scintillator investigation.

Indeed, energy resolution plays an important role for the coincidence measurements. The energy of the Compton electron could be reconstructed from the initial energy of the

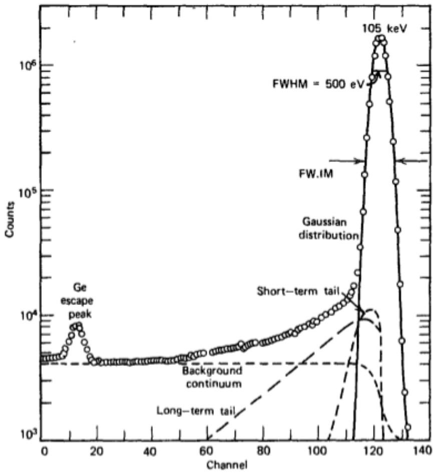

Figure 2.13: The detailed structure of the full absorption peak (from Ref. [14])

gamma E_γ and energy deposed in HPGe E_{HPGe}:

$$E_e = E_\gamma - E_{HPGe} \tag{2.28}$$

The error of determination of electron energy E_e in this case is directly connected with an absolute error of E_{HPGe}:

$$\sigma_{Ee} = \sigma_{Ehpge} \tag{2.29}$$

It means that the better energy range is located in the region, where the *absolute* energy resolution σ_{Ehpge} is better. Absolute energy resolution σ_{Ehpge} of HPGe degrades with energy (as $\sim \sqrt{E}$), even though the *relative* energy resolution became higher (as $\sim 1/\sqrt{E}$). From this we derive an important, but somehow counterintuitive conclusion: the energy region that has a better *absolute* energy resolution σ_{Ehpge} is preferable.

This is a good argument in favor of ^{137}Cs ($E_\gamma = 661.7$ keV; $T_{1/2} = 30.07$ years).

Despite this fact ^{22}Na ($E_\gamma = 1274.6$ keV and 511 keV annihilation, $T_{1/2} = 2.6$ years) source was used in Ref. [18] and ^{60}Co ($E_\gamma^{1,2} = 1173.237, 1332.501$ keV, $T_{1/2} = 5.27$ years) and ^{207}Bi ($E_\gamma^{1,2\,main} = 569.70, 1063.66$ keV; $T_{1/2} = 31.55$ years) in Ref. [105]. We preferred not to use these sources. ^{137}Cs also has an advantage of being a source with a single gamma. Sources with two and more gamma emission (^{207}Bi , ^{60}Co and ^{22}Na) give more complicated 2-d coincidence histogram.

Since the energy range, 0-662 keV was chosen an amplification of the signal was adjusted to match DAQ acquisition range (signal from 700 keV gamma corresponds to the maximum of the acquisition range). The list of calibration sources for this range is provided in Table 2.2. Usage of 511 keV annihilation gamma for calibrations is not recommended since it is asymmetric, broader and shifted (due to positronium bounding energy) (Ref. [14]).

In precise gamma spectroscopy, the method of least squares is common for fitting calibration data with a polynomial function of order 4-5 (Ref. [14]). Since in our case the energy range of HPGe is smaller (500 - 662 keV) we can approximate a small part of the calibration curve by a linear function (Fig.2.15).

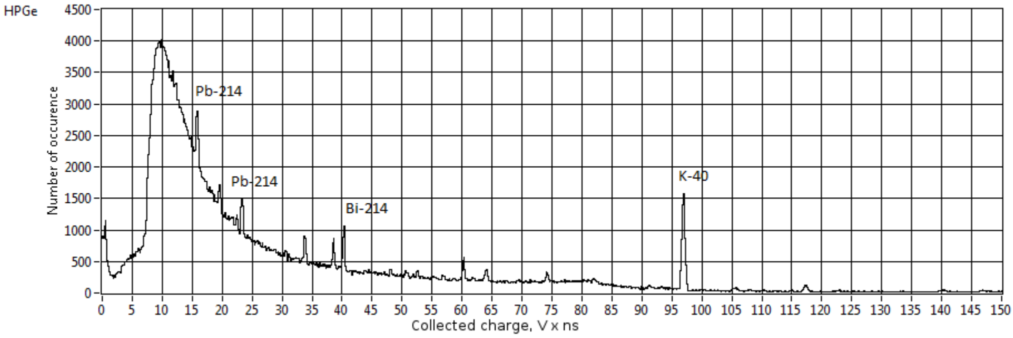

Figure 2.14: Longtime background measurement of HPGe. ^{40}K, ^{214}Bi, ^{214}Pb peaks are clearly observed.

Table 2.2: List of calibration gamma lines and sources in the energy range of interest 0-662 keV.

Energy, keV	Source	Source's code
121.78	^{152}Eu	35 B
244.69	^{152}Eu	35 B
276.40	^{133}Ba	42 B
302.85	^{133}Ba	42 B
344.28	^{152}Eu	35 B
356.01	^{133}Ba	42 B
383.85	^{133}Ba	42 B
411.12	^{152}Eu	35 B
443.97	^{152}Eu	35 B
569.70	^{207}Bi	59 B
661.66	^{137}Cs	37 B

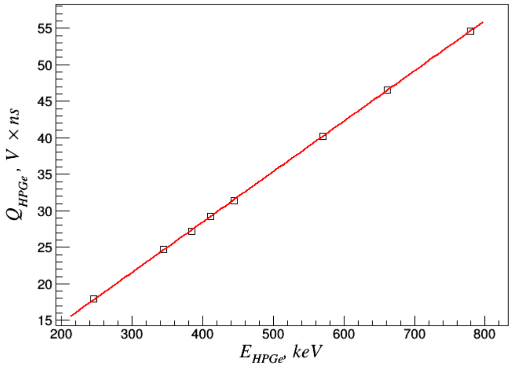

Figure 2.15: Calibration curve. X-axis is the energy E_{hpge} of gamma line in keV. Y-axis is a charge Q_{hpge} in V × ns, integrated by DAQ system. Calibration peaks: ^{152}Eu (244.6974 keV), ^{152}Eu (344.2785 keV), ^{133}Ba (383.8485 keV), ^{152}Eu (411.1165, 443.965 keV), ^{207}Bi (569.698 keV), ^{137}Cs (662 keV), ^{152}Eu (778.9045 keV)

Finally, one obtains the calibration relation for the conversion of the collected charge into the energy in the energy range 300-662 keV. This relation will be used in the analysis and Monte Carlo simulations.

Now let us have a look at the energy resolution of the HPGe detector. Three dominant factors contribute into energy resolution (Ref. [14],[106]):

- Inherent statistical spread in the number of charge carriers W_D
- Variation in the charge collection efficiency W_X
- Electronic noise W_E

So the total energy resolution:

$$W_T^2 = W_D^2 + W_X^2 + W_E^2 \tag{2.30}$$

The first term is:

$$W_D = \sqrt{F\epsilon E} \tag{2.31}$$

where F is Fano factor, ϵ - energy needed to create one electron-hole pair, and E is the gamma-ray energy. Assuming Fano factor $F = 0.1$ (Ref. [107]) and $\epsilon = 2.96$ eV gives $\sigma = 0.44$ keV resolution for 661.7 keV.

The second term W_X appears to incomplete charge collection. This effect is significant for large detectors and low average electric fields. Its magnitude could be experimentally measured by applying different high voltage. Shaping time of the amplifier also should be adjusted. Recommended shaping time for the Gem30P detector is $6\mu s$.

The third factor, W_E represents the broadening effects of the electronics components used. It could be tested with a pulse generator connected to the preamplifier. The typical relative importance of the contributions is illustrated in Fig. 2.16. In our case, since we use 10-bit module digitizer, the biggest contribution into the W_E is expected from the digitalization of the signal. To optimize this term, we set the maximum vertical range of the HPGe channel to energy 700 keV. For ^{137}Cs the resolution about $\sigma = 0.7$ keV could

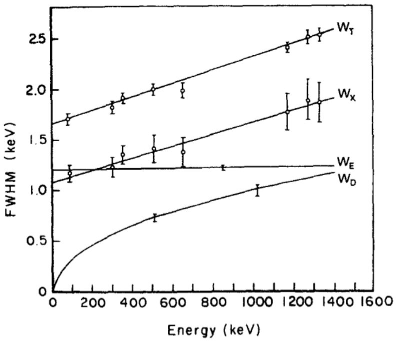

Figure 2.16: The plot illustrates different contributions of the resolution factors into the total energy resolution of HPGe (from Ref. [14])

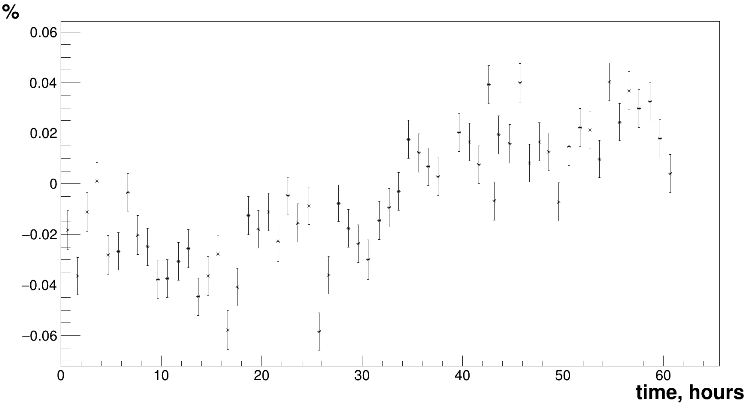

Figure 2.17: Full absorption peak deviation with time was ensured to be less than 0.1% from the mean value in the long time scale (measurement with ^{22}Na source).

be expected according to the specification. Energy resolution for ^{137}Cs peak was found to be $\sigma = 1.5$ keV. Further improvement could be achieved with a DAQ module with higher resolution (> 10 bits).

HPGe stability was checked by observation of the deviation of the full absorption peak from its mean value over the full period (Fig. 2.17). It was found to be less than 0.1% (< 0.6 keV). Short term instability of HPGe can also spoil energy resolution, while long-term drift can modify energy scale. It was decided to perform short calibration runs during the coincidence data acquisition to control the stability of HPGe detector with ^{137}Cs and ^{207}Bi calibration sources.

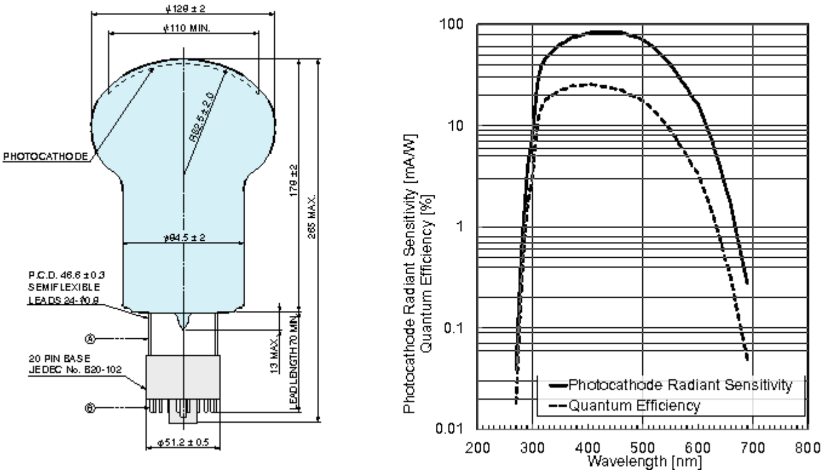

Figure 2.18: Schematic (left) and radiant sensitivity and quantum efficiency $QE(\lambda)$ of R6594 (right) from Ref. [15]

Photomultiplier and liquid scintillator

The schematic and quantum efficiency curve are presented in Fig. 2.18. Quantum efficiency $QE(\lambda)$ has a maximum at about 400 nm. Spherical PMT shape was not an optimal solution to couple with cylindrical quartz cuvette (35 type; $r \times l = 25 \times 100$ mm), but it was a price to be paid for other characteristics since flat window PMT with similar characteristics was not available. Flat window tube should be purchased for further studies.

The number of photo-electrons collected by PMT is proportional to

- Scintillator light-yield LY [photons/MeV] and its emission spectra $E(\lambda)$, $\int_0^\infty(\lambda)d\lambda = 1$.
- Reflection coefficient of cell's walls R_{wall}
- Optical coverage G_{cov}
- Quantum efficiency of a PMT $QE(\lambda)$
- Collection efficiency of the first dynode C_d

$$N_{p.e.} \propto LY \cdot R_{wall} \cdot G_{cov} \cdot C_d \int d\lambda \cdot QE(\lambda)E(\lambda) \tag{2.32}$$

Maximum of the number of photoelectrons could be achieved if the maximum of emission spectrum $E(\lambda_{max})$ is close to the quantum efficiency maximum $QE(\lambda_{max})$. A liquid scintillator for JUNO consists of three components: linear alkylbenzene (LAB) with emission spectra in the range between 300 and 400 nm, 2,5-diphenyloxazole (PPO) 300-480 nm and 1,4-Bis(2-methylstyryl)benzene (bis-MSB) 372-540 nm. The emission spectrum of PPO is shown in Fig. 2.19 from Ref. [16]. The maximum of the spectrum is in the range 350-400 nm which is close to the maximum of quantum efficiency of R6594 PMT. In this study, it was decided to use no bis-MSB. transparency of liquid scintillator at a large scale.

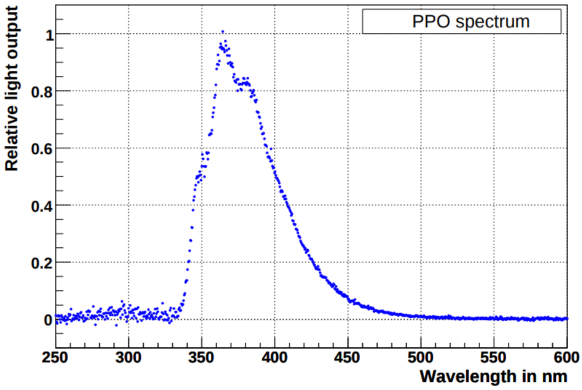

Figure 2.19: Emission spectrum from PPO dissolved with a concentration of 2 g/l in PXE (from [16]).

One needs to collect as many photoelectrons as possible to obtain the lowest possible threshold. To do this one needs to cover a cell by materials with high reflectivity and glass with good transparency for the entire emission spectrum of LS. Currently, we use aluminized Mylar for quartz cell coverage.

Now let us discuss closely the characteristics, which are essential for the measurement and formulate the optimal parameter range.

Response of the PMT

In order to understand the response of the PMT the techniques for singe photoelectron counting should be applied. Another motivation for the study of the s.p.e. response is the determination of the average charge produced by single photo-electron m_s and its variance v_m as important parameter for PMT scale calibration and intrinsic resolution studies. In this chapter, we are closely following the methods of the precise photon-electron counting developed in Ref. [108].

The main parameters of single electron response (SER) is the mean value m_s and relative variance $v_m = (\sigma_s/m_s)^2$.

An ideal SER consists of an exponential and Gaussian part:

$$SER_0(x) = \begin{cases} \frac{P_E}{A} e^{-\frac{x-x_p}{A}} + \frac{1}{\sqrt{2\pi}\sigma_0} \frac{1-P_E}{g_N} e^{-1/2 \frac{(x-x_0-x_p)^2}{\sigma_0}}, & \text{if } x > 0 \\ 0, & \text{if } x \leq 0 \end{cases} \tag{2.33}$$

where A is a slope of the exponential part, p_E is the number of events under the exponential function, x_p position of the pedestal and x_0 and σ_0 - mean value and standard deviation of the Gaussian part. $g_N = \frac{1}{2}\left(1 + \mathrm{Erf}(\frac{x_0}{\sqrt{2}\sigma_0})\right)$ is a factor to account for the cut of the PMT response Gaussian part. In principle, to improve correspondence of the ideal SER to the experimentally observed response it should be convoluted with a noise function that affect only exponential part as described in Ref. [108].

For $n > 1$ p.e. the response could be fitted with the function

$$M(x) = \sum_{n=2}^{N_M} \frac{P(n,\mu)}{\sqrt{2n\pi}\sigma_1} e^{-(1/2n)(\frac{x-nx_1-x_p}{\sigma_1})^2}, \tag{2.34}$$

that takes into account Poisson distribution of the detected light and Gaussian approximation for the responses to n photoelectrons.

For high voltage of 1600 V applied the integrated charge of single photoelectron is about $Q_s = 0.2$ V $\times$ ns (Fig. 2.29) and the amplitude is about $A_s = 33.8$ mV.

Dark noise measurement

For dark rate measurement the high voltage for R6594 PMT was set to 2000 V. At this value, the average amplitude of the dark noise pulse was about 150 mV. The threshold of the discriminator was about 30 mV ($\sim$ 0.2p.e.). The voltage was set up at such a high value to be sure that the significant part of the Gaussian part of the dark pulse amplitude's distribution is above the threshold of the discriminator. Just after the light exposure, the measured dark rate was about 18 kilo counts per second (kcps). After 30 minutes of warming up, it reduced to 2.8 kcps.

Charge-amplitude correlation of the signal

The correlation for integrated charge Q_{pmt}, V $\times$ ns (integral over the scintillation pulse) and amplitude A_{pmt}, V (maximum of the pulse) looks different for the signal from liquid scintillator and picosecond laser. The data acquired with liquid scintillator and laser (Fig. 2.20) showed $V/Q \approx 0.06\,\text{ns}^{-1}$ for liquid scintillator and $V/Q \approx 0.11\,\text{ns}^{-1}$ for the laser. The reduction of the amplitude is 54 % which is consistent with the internal measurement. In the case of the laser triggering, the amplitude-charge correlation is close to the one obtained for single photoelectron signal, since all photons arrive at the photocathode at the same time. For liquid scintillator, we deal with exponentially decreasing photon emission that is usually described by a superposition of several exponential probability distributions. In this case, photons arrive at the photocathode not at the same time, and the ratio between the amplitude and charge became much smaller. For LAB two main components of the probability distribution are 5 ns (fast) and 18 ns (slow) with 78 % and 17 % contribution, correspondingly [8](Ref. [16]). Therefore the amplitude should be reduced by 80 %.

One internal measurement conducted in Milan showed the values 4.5 and 18.95 ns with 56 % and 23 %.

PMT linearity

PMT should have an excellent dynamic range, that is to exhibit good linearity of anode output in a wide range of incident light intensities. The main factor that leads to saturation is the space charge effect at the last stages of amplification due to large flowing current [109]. In principle, the dynamic range of PMT could be increased with a specially designed voltage-divider circuit.

The value for linearity provided by Hamamatsu is $linearity(2\%) = 30$mA or 1500mV with 50 Ω termination.

The nominal photo-electron light yield to achieve is 1300 p.e./MeV that could be achieved with quite realistic $QE = 30\%$ and light collection $LC = 50\%$. The energy range of the interest is up to 100 keV, thus the maximal number of photoelectrons in the measurement is $N_{p.e.}^{max} = 130$ p.e.. To find the amplitude of the scintillation signal one needs to multiply this value by single photo-electron amplitude A_s and factor that takes into

---

[8] It should be noted that a ^{54}Mn (834 keV) gamma source was used for the measurements with 639 keV Compton edge. At such energy Cherenkov photons also contribute into the fast component of the signal affecting the result of the measurement

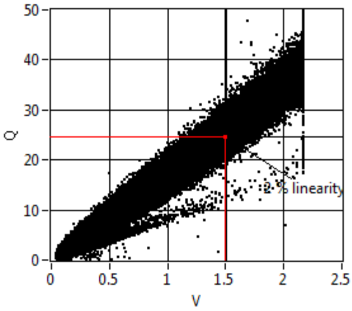

Figure 2.20: Charge - amplitude diagram for the signal from liquid scintillator. Two distinct correlation lines are clearly visible. The smallest line is generated by laser and has the charge-amplitude dependency of the s.p.e., the biggest one is the signal from the liquid scintillator.

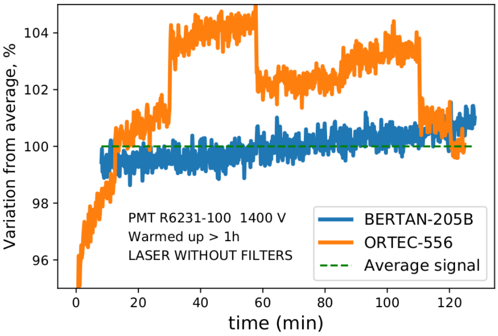

Figure 2.21: The comparison of the stability for two different HV power supply modules (*PMT R6231-100 was used*)

account charge-to-amplitude conversion $F_{Q\to V}$ which is approximately 0.5 for liquid scintillator. For 1600 V we get: $N^{max}_{p.e.} \times A_s \times F_{Q\to V} \approx 130\,\text{p.e.} \times 33.8\,\text{mV} \times 0.5 \approx 2180\,\text{mV}$. Thus, at 100 keV PMT is already in non-linear regime. For the present experimental setup the value 450 p.e./MeV was achieved. It corresponds to 756 mV at 100 keV. Therefore in the energy range of interest the PMT is always in linear regime.

PMT gain stability

A huge non-stability of the signal from PMT was found (about 5 % on the 10 hours timescale) from the first coincidence measurements. It is believed that LS is stable under laboratory conditions. The main sources of non-stability could be PMT by itself, electronics and HV-power supply. The study of the stability was conducted by using PMT in a dark box with a laser system with two different HV power suppliers: ORTEC and BERTRAN. The BERTRAN power supply demonstrated much better stability than ORTEC (Fig. 2.21).

Another approach is to use the gain correction technique if the independent measurement of the gain is available. It could be a measurement with low energy gamma source or the information from full energy absorption peak (in case of the source with two gammas) or with use of LED or laser for gain real-time calibration.

It was decided to use the laser. However, the question about laser stability and repeatability remained open. To reduce the uncertainty related to the laser stability is was proposed to use single photo-electron measurements instead to control gain evolution.

Monte Carlo simulation

The energy deposition scenario of gamma quanta is very different in large LS detectors and small experimental setup. In fact, in large detector gamma usually is fully absorbed in the scintillator. On the contrary, in small setup gamma always releases only some part of the energy, having one or several Compton scatterings and then escaping from the scintillator.

In the experimental setup that was discussed in the previous section scattered gamma then could be absorbed by HPGe detector. In this case, PMT and HPGe give a coincidence. The events in liquid scintillator with the only one Compton scattering occurred during gamma propagation are of our interest: they contain information about the response of liquid scintillator to a single Compton electron. On the contrary, the events with multiple Compton events may spoil the result. They produce less light for a given energy than single Compton events since quenching should be applied for each Compton electron. It leads to a systematic shift of the central value for the PMT response.

One may avoid the problem with multiple Compton events and, probably, even use them as an additional source of information for simulations tuning, if Monte Carlo can precisely reproduce the distortions observed in the coincidence diagram.

Another possible source of the systematic error is an interaction of the scattered electrons with the walls of the cell. It was found negligible (the typical range for 100 keV electrons is less than 0.2 mm). Also, an interaction of the photons with an environment and parts of the setup can induce some systematic effects. Monte Carlo simulations with detector geometry in GEANT4 can fully predict this kind of features of the data. Several other key questions could also be analyzed with Monte Carlo:

- What is the nature of the structures on the coincidence diagram? How they affect the measurements?
- What is the contribution of the systematic error due to multiple Compton events for different configurations of setup?
- Which experimental strategy is better for measurements?

First, let us analyze the Compton spectrum in the liquid scintillator without taking into account coincidence with HPGe detector. Modeled spectrum in the liquid scintillator is shown in Fig.2.23. The contribution from the multiple Compton events is quite

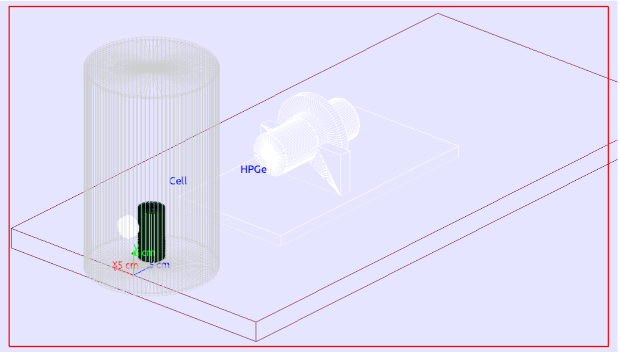

Figure 2.22: Experimental setup geometry simulation. On the picture: light tight cylinder with liquid scintillator cell and source inside, table and HPGe detector with support.

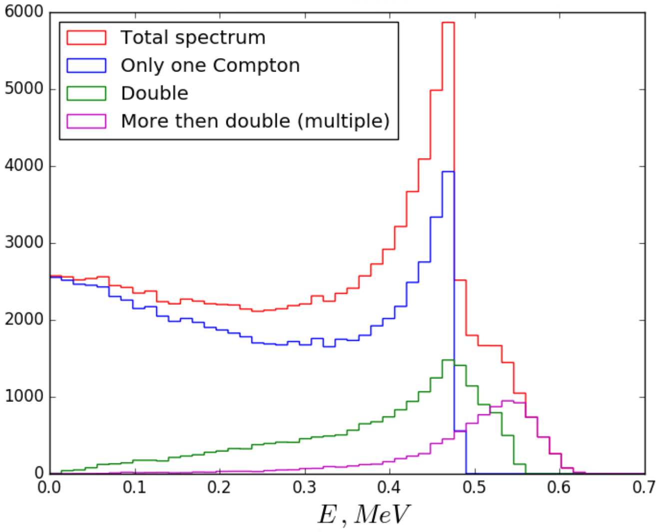

Figure 2.23: GEANT4 simulated Compton spectrum for ^{137}Cs gamma in the cell with liquid scintillator. Single and multiple Compton components are shown. No energy resolution applied).

significant: the ratio $N^{multiple}_{enents}/N^{1Compton}_{enents} = 0.4$. It is difficult to say so far how it affects our measurement since when the coincidence applied, some events became forbidden by kinematics.

Compton spectrum for HPGe could also be simulated. The comparison between the simulated spectrum and real data is presented in Fig. 2.24. The simulation satisfactory reproduce all spectral features. Significant deviations could be explained by quite complicate detector response function discussed previously (Fig. 2.13). Also, all effects related to X-ray emission are not reproduced by simulations. For our current purposes, the Gaussian shape of the full absorption peak could be assumed.

The full absorption peak is of high importance since in coincidence measurements the energy of electron E_e could be reconstructed correctly if and only if the energy of scattered gamma is fully deposed in HPGe detector.

Scatter coincidence plot

2d scatter plot of the coincidence events (energy deposed in HPGe *vs* energy deposed in LAB) is shown in Fig. 2.25. The origin of the peak in the field $E_{hpge} = 488$ keV and $E_{LS} = 50$ keV was determined when the code was modified in order to see in which detector the event occurs first (Fig. 2.26). It is clear that the peak corresponds to the situation when gamma has a backscattering in the HPGe detector first and then scattering in the liquid scintillator.

One should remember that on the diagonal where events of interest are located there are both single and multiple Compton scattering events (Fig.2.27). So far they are all on the diagonal because the quenching effect is not yet applied (Fig.2.27).

Since in Monte Carlo simulation the energy of all particles is known, we can build a condition for non-distorted events: $E_{LS} + E_{HPGe} = E_\gamma$ that is the energy deposed in the liquid scintillator plus the energy deposed in the HPGe detector should be equal to the

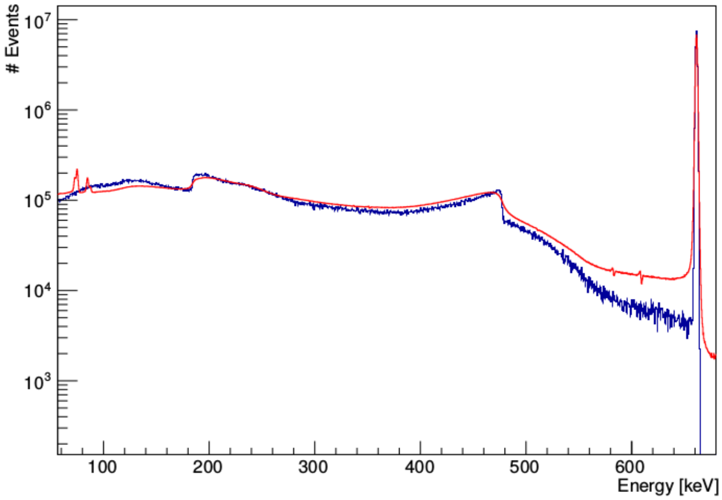

Figure 2.24: Comparison of the data (red) and Monte Carlo (blue) for HPGe detector. ^{137}Cs source. For Monte Carlo simulated data Gaussian smearing with approximate detector response function is applied.

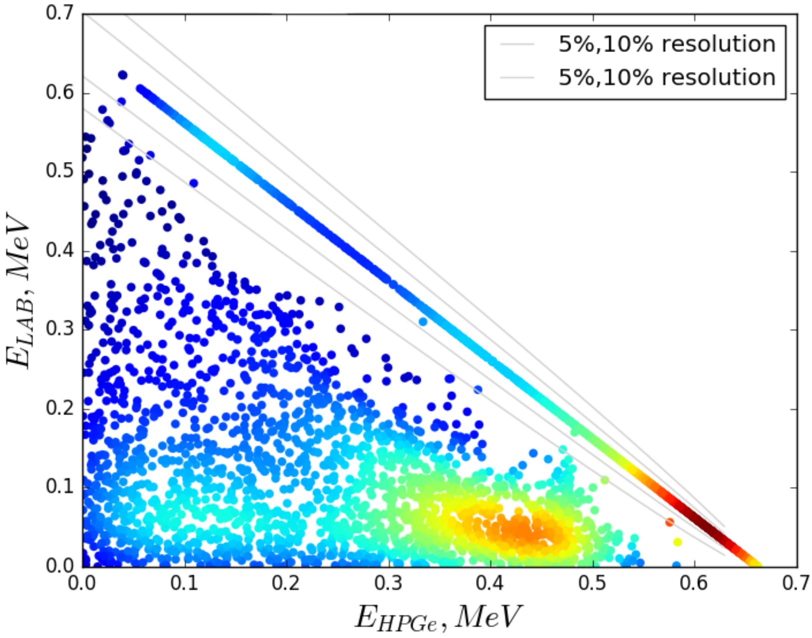

Figure 2.25: Scatter plot for the coincidence events. No quenching was yet applied.

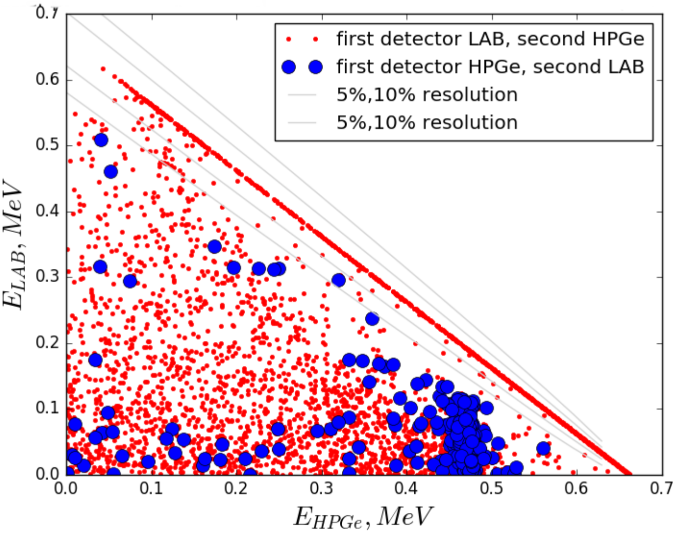

Figure 2.26: Scatter plot that represents the order of scattering in HPGe and liquid scintillator. The origin of the bulb at $E_{HPGe} \approx 0.48$ keV becomes clear: it is a backscattering which occurs in the HPGe first and then Compton scattering in the liquid scintillator

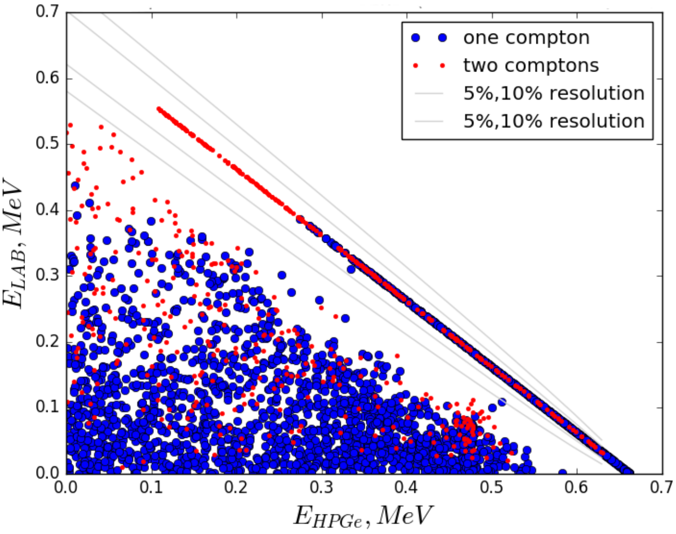

Figure 2.27: Scatter plot for events of single Compton and double Compton events.

energy of the incident gamma.

Another, alternative way to check if an event is biased by multiple Compton events is a condition which distinguish biased events at some level of acceptance ϵ_E (Ref. [17]):

$$|E_{MC}^{vis} - L(E_\gamma - E_{HPGe}, kB)| \leq \epsilon_E \tag{2.35}$$

where $E_{MC}^{vis} = \sum_i E_{Compton}^{vis} = \sum_i L(E_{Compton}, kB)$ is visible energy in the liquid scintillator and $L(E_\gamma - E_{HPGe}, kB)$ is an expected visible energy if only one Compton scattering event occurred. The function $L(T, kB)$ was previously defined by expression (2.11). ϵ_E is a parameter of acceptance that was set at $\epsilon_E = 0.15$ keV (0.5 % systematic deviation at 30 keV). This condition should be applied before smearing with energy resolution. The result of application of such condition is presented in Fig. 2.28 where events that were not accepted were indicated by red. As one may see the contribution of multiple Compton events, which produce significant deviation, is not that large in the energy range up to 80 keV. Thus, we can treat the effect of bias by multiple Compton events as not significant for non-linearity and intrinsic resolution measurement for a given experimental configuration.

Current data consists of the long run for ^{137}Cs source. The source was placed 20 deg off-axis of the HPGe detector. This angle corresponds to energy of electron $E_e = 47.97$ keV. Such energy will have an electron produced by gamma scattered in the very center of the cell. There is no collimation, so larger and smaller than 20 deg scattering angles are also possible. The data acquisition run consisted of six sub-runs (Table 2.3). Each sub-run included the HPGe calibration period (5-10 min), laser calibration (5-10 min) and coincidence acquisition periods (from 2 to 14 hours).

The time evolution of the energy scale of the detector could be compensated if the variation of the gain and baseline are corrected for both PMT and HPGe. HPGe calibration period provides information about the evolution of the energy scale, acquiring the data from two gamma sources. Laser calibration period acquires the low light level signals with a trigger from the laser. Finally, the coincidence acquisition period is used to measure non-linearity and resolution of the liquid scintillator.

Based on these considerations as well as additional analysis of χ^2, that is not provided here, the range $Q_{pmt}(2.3; 4.37)$ V $\cdot$ ns that corresponds to $N_{pe}(11.5, 21.8)$ was chosen. This range corresponds to HPGe energy 36.5-63.5 keV. One may increase the vertical range of DAQ to make this range larger; however, it introduces the problem of the baseline shift due to limited DAQ resolution.

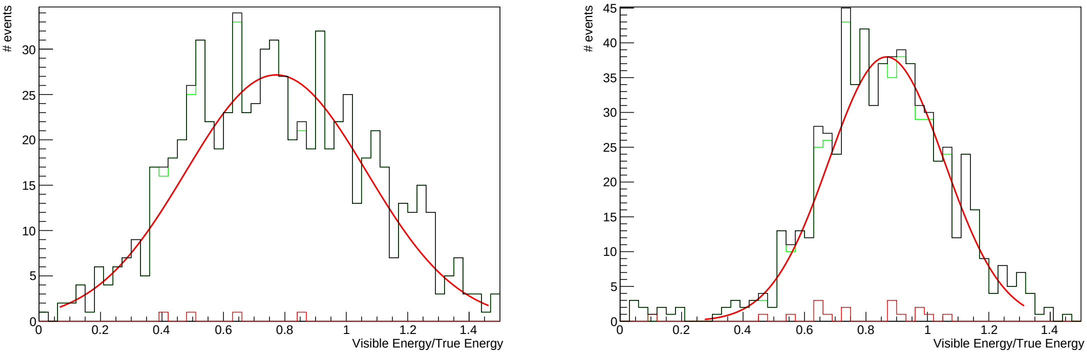

s

(a) $E_e = 20$ keV (b) $E_e = 50$ keV

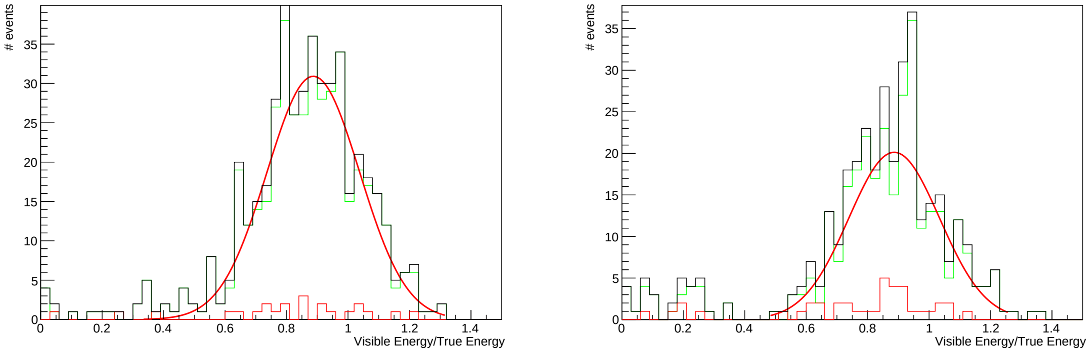

(c) $E_e = 80$ keV (d) $E_e = 100$ keV

Figure 2.28: Investigation of multiple Compton events systematic effect: examples of the slices for different energies. Events which were accepted by condition (2.35) are, represented by green, otherwise by red. (Ref. [17]). Configuration of the setup: $L_{source-cell} = L_{cell-detector} = 30$ cm, $\theta = 0$ deg.

Data analysis

Current data consists of the long run for ^{137}Cs source. The source was placed 20 deg off-axis of the HPGe detector. This angle corresponds to energy of electron $E_e = 47.97$ keV. Such energy will have an electron produced by gamma scattered in the very center of the cell. There is no collimation, so larger and smaller than 20 deg scattering angles are also possible. The data acquisition run consisted of six sub-runs (Table 2.3). Each sub-run included the HPGe calibration period (5-10 min), laser calibration (5-10 min) and coincidence acquisition periods (from 2 to 14 hours).

The time evolution of the energy scale of the detector could be compensated if the variation of the gain and baseline are corrected for both PMT and HPGe. HPGe calibration period provides information about the evolution of the energy scale, acquiring the data from two gamma sources. Laser calibration period acquires the low light level signals with a trigger from the laser. Finally, the coincidence acquisition period is used to measure non-linearity and resolution of the liquid scintillator.

Table 2.3: Run description. Subruns with HPGe, laser and coincidence periods duration in minutes.

subrun	HPGe	laser	Coincidence
1	10	14	90
2	10	10	94
3	11	10	105
4	11	10	120
5	10	14	14 hours 15 min
6	10	10	3 hours 46 min

PMT scale calibration, baseline calculation, and measurement of v_m

Laser period of subrun has several purposes: gain variation control, measurement of mean m_s and standard deviation σ_s of the charge of single photoelectron for charge Q_{pmt} PMT scale calibration in number of photoelectrons:

$$N_{p.e.} = Q/m_s \tag{2.36}$$

and v_{m_s} calculation as

$$v_{m_s} = (\frac{\sigma_s}{m_s})^2 \tag{2.37}$$

To achieve the single photoelectron regime (with mean number of photoelectrons $\mu \sim 1$) the intensity of the laser was adjusted by the variable optical attenuator. In Fig. 2.29 the fit with functions (2.33) and (2.34) of the acquired histogram is presented. The mean m_s and standard deviation σ_s of single photoelectron response are determined by both the first peak and exponential part.

The typical value of the single photoelectron charge was found to be

$$m_s \approx 0.2 - 0.21 \text{ V} \cdot \text{ns} \tag{2.38}$$

Gain variation peak to peak is about 5 % in approximately one day of acquisition.

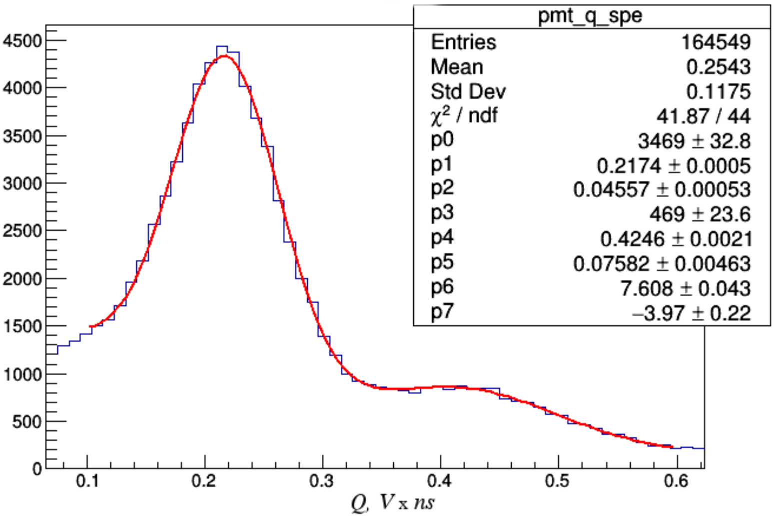

Figure 2.29: The fit of the PMT response with the function (2.33) to low light intensity signal with average number of photoelectrons $\mu \sim 1$ per laser trigger. Parameters m_{1s},σ_{m_1s} and m_{2s},σ_{m_2s} are denoted as p_1, p_2 and p_4, p_5, correspondingly.

Based on the acquired information the relative variance of single photoelectron response could be calculated:

$$v_{m_s} = 0.0496 \pm 0.0010\,(\text{stat}) \pm 0.0014\,(\text{syst}) \tag{2.39}$$

where statistical error δ_{v_m} was propagated from the relative errors of m_s and σ_s as:

$$\delta_{v_m} = 2v_{m_s}\sqrt{(\frac{\delta_{\sigma_s}}{\sigma_s})^2 + (\frac{\delta_{m_s}}{m_s})^2} \tag{2.40}$$

Systematic error is a standard deviation of the mean values for six independent measurements for each sub-run. Since v_m evolves with time as well it was decided to calculate it for each sub-run separately.

HPGe real-time calibration

Evolution of gain and baseline with time could easily spoil energy calibration of HPGe. It was decided to track the evolution of HPGe energy scale with calibration runs during the acquisition to avoid this problem. The energy scale of HPGe in the energy range of interest was found to be very linear, so practically two points are enough to fix it. During each HPGe acquisition period, ^{210}Bi source was adjusted.

For the fit of the full absorption peak a combination of two functions are chosen: "crystal ball function" that can well reproduce the asymmetrical distributions with a tail at lower energies (see long and short-term tail in Fig. 2.13) (Ref. [110]):

$$f_{crystal}(x; C, \bar{x}, \sigma, n, \alpha) = C \cdot N(n, \alpha) \cdot \begin{cases} exp(-\frac{(x-\bar{x})^2}{2\sigma^2}), \text{for } \frac{x-\bar{x}}{\sigma} > -\alpha \\ A(n,\alpha) \cdot (B(n,\alpha) - \frac{x-\bar{x}}{\sigma})^{-n}, \text{for } \frac{x-\bar{x}}{\sigma} \leq -\alpha \end{cases} \tag{2.41}$$

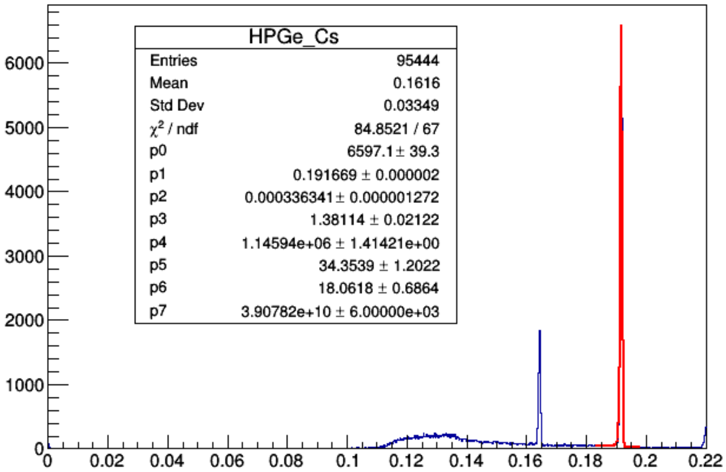

Figure 2.30: The fit of the ^{137}Cs gamma absorption peak. $\chi^2/Ndf \sim 1.27$. The meaning of parameters: $p_0 = C$, $p_1 = \bar{x}$, $p_2 = \sigma$, $p_3 = n$, $p_4 = \alpha$, $p_5 = a$, $p_6 = b$, $p_7 = c$.

and Fermi step-like function to reproduce background continuum (background continuum, Fig.2.13):

$$f_{fermi}(x; a, b, c, \bar{x}) = \frac{a}{1 + exp[(x - \bar{x})/c]} + b \tag{2.42}$$

The fits have $\chi^2/Ndf \sim 1.5 - 2$ (Fig. 2.30). The study of residuals of the fit reveals oscillating behavior of neighboring bins (Fig. 2.31). Thus, most probably the problem of the high χ^2 is related to binning. The DAQ resolution determines actual bin size, and it is 3 times bigger than optimal bin size $\sigma/5$ (Ref. [111]). Thus, it is necessary to have a DAQ module that has at least 12-bit resolution. It is better to have several points (let us say four) per 1 bin to avoid the problem of oscillation; thus 14-bits is a requirement.

Despite the fact of bad χ^2/Ndf the determination of the $\bar{x}$ is quite precise thanks to relatively small $\sigma = 3 \cdot 10^{-4}$ V · ns and large number of counts in the peak $N \approx 2.5 \times 10^4$.

the standard error of the mean (SEM) is given as

$$\delta_{\bar{x}}^{SEM} = \sigma/\sqrt{N} \approx 1.9 \cdot 10^{-6}\ \mathrm{V \cdot ns} \tag{2.43}$$

it is similar to the fit result $\delta_{\bar{x}}^{fit} = 2 \cdot 10^{-6}$ that is $10^{-3}\%$ or $6\ eV$ in energy units. Even if we exceed this value by a factor of 10 the time evolution of the full energy peak position still could be distinguished (Fig.2.32, note the error bars are increased by factor 10). The variation of just 0.25 % peak-to-peak leads to the shift of the energy scale by 1.3 keV which, as we will see further, is quite large for non-linearity analysis. Therefore, the compensation of non-linearity measurements of HPGe energy scale is necessary. The impact of HPGe energy scale shift on kB measurement will be presented further in the context of the study of systematic effects. In any case, the systematic error of the E_e due to the slicing of the two-dimensional histogram is quite large, being half of the slice or 0.5 keV. Therefore the compensation of the energy scale should eliminate the systematic

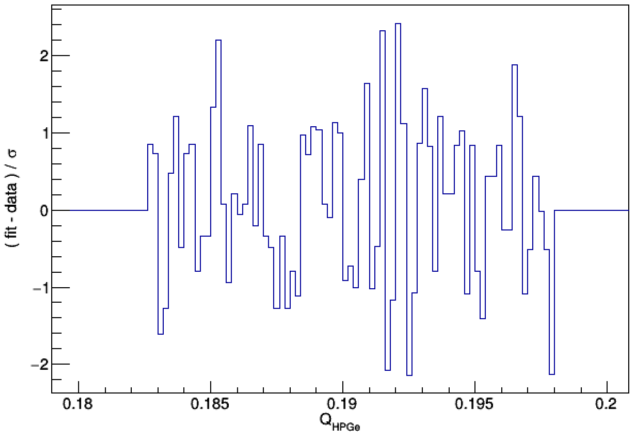

Figure 2.31: Residuals for the histogram fit Fig. 2.30. Oscillating behavior suggest the problem with binning: the bin size which is dictated by DAQ resolution is too large, violating the recommendation "binsize $= \sigma/5$".

effect related to it. On the contrary, the shift of the HPGe energy scale is not relevant for the energy resolution measurement.

Correction of the energy scales

The scales of PMT and HPGe should be corrected with calibrations periods provided at the beginning and the end of the coincidence period of a sub-run.

The charge collected by PMT was corrected and normalized to provide $m_s = 0.2V \cdot ns$ for all sets of the data:

$$Q = \frac{0.2(Q - b(t))}{m_s(t)} \tag{2.44}$$

where $m_s(t)$ and b are single photoelectron amplitude and baseline in a given time t of acquisition.

For HPGe detector we have an evolution of the coefficients $s(t)$ and $m(t)$ and relation

$$E = K(t) \times Q + B(t) \tag{2.45}$$

which determines the conversion of the energy scale. The evolution in time of PMT and HPGe is supposed to be linear for each sub-run. This is a reasonable assumption (see Fig. 2.32 as well as Fig. 2.21 and Fig. 2.17).

In linear approximation we have the expression for evolution of the parameter η that could be m_s, b , K or B:

$$\eta(t) = (\eta_{start} - \eta_{end})(t - t_{start})/(t_{end} - t_{start}) + \eta_{start} \tag{2.46}$$

where t_{start} and t_{end} are moments when coincidence period starts and stops, $\eta_{start} = \eta(t_{start})$ and $\eta_{end} = \eta(t_{end})$.

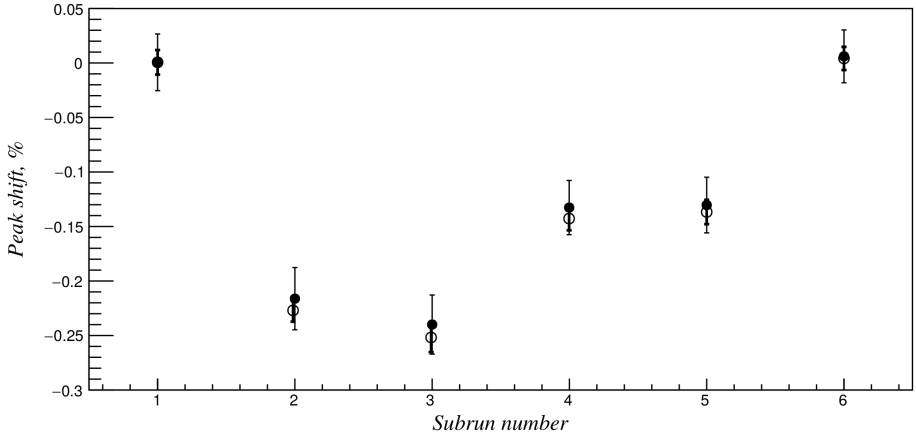

Figure 2.32: Stability plot for 6 subruns. Evolution of the shift of full absorption peaks for ^{137}Cs (empty circles) and ^{207}Bi (filled circles) expressed in %. Note that experimental error are 10 times enlarged.

Coincidence histogram. Slicing.

The most extended sub-run 5 was used for the analysis. Applying calibrations and correction of the energy scale and expressing the energy of Compton electron via energy deposed in the HPGe, we can obtain coincidence histogram with E_e versus Q_{pmt} shown in Fig 2.33.

Cutting in 1 keV slices along the x-axis and projecting the result on y-axis provides one-dimensional histograms for the fit to determine the response of the liquid scintillator to the electron with energy E_e.

For each slice a sum of Gaussian (C,Q,σ_Q) and 1-order polynomial (a_0,a_1) functions was chosen for fitting. It reproduces well the profile of the peak for a given energy of the electron (Fig. 2.36).

The χ^2/Ndf versus slice number is presented in Fig. 2.37. $<\chi^2/Ndf>= 1.1$ in the range of the analysis (slices with number between 36 and 63 or $E_e = 36.5 - 63.5$ keV). The fit results for mean value of charge Q_{pmt} and standard deviation $\sigma_{Q_{pmt}}$ of each slice are presented in Fig.2.34 and Fig.2.35.

The range of the analysis is determined by discriminator threshold at low energies and dynamic range of the DAQ (vertical range and offset). The effect of PMT non-linearity is not significant since the upper range V_{max} is quite far from saturation (the value provided by the manufacturer is 2 % non-linearity at 1.5 V). The signals which are close to the threshold ($Q \sim 1.5$V $\times$ ns) and maximum of the acquisition vertical range ($Q \sim 4.5V \times ns$) could be distorted (see Fig. 2.38). Also at low energies the response may became Poissonian (for $N_{pe} < 10$ p.e. or $Q < 2$) and Gaussian fitting became not valid anymore.

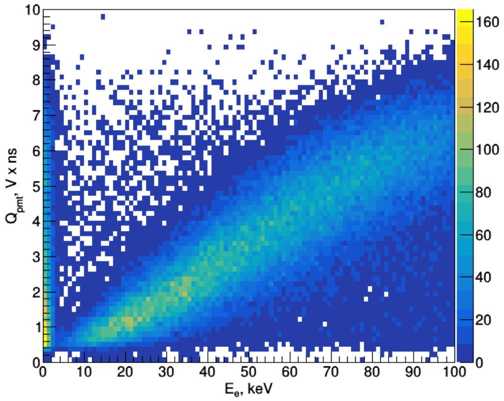

Figure 2.33: Coincidence histogram for electrons produced by scattered gamma. Diagonal structure contains information about the non-linearity and energy resolution of the liquid scintillator.

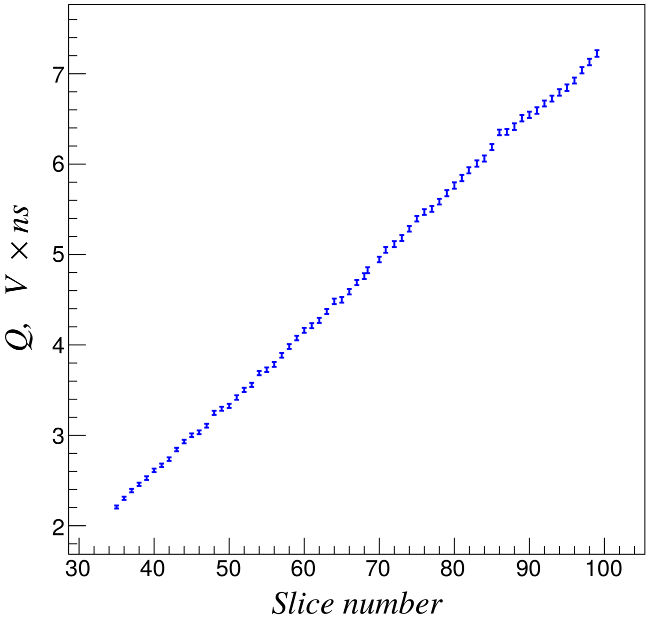

Figure 2.34: The result for the mean value of the peak $Q \pm \delta_Q$ versus slice number.

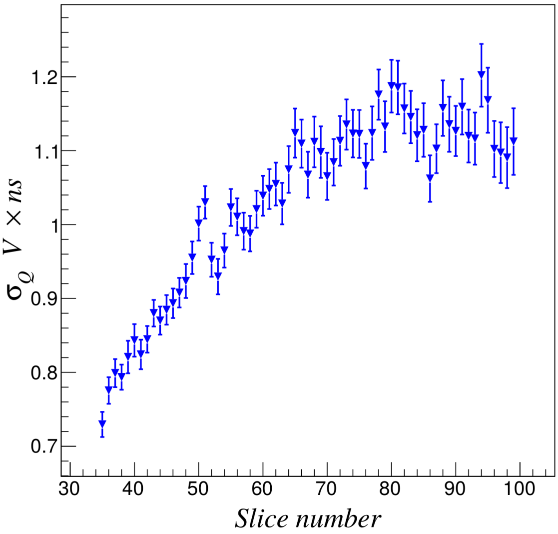

Figure 2.35: The result for the standard deviation of the peak $\sigma_Q \pm \delta_{\sigma_Q}$ versus slice number.

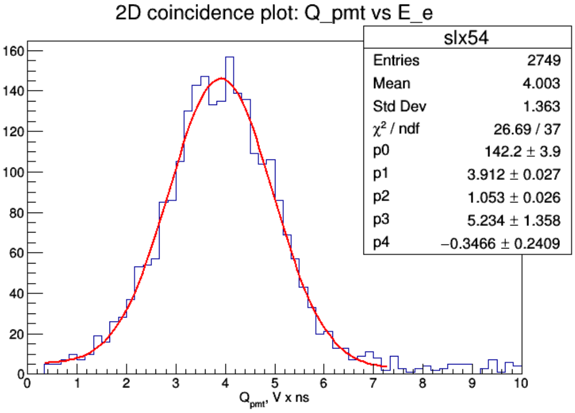

Figure 2.36: Example of the fit of the 1 keV slice (a cut of 2d coincidence diagram along x-axis). The meaning of parameters: Gauss $p_0 = C$, $p_1 = Q$, $p_2 = \sigma_Q$ and polynomial $p_3 = a_0$, $p_4 = a_1$

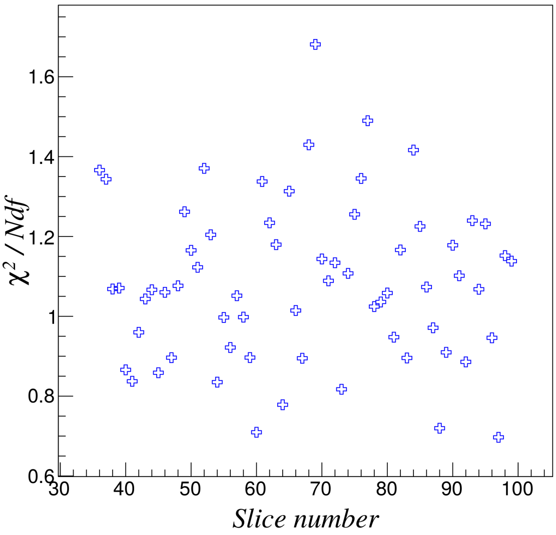

Figure 2.37: The goodness of the fit: χ^2/Ndf versus slice number.

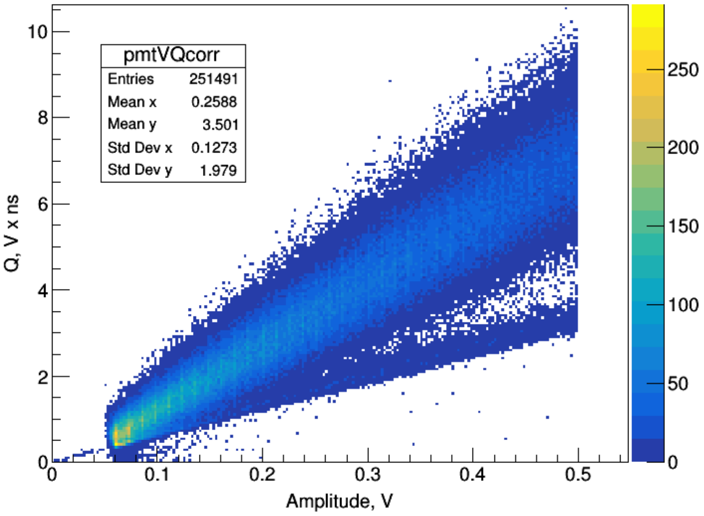

Figure 2.38: The diagram of the amplitude in Volts versus integral charge Q in V × ns. The signals which are close to the threshold ($Q \sim 1.5$ V × ns) and maximum of the acquisition vertical range ($Q \sim 4.5$ V × ns) could be distorted.

Based on these considerations as well as additional analysis of χ^2, that is not provided here, the range $Q_{pmt}(2.3; 4.37)$ V · ns that corresponds to $N_{pe}(11.5, 21.8)$ was chosen. This range corresponds to HPGe energy 36.5-63.5 keV. One may increase the vertical range of DAQ to make this range larger; however, it introduces the problem of the base-

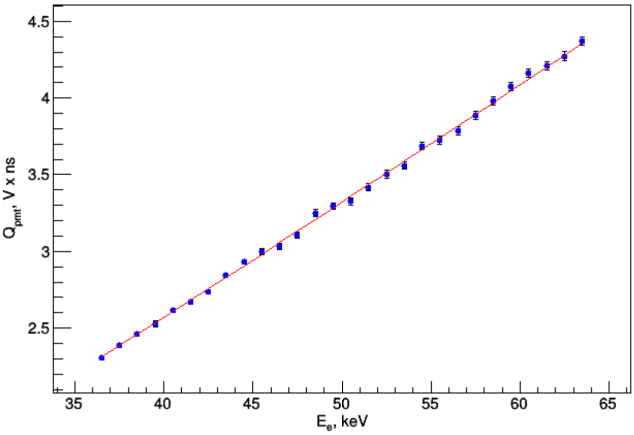

Figure 2.39: Fit of the $Q \pm \delta_Q$ with a function $LY(Y_p, kB)$ (Expression. 2.10). $\chi^2/Ndf = 22/28$.

line shift due to limited DAQ resolution.

Results

Non-linearity determination

One can extract information about non-linearity of the liquid scintillator performing the fit of the curve in Fig. 2.34 in the energy range of the analysis with expression (2.10) with two free parameters: light yield Y_p and quenching factor kB. Even though the range of the analysis is small, experimental points fix the parameter kB quite well. Though Monte Carlo preliminary studies showed that the contribution of multiple Compton events in the analysis range is small, the more detailed investigation should be performed to estimate this effect. Another critical factor which is still beyond of discussion is the light collection inhomogeneity that may introduce bias as well. Since small ,we assumed that light collection effect is negligible. This assumption could be verified in the future Monte Carlo simulation studies.

The fit gives

$$kB = 0.0195 \pm 0.022 \text{ (stat) cm/MeV}, \tag{2.47}$$

which corresponds to about 8 % relative error. It is quite good statistical error compared to the determination of kB by calibrations with sources in large liquid scintillator detector, e.g. 6 % for Borexino (Ref. [91]). The statistical error of experimental points is $\delta_Q = \sigma_Q/\sqrt{N}$. This error could be reduced by acquiring more data to increase the precision of the Q determination. Increase of the light collection of the setup also improve the result: in this case σ_Q is reduced.

To take into account systematic effect of the HPGe energy scale shift we performed two other fits with $E_{HPGe} + 0.5$ keV and $E_{HPGe} - 0.5$ keV. In principle, this systematic effect of the slicing could be determined by means of the analysis of Monte Carlo simulated data what is planned in further studies. With 0.5 keV shifted energy scale, we have:

$$kB_{+0.5} = 0.022 \pm 0.00185 \text{ (stat) cm/MeV} \tag{2.48}$$

for $E_{HPGe} + 0.5$ keV and

$$kB_{-0.5} = 0.0172 \pm 0.0015 \text{ (stat) cm/MeV} \tag{2.49}$$

for $E_{HPGe} - 0.5$ keV.

Incorporating all three results, we finally obtain

$$kB = 0.0196 \pm 0.0019\text{(stat)} \pm 0.0024 \text{ (syst) cm/MeV} \tag{2.50}$$

with a very conservative systematic error estimation that could be reduced in the future analysis. So far, the result has a total precision 16 %. As it was told before the bias due to double Compton events and light collection inhomogeneity should be taken into account to obtain an actual kB of liquid scintillator.

To make threshold lower significantly and to catch up the most essential and truly non-linear part of the measurement, one needs to achieve higher photoelectron light yield to avoid close-to-threshold deformations and Poissonian statistics at lower energies. So far the threshold ~35 keV (~10 p.e.) was achieved. Still, there is room for increasing photoelectron yield by the factor of 3 to achieve 10 keV threshold.

Intrinsic energy resolution

From the fit of the slices it is possible to obtain $v_Q(E_e)$, the variance of the charge Q as a function of electron energy (2.19):

$$v_Q(E_e) = \frac{\sigma_Q^2}{Q^2} \tag{2.51}$$

As we discussed in Section 2.7 it consists of four contributions: statistical term $v_{st} = \frac{1+v_m}{N_{p.e.}}$, light collection term v_p, intrinsic resolution term v_{int} and dark noise term v_d. The dark noise v_d term is completely negligible for our setup since the probability to obtain a dark pulse in the 200 ns acquisition window with typical dark rate about 2 kcps is 0.04 %. The term v_{int} is of interest for us and it could be found as

$$v_{int} = v_Q - v_{st} - v_p \tag{2.52}$$

The first term v_{st} could be precisely determined since both values $N_{p.e.}$ and v_m are available from the PMT scale calibration. It is believed that this term can be reduced by a factor 3 by increasing the light collection and therefore photoelectron yield. The current value is about 450 p.e. at 1 MeV that corresponds to the photoelectron yield found in Borexino (Ref. [91]). The factor three improvement will make it closer to the yield of JUNO detector. For this purpose, the plane window PMT [9] have to be used, and the system have to be optically optimized.

There is no way to determine v_p from this measurement. In principle, v_p could be estimated by optical Monte Carlo simulations. However, the reliability of such simulations should be verified to ensure correctness of estimation[10]. Though before simulations it

---

[9] One can also consider a configuration when two PMTs are coupled from two sides of the cell (as in Ref. [105]). It increases overall photocathode coverage and reduces the role of the reflectively index of the walls of the cell

[10] Light collection inhomogeneity may produce visible energy-dependent effects on 2d coincidence diagram such as shifts of the energy response for certain energies. One may think about usage of this fact for Monte Carlo verification: it probably could reproduce these effects

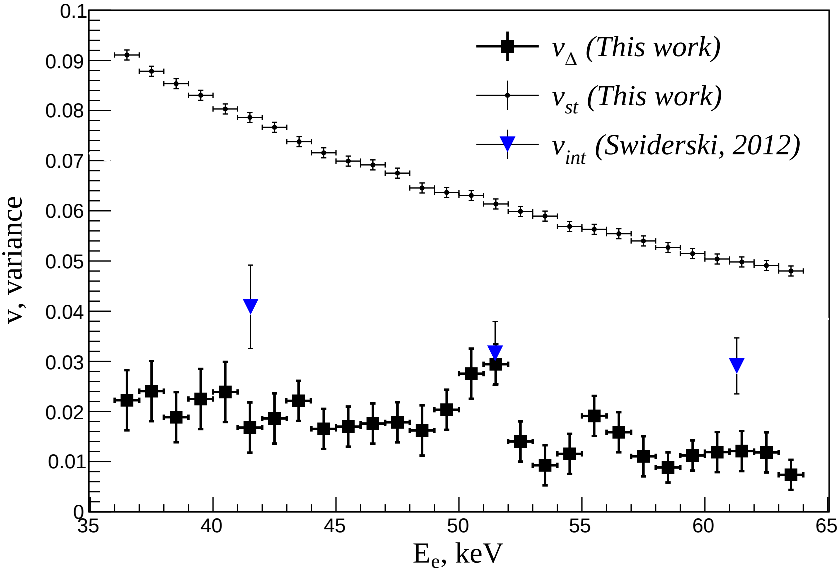

Figure 2.40: The $v_\Delta = v_p + v_{int}$ term (large black squares) and statistical term v_{st} (small black dots) in the energy range 36-63 keV. The result for v_{int} from Ref. [18] (triangles) is provided for comparison.

would be better to optimize the setup by increasing the light collection and reducing the uncertainties related with the optical properties of the system [11]. As the rule of thumb, the bigger the light collection is, the smaller is its variation. Recommendations that are valid for the reduction of the v_{st} are also valid for v_p.

Since the v_p component is not yet determined, it is possible to measure only the sum of intrinsic energy and light collection terms $v_\Delta = v_{int} + v_p$:

$$v_\Delta = v_{int} + v_p = v_Q - v_{st} = v_Q - \frac{1 + v_m}{N_{p.e.}} \tag{2.53}$$

v_Δ extracted from the analysis of the data permits to make a valuable conclusion about the size of the intrinsic resolution effect: the maximum contribution of intrinsic energy resolution into the total variance will be:

$$v_{int}^{max} = v_\Delta \tag{2.54}$$

Both terms $v_Q = (\frac{\sigma_Q}{Q})^2$ and $v_{st} = \frac{1+v_m}{N_{pe}} = \frac{1+(\frac{\sigma_s}{m_s})^2}{Q/m_s}$ depend on the Q and correlate. Thus, for error propagation of v_Δ it is necessary to consider both terms together:

$$v_\Delta = v_\Delta(Q, \sigma_Q, m_s, \sigma_s) = (\frac{\sigma_Q}{Q})^2 - \frac{1 + (\frac{\sigma_s}{m_s})^2}{Q/m_s} \tag{2.55}$$

with error calculated:

---

[11] Reduction of the overall optical complexity of the setup increases the reliability of the simulations. If the geometry of the setup is simple and light collection very high, only one parameter, the reflection of the walls, could be chosen to describe the effect of the light collection

Table 2.4: Error propagation terms for $v_\Delta(Q, \sigma_Q, m_s, \sigma_s)$ and their characteristic values for $E_e = 50.5$ keV.

$\frac{\partial v_\Delta}{\partial Q}$	$\frac{\partial v_\Delta}{\partial \sigma_Q}$	$\frac{\partial v_\Delta}{\partial m_s}$	$\frac{\partial v_\Delta}{\partial \sigma_s}$	$\frac{\partial^2 v_\Delta}{\partial Q \partial \sigma_Q}$	$\frac{\partial^2 v_\Delta}{\partial m_s \partial \sigma_s}$
$-(v_\Delta + v_Q)/Q$	$2\sqrt{v_Q}/Q$	$(v_m - 1)/Q$	$-2\sqrt{v_m}/Q$	$-4\sigma_Q/Q^3$	$2\sigma_s/(m_s^2 Q)$
$(\frac{\partial v_\Delta}{\partial Q}\delta_Q)^2$	$(\frac{\partial v_\Delta}{\partial \sigma_Q}\delta_{\sigma_Q})^2$	$(\frac{\partial v_\Delta}{\partial m_s}\delta_{m_s})^2$	$(\frac{\partial v_\Delta}{\partial \sigma_s}\delta_{\sigma_s})^2$	$\frac{\partial^2 v_\Delta}{\partial Q \partial \sigma_Q}\delta_{Q\sigma_Q}$	$\frac{\partial^2 v_\Delta}{\partial m_s \partial \sigma_s}\delta_{m_s\sigma_s}$
7×10^{-7}	1×10^{-5}	3.3×10^{-7}	4.5×10^{-7}	2.9×10^{-6}	-2.9×10^{-8}

$$\delta_{v_\Delta}^2 = \sum_{\xi = Q, \sigma_Q, m_s, \sigma_s} (\frac{\partial v_\Delta}{\partial \xi})^2 \delta_\xi^2 + \frac{\partial^2 v_\Delta}{\partial Q \partial \sigma_Q}\delta_{Q\sigma_Q} + \frac{\partial^2 v_\Delta}{\partial m_s \partial \sigma_s}\delta_{m_s\sigma_s} \tag{2.56}$$

The analysis of the typical values of terms (Table. 2.4) suggests that the dominating term is

$$(\frac{\partial v_\Delta}{\partial \sigma_Q}\delta_{\sigma_Q})^2 = 4 v_Q (\delta_{\sigma_Q})^2 / Q^2 \tag{2.57}$$

It suggests that the result could be improved using higher statistics acquired to increase the precision of σ_Q. For four times reduction, we should have 16 times more statistics (instead of 14 hours x 14 μCi of sub-run 5, one needs to acquire 9 days x 14 μ Ci), which is quite time-consuming. Since the term is proportional to the v_Q as well, the improvement of the precision is also possible if the total energy resolution will be increased, that could be achieved through the improved light collection. General expression for the scaling of the data-taking time is

$$\sim \frac{1}{(N_{p.e.}/450\,\text{p.e.})\sqrt{t/t_0}} \tag{2.58}$$

where $t_0 = 14\text{hours} \times 14\mu\text{Ci}$

Improvement of the light collection also reduces the contribution of the v_p into the v_δ, making the presence of the v_{int} more evident.

The results for v_Δ measurement are shown in Fig. 2.40 by large black squares. By small black dots the statistical term v_{st} is presented. The effect of the presence of v_Δ term is quite robust. The v_{int} term in a EJ301 liquid scintillator from Ref. [18] (triangles) is provided for comparison. Even though the liquid scintillators are different, it is the only data available in literature. It is not possible to derive a definite conclusion about the presence of v_{int} since v_p contribution remains unknown. It is probable that large v_Δ is generated by variance of light collection term v_p and $v_p > v_{int}$. Further investigation that includes optical Monte Carlo simulations and determination of v_p are necessary. With the further upgrade of experimental setup by increasing the light collection, in principle, the regime $v_p < v_{int}$ could be achieved. In this case, the experimental technique will permit v_{int} discovery.

Conclusions

The 3 % energy resolution at MeV and 1 % energy scale uncertainty are the crucial requirements for reactor neutrino program realization of JUNO that includes Mass Hierarchy determination, CC NSI measurement, the study of the fine structure of the antineutrino spectrum and other topics. Moreover, these parameters determine an overall ability of the detector to distinguish signals from backgrounds by energy spectrum fitting procedure. This chapter was dedicated to the description and investigation of non-linear energy response and energy resolution of the liquid organic scintillator, since their great importance for large-scale detectors.

Starting from the first principles of propagation of electrons (positrons) and gamma quanta in media and introducing ionization quenching and Cherenkov radiation phenomena, the full description of the energy scale in the energy range up to 100 MeV were provided. It was shown that the quenching and Cherenkov contributions into the total energy scale non-linearity could be decoupled, thus suggesting the range up to 100 keV to be sufficient for the measurement of the Birks' ionization quenching constant kB.

This range is supposed to be optimal for intrinsic energy resolution measurement as well since, if the hypothesis about the origin of intrinsic energy resolution due to delta-electrons fluctuations and non-linear response of the liquid scintillator is correct, the effect is expected to be the strongest.

It was shown that non-linear effects are relevant not only in the energy range below 1 MeV but also manifest themselves at higher energies due to radiative energy losses with the strength that depends on the fraction of Cherenkov light in the total energy losses.

We mainly focused on the liquid scintillator contribution to the energy scale non-linearity and energy resolution. Other effects (such as the main statistical term or light collection contribution into non-linearity and energy resolution) were investigated only for the determination of kB and v_{int}.

Theoretical consideration of the system (PMT+liquid scintillator) provided us with an expression that described energy resolution of the detector in the most general way and gave a mathematically strict definition of the intrinsic energy resolution term. This description gave a clue for intrinsic energy resolution measurement.

In this work, I treated kB and v_{int} as a properties of the liquid scintillator by itself and *invariant* under the change of experimental apparatus for a given liquid scintillation recipe and temperature conditions. Thus, if all systematic effects are appropriately taken into account, these values should be found the same in small and large experimental apparatus.

In the second part of the chapter, I present the development of the experimental technique for characterization of liquid scintillation response to electrons. It is based on the Compton coincidence techniques with High Purity Germanium (HPGe) for scattered gamma detection. The energy of an electron is reconstructed from the difference between initial energy of a gamma and energy of scattered gamma deposed in the spectrometer.

Experimental apparatus was constructed using the equipment available in the laboratory. HPGe detector was calibrated in units of energy. The stability of the system was carefully examined and experimental data corrected to reduce the systematic effects of instabilities on measured quantities.

The photomultiplier tube was calibrated in units of photoelectrons and v_m was measured, providing a precise determination of the statistical term.

For overall optimization of the setup and the study of systematic effects, induced by multiple Compton scattering, the Monte Carlo simulation program was developed.

The analysis was limited by the window 36-64 keV due to the presence of the threshold at low energies and upper vertical range border of DAQ. The data in this window was fitted with Birks' model to determine kB including a conservative systematic error due to the slicing procedure.

Data analysis of the coincidence histogram and the fit with $L(T_{kin}, kB)$ function provided the ionization quenching constant value:

$$kB = 0.0196 \pm 0.0019\,\text{(stat)} \pm 0.0024\,\text{(syst)}\ \text{cm/MeV}$$

By the calibration of the PMT, the statistical term v_{st} was precisely determined and the contribution of the intrinsic energy resolution v_{int} was extracted from the total relative variance v_Q as $v_{int} = v_Q - v_{st}$.

The magnitude of IER was smaller compared with the value found in Ref. [18] for EJ301 liquid scintillator. However, since both effects should depend on the type and composition of the liquid scintillator the comparison with the present data is only indicative.

The result was obtained assuming that the effects of the light collection could be neglected ($v_p/v_Q << 1$). As an outlook, the precise estimation of the light collection for this setup configuration should be conducted in order to ensure that the contribution of v_p is not significant to mimic the observed intrinsic resolution effect.

CHAPTER 3

JUNO liquid scintillator purification test

Introduction

A crucial requirement for low energy neutrino detection is radiopurity of the detector target: in the range of solar (0.1 - 15 MeV) and reactor neutrino physics (1 - 10 MeV) several radiative isotopes can mimic signal from neutrinos. The relatively high natural presence of ^{238}U and ^{232}Th in liquid scintillator in the form of dust and organometallic compounds became a challenge for large-scale liquid scintillator experiments. This challenge could be overcome with several *purification techniques*.

Use of IBD reaction makes radiopurity requirements softer since neutrino signal has a coincidence tag and could be discriminated from backgrounds. Still, there is a possibility for a random coincidence of signal and background that dictates minimal permissible concentrations of contaminants. Current concentration C requirements (in grams of the element per gram of LS) for Mass Hierarchy determination are

$$C < 10^{-15}\mathrm{g/g} \tag{3.1}$$

for both ^{238}U and ^{232}Th (Ref. [9], [112]).

Solar neutrino program is more challenging than the mass hierarchy determination. It uses elastic neutrino scattering reaction that doesn't have a coincidence tag and requires one order of magnitude smaller concentrations of contaminants to achieve good signal/background ratio.

The purification results for Borexino detector (Ref. [113]) are ^{238}U and ^{232}Th $< 10^{-18}$g/g, three order of magnitude better than requirement (3.1) for reactor neutrino detection and one hundred times better than solar neutrino requirement. Therefore, technologies and experience gained during Borexino design and operation guarantee that the requirement (3.1) can be achieved.

Such tiny concentrations could not be detected by any method in an above-ground laboratory. Therefore, the only way to check the radiopurity of the LS at such a low level is to fill large and sensitive enough detector located underground.

Apart from ^{238}U and ^{232}Th there are other radioactive isotopes that may significantly contribute to background (Table 3.1). For example, ^{40}K that could be found in PPO. PPO crystals may have higher ^{40}K concentrations with respect to linear alkylbenzene being produced synthetically. Once linear alkylbenzene is mixed with PPO, ions of ^{40}K should be removed from the solution. Another relevant sources of background are gaseous ^{222}Rn, ^{85}Kr and ^{39}Ar. All three are presented in air: ^{222}Rn $\sim 10 - 100$ Bq/m^3, ^{85}Kr $\sim$ 1 Bq/m^3 and ^{39}Ar $\sim$ 16 mBq/m^3. Moreover, ^{222}Rn, being part of the ^{238}U-chain, can be emanated from materials. To avoid gaseous contamination the entire detector and filling system should be leak tight and gas stripping should be performed to extract contamination dissolved in liquid scintillator (Sec. 3.2). The presence of ^{222}Rn in detector could an indication of an air leak in the storage, purification plants or in the detector.

Particular attention should be given to all interior cleaning of detector and filling system to reduce the amount of parent ^{210}Pb isotope attached to the surface, another important source of background.

Some other sources of background, ^{11}C, ^{14}C and ^{7}Be produced by cosmic ray activation, are not covered in this study. The first one is intrinsically presented in LS since its organic nature.

Table 3.1: The list of main contaminants of liquid scintillator and removal strategy

Radioisotope	Contamination source	Typical value	Removal strategy	JUNO requirement
^{222}Rn	Air, emanation from materials	< 100Bq/m^3	Stripping	-
^{238}U	Dust suspended in liquid	10^{-6}g/g	Distillation and Water Extraction	$< 10^{-15}$g/g
^{232}Th	Dust suspended in liquid	10^{-5}g/g	Distillation and Water Extraction	$< 10^{-15}$g/g
^{40}K	PPO used as doping material	10^{-6}g/g	Water Extraction	$< 10^{-15}$g/g
^{39}Ar, ^{42}Ar	Air	1Bq/m^3	Stripping	-
^{85}Kr	Air	1Bq/m^3	Stripping	1μBq/m^3

The level of contamination of the liquid scintillator by some element $\frac{m_{element}}{m_{LS}}$ could be well estimated with the rate of their radioactive decays $rate_{decay}$:

$$\frac{m_{element}}{m_{LS}}[\mathrm{g/g}] = \frac{rate_{decay}[\mathrm{Bq/m^3}]T_{1/2}M}{ln2N_A\rho[\mathrm{g/m^3}]10^6}, \tag{3.2}$$

where $T_{1/2}$, M and ρ are half-life, molar mass and density of the element. Usually, only some part ϵ of decay events is detected, and measured rate should be corrected to obtain the rate of radiative decays:

$$rate_{decay} = rate_{measured}/\epsilon \tag{3.3}$$

Therefore, the problem of the estimation of the concentrations consists of the determination of the experimental rate $rate_{measured}$ and efficiency ϵ of detection.

Let us suppose that secular equilibrium in the radioactive chains of ^{238}U and ^{232}Th is established. The rates could be determined by coincidences between ^{214}Bi (β Q-Value: 3.27 MeV) and ^{214}Po (α 7.8 MeV) for ^{238}U (^{222}Rn) and between ^{212}Bi (β Q-Value: 2.25 MeV (64 %); α 6.2 MeV (36 %)) and ^{212}Po (α 8.9 MeV) for ^{232}Th. Thanks to relatively short life-time of ^{214}Po ($T_{1/2} = 164.3\mu$s) and ^{212}Po ($T_{1/2} = 0.29\mu$s) the coincidences could be clearly distinguished in a whole set of triggered data.

Other important issues are optical transparency and the absolute liquid yield of the liquid scintillator. They determine the total number of detected photoelectrons and, therefore, the statistical term of the energy resolution (chapter 2). In Sec. 3.3 the results on transparency characterization of liquid scintillator are discussed. Search for an optimal LAB+PPO+bis-MSB composition of the liquid scintillator goes beyond the current scope of this study.

To test purification technologies, estimating radioactive contamination as well as investigate optical properties, it was decided to build a prototype of a purification system which consists of four pilot plants. Each one corresponds to a distinct process of purification: alumina oxide filtration, distillation, water extraction and gas stripping. JUNO Milan group was responsible for distillation and stripping plants. Their description is given in Sec. 3.2. Alumina oxide and water extraction plants were designed and operated by Chinese colleagues. The summary of contaminants mentioned above and corresponding purification strategy are provided in Table 3.1.

The system was placed in underground experimental hall 5 of Daya Bay experiment to perform a test in conditions that are very close to the future filling and operation of JUNO. One of Daya Bay detectors was connected to the system to be used as a prototype detector. In advance, Daya Bay liquid scintillator was replaced with ultra-pure water to be refilled with liquid scintillator of JUNO. In the next subsections the general information on detector geometry, acquired data set and fiducial volume are provided. I took part in pilot plants test conducted in February-March 2017. Based on data acquired from Daya Bay detector I established an estimation of the radiation contamination of ^{238}U and ^{232}Th presented in Sec. 3.4 and 3.5.

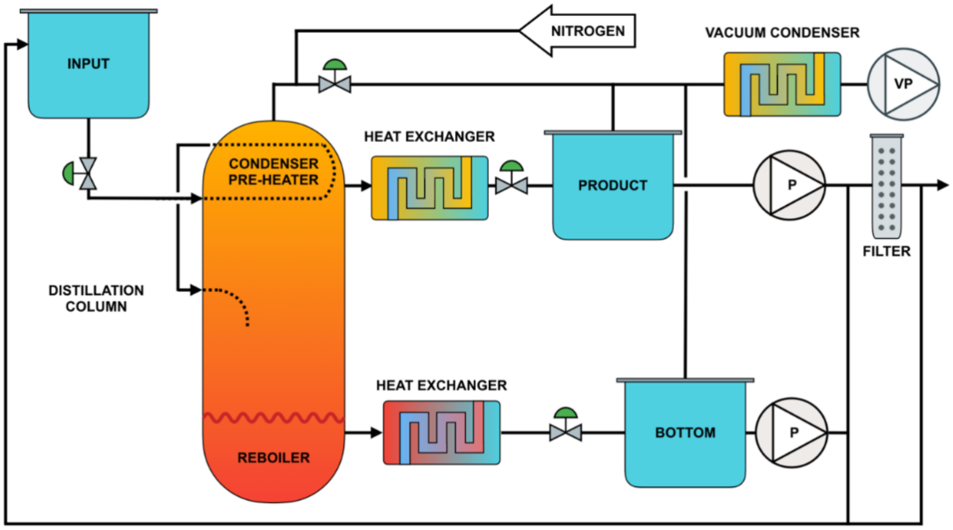

Figure 3.1: Distillation pilot plant sketch (see the text for a description)

Distillation and stripping pilot plants

Distillation

The process of distillation is well suited for removal of ^{238}U and ^{232}Th as well as extracting heavy fractions of liquid scintillator which may degrade optical transparency in the range 350-550 nm. The sketch of distillation pilot plant is shown in Fig.3.1. The principal part of the plant is 7 m high and 20 cm large column with 15 kW electric reboiler (heater) and condenser-preheater on the bottom and top, correspondingly. 6 sieve trays separate space between reboiler and condenser-preheated with holes. The LAB from the input tank is fed to the column in the middle tray section at a flow rate of 102 l/hour. It is preheated in upper section of the column up to 160°C. Counter-current flow of liquid (that falls) and gas (goes up) is organized in the column. The trays are placed to establish a close contact of two phases to perform heat and mass transfer from vapor to liquid. This process enriches the liquid flow with heavy impurities, reducing contamination in up-going flow and the temperature of the vapor. Finally, vapor reaches the condenser where some part of the liquefied scintillator is directed into the product tank, and another part flows down forming a downstream of the LAB. When liquid exits from the column in the product and the bottom tanks it is cooled in heat exchangers down to ambient temperate. Two diaphragm pumps guide the flow of LAB from the product (100 l/hour) and the bottom (2 l/hour) tanks. Before being sent to the next stage of purification, output flow passes through 50 nm pore filter to block any particles and metal dust that could be introduced in the plant.

The pressure inside of the column is kept below 5 mbar to reduce the boiling point ($<$ 200°C) and preserve LAB from thermal degradation. The system is equipped with a vacuum pump (VC) to achieve this pressure. The entire system is kept under N_2 atmosphere to avoid any oxidation and to reduce fire risk. About 2 % of the input flow is discharged from the bottom of the column into the drain tank.

Stripping

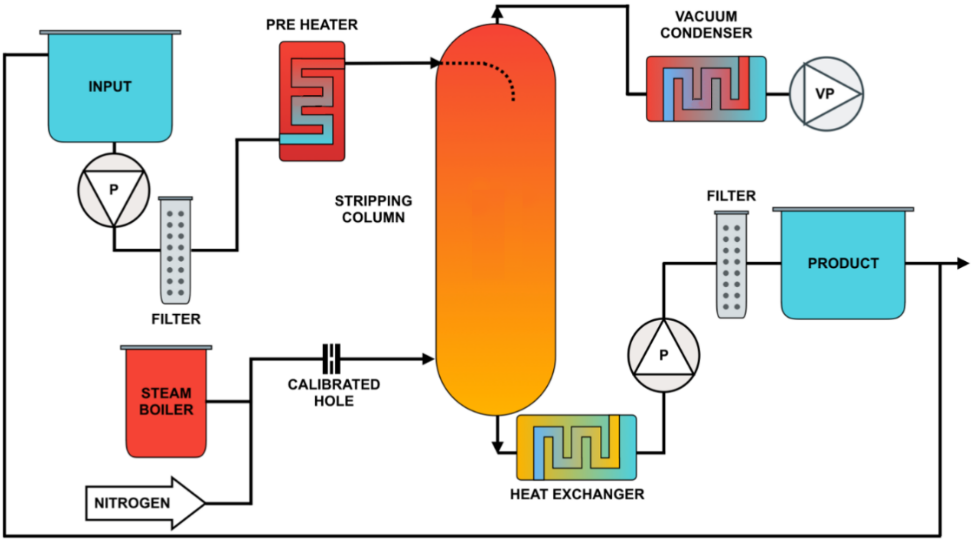

Figure 3.2: Stripping pilot plant sketch (see the text for a description)

The gas stripping is a separation process in which, one or more dissolved gases are removed from the liquid phase and transferred to the gas phase by the desorption mechanism. To remove radioactive gases such as ^{222}Rn, ^{85}Kr and ^{39}Ar as well as oxygen (that could decrease the light yield [1]) At the very last stage, liquid scintillator passes by the stripping column. The principle of operation is desorption of gaseous contaminant dissolved in liquid scintillator into the vapor steam or nitrogen flow.

The sketch of the plant is shown in Fig. 3.2. After filtratgion and preheating, scintillator stream enters in the stripping column from the top, while ultrapure vapor steam and nitrogen enter from the bottom. The column is filled with unstructured packing that forms a large contact surface between two phases. Nitrogen is purified with active carbon since its quality determines the radiopurity that can be achieved by stripping. Use of vapor steam is preferable since it has two advantages: it is much easier to produce ultrapure water than nitrogen, plus, at higher fluxes of nitrogen special ventilation system should be designed to prevent an increase of nitrogen in an experimental hall.

Absorption length

It was possible to estimate the efficiency of distillation and stripping column only after the detector is filled with liquid scintillator. However, some indications on the purity of the LAB and column efficiency could be given by spectrophotometry. In Fig. 3.3 the comparison of absorbance for raw and distilled LAB is provided. As one may see, the absorbance is reduced by a factor 4 in the range 350-450 nm. It tells about the improvement of the quality of LAB in terms of optical properties and, indirectly, radiopurity.

Moreover, spectrophotometry of a sample of liquid scintillator after stripping plant

---

[1] Though this effect was found to be not so relevant for LAB compared to pseudocumene, for example Ref. [114].

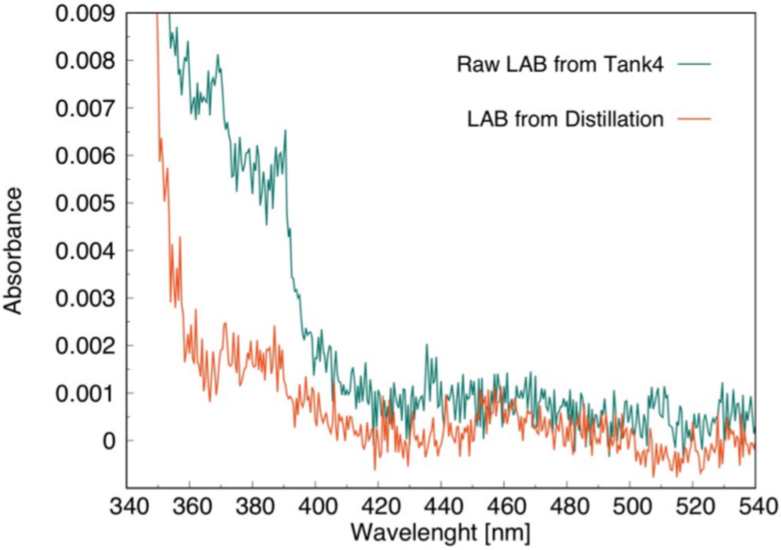

Figure 3.3: Absorption spectra of raw and distilled LAB

(not represented on the plot) showed that stripping does not degrade its optical properties.

Daya Bay detector geometry

One of the Daya Bay's detectors (called AD1) was chosen for the liquid scintillator purification test. The scheme of the detector is represented in Fig. 3.4. The target mass called Inner Acrylic Vessel (IAV) is a $r = 1.5$ m-radius and $h = 3$ m-height cylinder. It is placed inside outer acrylic vessel (OAV) with $r = 2$ m and $h = 4$ m. There are three calibration sources inside: two for IAV (ACU-A and ACU-B) and ACU-C for OAV. The calibration ACU-A source is on the central axis. ACU-A is a combined source: LED + ^{68}Ge + ^{241}Am^{13}C + ^{60}Co. ACU-A was used for detector calibrations during the operation. ACU-B source was removed in order to install an acrylic tube for refilling. At the beginning of the operation, Daya Bay LS from IAV was replaced with water (16-20 February 2017). Then (20 February - 16 March 2017) this water was replaced with 20 t of a newly purified liquid scintillator (see Fig. 6 in Ref. [112]). It passed through different stages of purification: aluminum column filtration, distillation, water extraction and, finally, stripping with nitrogen (or water vapor). After distillation and before water extraction LAB was mixed with PPO (bis-MSB) to prepare a master solution. This is the point of no return: once LAB is mixed with PPO and bis-MSB, it could not pass through the aluminum column filtration and distillation again. More information on the procedure could be found in Ref. [112] . The very first batch of the liquid scintillator consisted of pure LAB. Then PPO and bis-MSB were introduced, and the concentration of flavors was increased through several intermediate steps up to 4 g/l of PPO and 13 mg/l of bis-MSB to determine the dependence of the light yield from PPO and bis-MSB concentrations.

Since the LS solutions in IAV (JUNO LS) and OAV (Daya Bay LS) have different PPO and bis-MSB concentrations, the light yield was expected to be also different. The

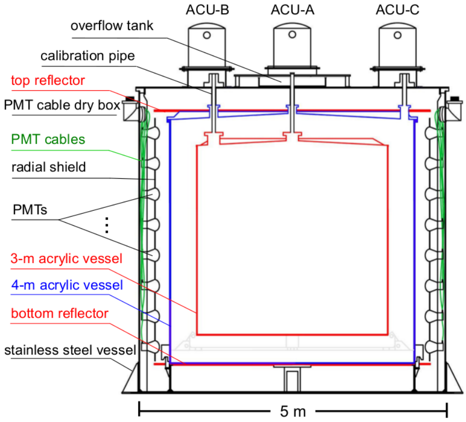

Figure 3.4: The scheme of one of the Daya Bay's detectors, AD1, used for the purification test.

starting JUNO LS with composition LAB + 0.5 g/L PPO has a light yield about 40% lower than LAB + 3 g/L PPO + 15 mg/L bis-MSB of Daya Bay LS.

Data set

The acquisition system of AD1 detector collected the data. Then it was also acquired in parralel by newly installed FADC which reduces the dead time (299 ns) of acquisition significantly. It was necessary for an efficient ^{232}Th detection since ^{212}Bi-^{212}Po has a very small time of coincidence. All essential reconstructed data was stored in a root file. The root file contained *AdEnergy* tree with variables such as reconstructed energy, vertex and trigger time (in seconds and nanoseconds). Zero of time (sec, nano sec) corresponded to 1970-01-01 00:00:00 UTC. The data was filtered from the PMT flasher events and events with energy larger than 2 MeV which were anti-neutrino candidates. The file also contained muon events. They were signed as events with energy larger than 20 MeV.

Fiducial volume

z-coordinate reconstruction had a bias: a reconstructed event with $Z = 1.0$ m corresponded to the true vertex at $Z = 1.5$ m. The bias was visible for runs with a calibration source. It was symmetrical with respect of the coordinate origin. The bias was due to lack of PMTs on the top and bottom of the detector. Instead, it was covered with a reflective coating. The bias in radial coordinate R was assumed to be small. Since the off-center calibration source ACU-B was removed, the direct observation of R-axis bias was not available. The presence of bias leads to the correction for fiducial volume.

^{222}Rn and ^{238}U analysis

Several cuts were applied on raw data to remove backgrounds and select ^{214}Bi-^{214}Po coincidence ($T_{1/2} = 164.3$ μs):

- Muon veto. Veto all events after a muon in 1 ms (Fig. 3.5)

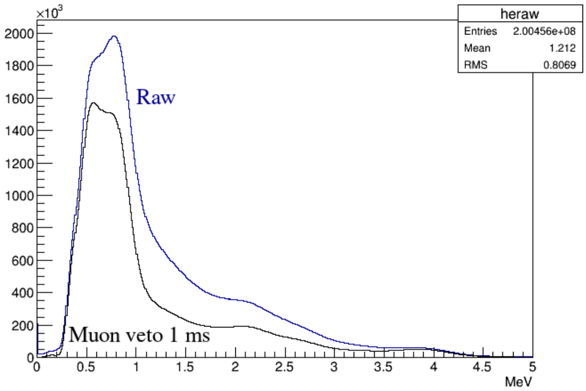

Figure 3.5: Energy spectrum with and w/o muon veto cut applied.

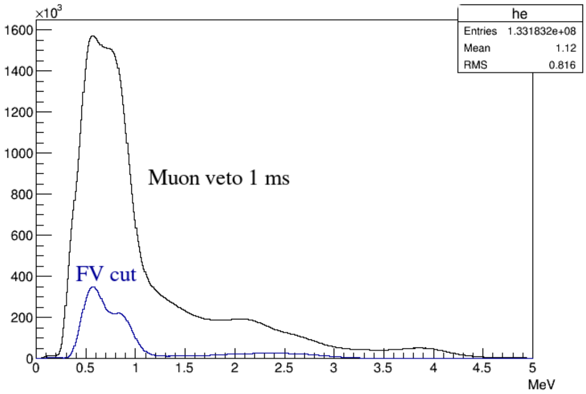

Figure 3.6: Energy spectrum with and without fiducial volume cut applied.

- Fiducial volume cut: $r < 1$ m, $|z| < 1$ m (Fig. 3.6) to reject surface and external γ background.

- Find a pair of events whose time interval is less than 500 μs (about 3 half-lives) (and more than 10 μs) and they would be candidates of β and α decays of ^{214}Bi and ^{214}Po called prompt and delayed signal (Fig.3.7)

- Energy and spatial distance cut: prompt signal $E_{\alpha}^{vis} = 0.7 - 1.1$ MeV (contraction of the energy scale from $E_{\alpha}^{true} \approx 5.5$ MeV due to quenching effect); delayed signal $E_{\beta}^{vis} = 1.5 - 3$ MeV. Both events happen in immediate proximity to each other, therefore spatial distance cut less than 1 m should be applied (Fig. 3.8 and 3.9).

The radon decay rate could be determined as:

$$rate_{decay}[\mathrm{Bq/m^3}] = N_{coin}/(FV_{true} \times \epsilon \times (t_{total} - t_{veto})) \tag{3.4}$$

where N_{coin} is the number of time coincidence events with all cuts implemented. FV_{true} is the true fiducial volume. It slightly differs from the one that we use for the

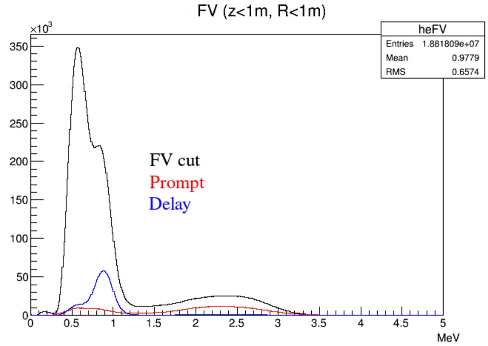

Figure 3.7: Prompt and delay events after muon and fiducial volume cuts.

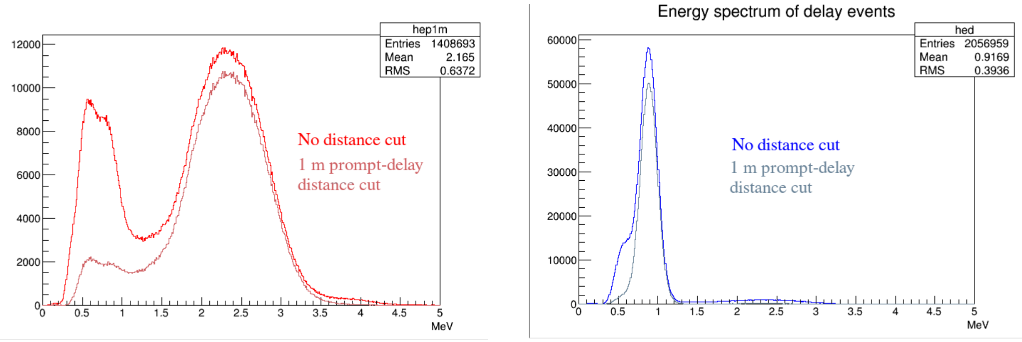

Figure 3.8: a) **Figure 3.9:** b)

Figure 3.10: Prompt β (a) and (b) delay α event spectra for ^{214}Bi $-$ ^{214}Po coincidence

cut $FV_{cut} = \pi r^2_{cut}(2z_{cut})$ due to z-axis bias; $\epsilon \approx 0.5$ is a total efficiency for all cuts (Ref. [115]) ; t_{total} is the total time of the data taking, t_{veto} is the vetoed time due to muons. Backgrounds (for example, accidental) were not considered.

Results

The fit of the plot for coincidence rate (Fig. 3.11) gives the $T^{unkown}_{1/2} = 3.747 \pm 0.075$ days. It is consistent with $T^{Rn222}_{1/2} = 3.8235 \pm 0.0003$ days for ^{222}Rn.

If ^{222}Rn is in equilibrium with ^{238}U its rate is expected to be constant. Therefore to measure ^{238}U concentration one needs to wait until the radon rate achieves a plateau.

On 25 April 2017 the radon rate became constant: 2.6 ± 0.015 coincidence per hour in fiducial volume or $(1 \pm 0.006) \times 10^{-4}$ Bq/m^3. It is possible that the constant rate is due to non-identified radon leakage or unknown background. Nitrogen flow could be a source of radon as well, but the change of nitrogen flow seems do not affect the rate. Since the ambiguity of these factors we can only set the upper limit on the ^{238}U concentration:

$$^{238}\mathrm{U} < 1 \times 10^{-14}\ \mathrm{g/g}\ 90\%\ \mathrm{C.L.} \tag{3.5}$$

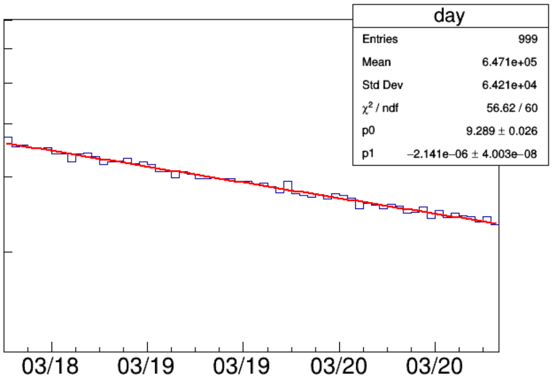

Figure 3.11: Event coincidence rate versus time in days (bin size is 1 hour)

^{232}Th analysis

The efficiency of Daya Bay DAQ system for looking ^{212}Bi $-$ ^{212}Po was very low due to very small 299 ns half-life of ^{212}Po. The installation of new FADC was necessary. The old and the new electronics (FADC, 1μs time window) shared the same trigger. They record the same event, but the old system stores integrated charge while the FADC records a whole waveform. Some cuts were made in the DAQ software to reduce the data size of the FADC dataset. Thus the FADC data is only some sample of the total data sample acquired by old DAQ. Therefore, to estimate a single trigger rate in the fiducial volume, we should use the old DAQ data. 10^{-15} g/g is the sensitivity estimated for 15 days of the data taking with the new system (Ref. [116]).

$N_{coin} = 93$ coincidence events were observed (period from Mar. 30 to Apr. 20). To estimate the rate of the ^{232}Th it was necessary to study backgrounds from accidental events, ^{222}Rn and related with vertex reconstruction. The efficiency includes the following factors: branching ratio (0.64), FADC data reduction (0.77 for $k = 0.5$), trigger time efficiency (0.46), fiducial volume cut (0.77) and prompt energy cut (0.89), giving the total efficiency:

$$\epsilon_{Th} = 0.14 \tag{3.6}$$

Since access to official Daya Bay Monte Carlo software was not available, I developed simplified Monte Carlo to estimate these efficiencies. Chinese colleagues provided several experimental parameters from Daya Bay collaboration.

Trigger and FADC

DAQ Energy Cut efficiency

To detect a coincidence for ^{232}Th, we search for two triggers in readout window of FADC. Therefore the events with only one trigger could be excluded from the acquisition; otherwise, DAQ would record a massive amount of data. Prompt events usually have higher visible energy than delay, so we can apply low-level selection criteria to reduce DAQ trigger rate: $E_{delay} > kE_{prompt}$. Monte Carlo method is used to estimate this

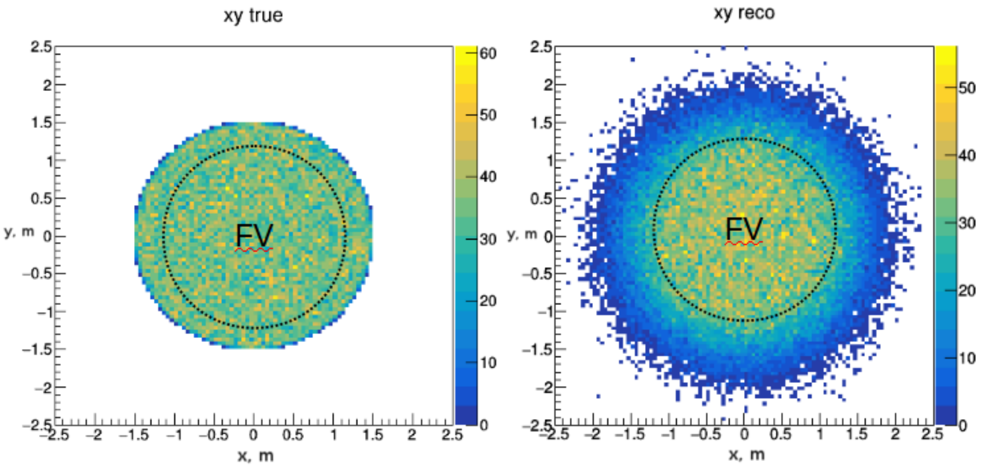

Figure 3.12: Events simulated in the inner vessel IAV: true (left) and reconstructed (right)

efficiency. It was found ($k = 0.5$) to be equal to 0.774.

Trigger time efficiency

Trigger time efficiency is related to the fact that only part of coincidence decays are inside of acquisition time window. To determine this efficiency we need to calculate the probability for delay event to be inside the time window. The optimal time window is from $t_1 = 300\,\text{ns}$ until $t_2 = 800\,\text{ns}$. Therefore the efficiency:

$$\epsilon_{trigger} = exp(-300\,\text{ns}\,ln2/299\,\text{ns}) - exp(-800\,\text{ns}\,ln2/299\,\text{ns}) = 0.342 \tag{3.7}$$

and $\epsilon_{trigger} = 0.472$ if we use $t_1 = 200\,\text{ns}$ as starting time.

Fiducial Volume efficiency

To calculate FV efficiency, we need to take into account vertex reconstruction error and events with two different topologies:

1. Event inside of FV; prompt signal inside FV, delay signal outside and vice versa.
2. Event outside of FV, but inside 3 m acrylic; Prompt and delay signals inside FV.

The reconstruction error is distributed normally with $\sigma_x = \sigma_y = \sigma_z = 0.2\,\text{m}$.

Fig. 3.12 demonstrates simulated distribution of events in the vessel and FV for true (left) and reconstructed events (right).

Calculations give $\epsilon = 0.736$ for $\sigma = 0.2\,\text{m}$ (Ref. [117]).

Backgrounds

Mainly three sources of background could be identified:

- Accidental that consists of random coincidence of the events inside the FV and could be found with the formula

$$N_{acc}^{bkg} = f_{FV}^2 \Delta t_{window} T_{live} / (\epsilon_{energycut}\ \epsilon_{DAQ}) \tag{3.8}$$

where f_{FV} is the total event rate inside of the fiducial volume.

Estimated number of accidental background events in FV is $N_{accidental}^{bg} = 34$.

- Radon decay in FV could also give coincidence and mimic the signal $N_{Rn}^{bg} = 20$.
- Events from OAV (4 m acrylic) which are reconstructed inside the FV due to limited spatial resolution. Daya Bay LS has a higher concentration of ^{232}Th with respect to JUNO requirements: $^{232}\text{Th}_{OAV} \approx 10^{-14}$g/g (Fig. 3.13). Due to poor vertex resolution some prompt and some delay signals in Daya Bay LS are reconstructed inside of fiducial volume (Fig. 3.14). The event is treated as a background if and only if both the prompt and delay signals are reconstructed inside the FV (Fig. 3.15). Fiducial volume: $R = 1.2\ m$, $z = 3$ m. For concentration $^{232}\text{Th}_{OAV} \approx 10^{-14}$ g/g and vertex resolution $\sigma_{x,y,z} = 0.2$ m 8 events were found.

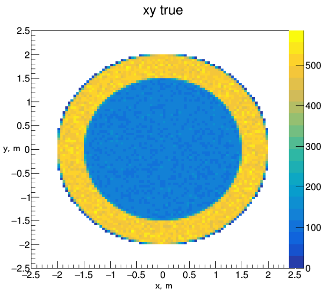

Figure 3.13: Events generated in Daya Bay scintillator in OAV

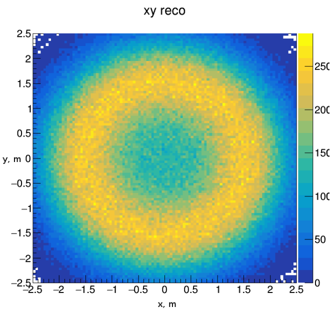

Figure 3.14: Reconstructed events

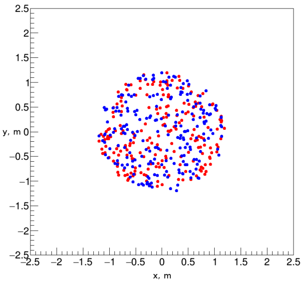

Figure 3.15: Events when both prompt and delay are reconstructed inside IAV

Results

Efficiencies and backgrounds for ^{232}Th rate were explicitly studied.

$N_{coin} = 93$ events were observed in coincidence in the analysis period. Among them 90 events of background: 34 accidental events, 20 radon events, and 8 events from $^{232}\text{Th}_{OAV}$ ($\sigma_{x,y,z} = 0.2$, OAV Daya Bay LS, $^{232}\text{Th}_{OAV} = 10^{-14}$g/g). Since backgrounds limit the sensitivity of our method: $signal{+}background \approx background$, we can only put the upper limit:

$$^{232}\text{Th} < 2.8\ 10^{-15}\text{g/g}\ \ 90\%\ \text{C.L.} \tag{3.9}$$

Conclusions

To fulfill JUNO crucial requirements for liquid scintillator radiopurity and transparency, the development and testing of the purification system are of great importance. Before full-scale implementation, it was decided to build a prototype of purification system which consists of four pilot plants for alumina oxide filtration, distillation, water extraction and gas stripping. Close investigation of the efficiency of two techniques, distillation and stripping, was provided in this chapter.

The very first indications on the purity of the LAB and column efficiency was given on-site by spectrophotometry. Comparison of absorbance for raw and distilled LAB had shown factor 4 reduction in the range 350-450 nm. It is direct evidence of the capability of distillation to improve optical properties and indirect indication of radiopurity improvement. Spectrophotometry of a liquid scintillator sample after stripping plant, the very last stage of purification, showed that it does not degrade its optical properties.

The main challenge of the radiopurity analysis presented in this chapter was a lack of the official Monte Carlo simulation program of the detector which is available only to members of Daya Bay collaboration. Nevertheless, it was possible to obtain a measurement for ^{222}Rn and limits for ^{238}U and ^{232}Th which were strategically valuable for purification campaign.

The radon rate at the plateau, associated with ^{238}U chain secular equilibrium was found to be quite high. However, it could be induced by uncounted background, therefore only the upper limit could be set:

$$^{238}\mathrm{U} < 1.0\,10^{-14}\mathrm{g/g}\;\; 90\%\,\mathrm{C.L.}$$

The result for ^{232}Th suggests that radiopurity of the scintillator with respect to this element is close to the nominal requirements for reactor neutrino program (3.1):

$$^{232}\mathrm{Th} < 2.8\,10^{-15}\mathrm{g/g}\;\; 90\%\,\mathrm{C.L.}$$

The presence of ^{222}Rn in the liquid scintillator at the first stage of filling indicated on some leakages presented in the system and suggested technological improvement of distributing line. After this improvement the amount of radon was further reduced and fine measurements $^{238}\mathrm{U} = 7.52 \pm 1.41\,\mathrm{(stat)} \pm 0.37\,\mathrm{(sys)}\,10^{-15}\mathrm{g/g}$ and $^{232}\mathrm{Th} = 3.2 \pm 1.0\,\mathrm{(stat)} \pm 0.66\,\mathrm{(sys)}\,10^{-15}\mathrm{g/g}$ were obtained by Zeyuan Yu and others (Ref. [118]). The limits presented in this chapter are in agreement with this result.

The main conclusion that could be derived is that so far the purification results do not fulfill JUNO requirements and further effort should be made for improvement.

CHAPTER 4

Study of the Non-Standard Interactions with large liquid scintillator detectors

Constraining NSI's with Borexino Phase II

Within the last few decades, the study of solar neutrinos has become relevant not only for probing our understanding of the Sun but also for investigating and determining intrinsic neutrino properties. Solar neutrino experiments, primarily SNO [49] and Super-Kamiokande [119], together with KamLAND [50, 120, 121], have resolved the solar neutrino problem with the large mixing angle (LMA) MSW effect [46, 122, 123, 124]. Further improvements of experimental precision may reveal the effects of physics beyond the Standard Model such as sterile neutrinos, Dark Matter, and other non-standard interactions of the neutrino [125, 126, 127, 128]. In this article, we will see how far the latest achievements of Borexino in solar neutrino detection and the advances in the modeling of the Sun will take us in our search for such small sub-leading effects.

The Borexino experiment at the Laboratori Nazionali del Gran Sasso (LNGS) [129] detects solar neutrinos through the neutrino-electron elastic scattering interaction on a $\sim$280 ton liquid scintillator target. During the Phase-I data taking period (May 16, 2007–May 8, 2010) Borexino had 740.7 live days of data taking, corresponding to 153.6 ton·years of fiducial exposure [130, 100]. Following Phase-I, an extensive scintillator purification campaign was conducted resulting in significant reductions of radioactive contaminants. Uranium-238 and Thorium-232 levels were reduced to ^{238}U $< 9.4\times10^{-20}$ g/g (95 % C.L.) and ^{232}Th $< 5.7 \times 10^{-19}$ g/g (95 % C.L.). ^{85}Kr and ^{210}Bi concentrations were reduced by factors ~ 4.6 and ~ 2.3, respectively [55]. The Phase-II data, analyzed in this paper, were collected from December 14, 2011 until May 21, 2016, corresponding to 1291.51 days × 71.3 t (252.1 ton·years) of fiducial exposure. Reduction of the background, longer exposure, and better understanding of the detector response allowed for fits to be performed in a wider energy range ($0.19\,\mathrm{MeV} < T < 2.93\,\mathrm{MeV}$, where T is the recoil-electron kinetic energy) to include pp, ^{7}Be, pep and CNO electron-recoil spectra [6]. Taking advantage of this improvement, this paper uses the Phase-II data to place constraints on the parameters of non-standard interactions (NSI's) of the neutrino.

Solar neutrinos can be used as a probe for new physics beyond the SM that affect neutrino interactions with the charged leptons and quarks. In this paper, we restrict our analysis to the neutrino-flavor-diagonal NSI's that affect $\nu_e e$ and $\nu_\tau e$ interactions since Borexino is particularly sensitive to this set. We do not consider NSI's that affect the $\nu_\mu e$ interaction since those had already been strongly constrained by the $\nu_\mu e$ scattering experiment CHARM II [70].

Using Borexino for constraining NSI's was originally discussed by Berezhiani, Raghavan, and Rossi in Refs. [64, 24]. There, it was argued that the monochromatic nature of the ^{7}Be solar neutrinos results in an electron recoil spectrum whose shape is more sensitive to the νe couplings than that from a continuous neutrino energy spectrum. Following Refs. [64, 24], a purely phenomenological analysis based on Borexino Phase-I data [131] was carried out in Ref. [25], in which the roles of the main backgrounds were analyzed and bounds on $\nu_e e$ and $\nu_\tau e$ NSI's were reported. However, the analysis considered the effects of the NSI's at detection only. High solar metallicity (HZ) was also assumed as input to the Standard Solar Model (SSM) [71, 132, 133, 5] to predict ^{7}Be-solar neutrino flux.

This paper updates and improves upon the analysis of Ref. [25] by the direct use of Phase-II data with the full arsenal of tools of the Borexino collaboration developed so far. NSI effects are included in both propagation and detection. At production the NSI's affect the solar-neutrino spectrum only below the Borexino threshold of $\sim$ 50 keV [6, 69]. To account for the effect of solar metallicity, analyses are performed for both high- (HZ) and low-metallicity (LZ) assumptions.

Phenomenological analysis

Analysis description

In this section, I reproduce the results of this article and perform a similar analysis for Phase II of the Borexino's data. For this purpose, I wrote a C++ program to generate experimental data and perform fitting. Being a very simplified representation of the experiment, it defines the leading strategy and may serve as a guideline for the real data inquiry.

In the Phase I The principal backgrounds for the analysis were (in cpd/100 ton):

$$^{85}\text{Kr} = 31.2 \pm 1.7\,\text{(stat)} \pm 4.7\,\text{(syst)} \tag{4.1}$$

$$^{210}\text{Bi} = 41.5 \pm 1.5\,\text{(stat)} \pm 2.3\,\text{(syst)} \tag{4.2}$$

For the Phase II the backgrounds are significantly lower (in cpd/100 ton):

$$^{85}\text{Kr} = 6.8 \pm 1.8\,\text{(stat)} \tag{4.3}$$

$$^{210}\text{Bi} = 17.5 \pm 1.9\text{(stat)} \tag{4.4}$$

Lower backgrounds suggest a better sensitivity to NSI for the Phase II compared to the Phase I.

All following section is related to Phase II, and at the end of the section, a comparison between the two phases is provided.

The idea of the analysis is to generate the simplified dataset that include only one ^7Be spectrum and two background spectra: ^{85}Kr and ^{210}Bi. They should be the most relevant in the energy window $0.3 - 0.8$ MeV. ^{7}Be spectral shape deformation and normalization may correlate with the backgrounds, diminishing the limits on NSI. The peak of ^{210}Po was assumed to be removed from the spectrum with $\alpha - \beta$ discrimination.

The Phase II generated dataset consists of about 250 years × ton (December 2011 - May 2016). No NSI interactions assumed for data generation. The generated data was represented in the histogram with a bin size 10 keV. The energy response of the detector was modeled with a very simple Gaussian smearing: $\sigma_T/T = 5\%/\sqrt{T[\text{MeV}]}$. The detector efficiency is supposed to be 100 % in the energy range of the analysis. Maximal mixing scenario was chosen with $\theta_{23} = \pi/4$.

Generated data was fitted with a theoretical model that includes NSI using a χ^2 minimization. The resulting dependence of the χ^2 from the NSI parameters puts the bounds on them: the bounds could be obtained with χ^2-profile. With a simplified statistical approach 90 % C.L. level corresponds to $\Delta\chi^2 = 2.71$. Though, strictly speaking, this approach is valid only if the profile is parabolic. The full scan of the ε-space is quite problematic, so usually one- or two-dimensional projections on the subspace are considered (for example, χ^2 versus $\varepsilon_{\alpha R}$ or χ^2 versus $\varepsilon_{\alpha R}$ - $\varepsilon_{\alpha L}$ plane), which are also convenient for the comparison with results of other experiments.

With our knowledge of the solar neutrino fluxes we can fix the $j_{^7Be}$-flux with SSM prediction. To do this the penalty term with mean value and uncertainty of the prediction should be added in the χ^2. One can realize the profit which $j_{^7\text{Be}}$-flux penalty can gain, keeping in mind the relation $N^{obs}_{^7\text{Be}} \propto \sigma(\varepsilon_{\alpha L}) \times j_{^7\text{Be}}$. $\varepsilon_{\alpha L}$ changes mostly the total cross section and not the spectral shape. Therefore, the χ^2 expression for minimization consists of two parts:

Table 4.1: 90 % C.L. limits on the NSI parameters. Comparison of the Phase I and Phase II data with constraints. Bold font is to underline the power of the Kr-constraint.

$Phase$	I	II	II	II
$Kr - penalty$	yes	no	yes	no
$Bi - penalty$	no	no	no	yes
ε_e^R	[-0.196, 0.139]	[-0.170, 0.135]	**[-0.105, 0.084]**	[-0.170, 0.135]
ε_e^L	[-0.043, 0.051]	[-0.038, 0.043]	[-0.038, 0.043]	[-0.038, 0.043]
ε_τ^R	[-0.844, 0.598]	[-0.850, 0.601]	**[-0.656, 0.404]**	[-0.850, 0.599]
ε_τ^L	[-0.224, 0.856]	[-0.197, 0.829]	[-0.195, 0.819]	[-0.196, 0.828]

$$\chi^2 = \chi^2_{fit} + \chi^2_{SSM\ penalty} = \sum_i \frac{(N_{exp} - N_{model}(\varepsilon))^2}{N_{exp}} + \frac{(j^{SSM}_{^7Be} - j^{exp}_{^7Be})^2}{(\sigma^{SSM}_{^7Be})^2}$$

The normalization is performed for the full spectral range to make the rates independent from the threshold of the detector, even if the analysis range includes only some part of the spectrum. It means that the rate obtained from the fit differs from the rate of the triggered events if the analysis range does not contain an entire spectrum. The fit provides us the normalization factors that could be directly converted in the experimental rates in cpd/100ton.

The amount of Kr could be independently measured by coincidence technique with reactions (4.11) discussed later. Based on this information a Kr-penalty term

$$\chi^2_{\mathrm{Kr}} = \frac{(N^{exp,fit}_{Kr} - N^{exp,coin}_{Kr})^2}{(\sigma^{coin}_{Kr})^2}$$

could be introduced into χ^2 to increase sensitivity. To study the importance of the Kr-penalty the uncertainty 18 % was used (the same as for Phase I data).

Strictly speaking it is not correct uncertainty, since Phase II has another limit for Kr from coincidence measurement: upper limit < 7.5 cpd/100 ton. Hence the result with 18 % - penalty should be treated as illustrative intermediate step. The further analysis with the data reveals the role of the Kr in detail.

10 % Bi-penalty was also tested, though as we will see from correlation analysis in Appendix, it is weakly correlated with ^{7}Be and has no influence.

One dimensional χ^2 profiles

The results are represented as χ^2-profiles for the NSI parameters in Fig. 4.1. While one parameter changes all others are fixed to zero. It reproduces the result for Phase I phenomenological analysis (Kr-penalty applied) as well as predict the result for Phase II with and without Kr-constraint.

The statistical analysis was conducted in a simplified way. $\Delta\chi^2$ corresponds to 90 % C.L. even if the shape of the profile was *not* parabolic. The corresponding limits are represented in Table 4.1. The results for 10 % Bi-constraint are also presented, but not shown on the plots.

The analysis showed that even without applying Kr-constraint the bounds with Phase II data are better than Phase I bounds even with Kr-constraint applied. The bounds for ε_e^R and ε_τ^R are improved due to reduced background; ε_e^L and ε_τ^L bounds are better due to

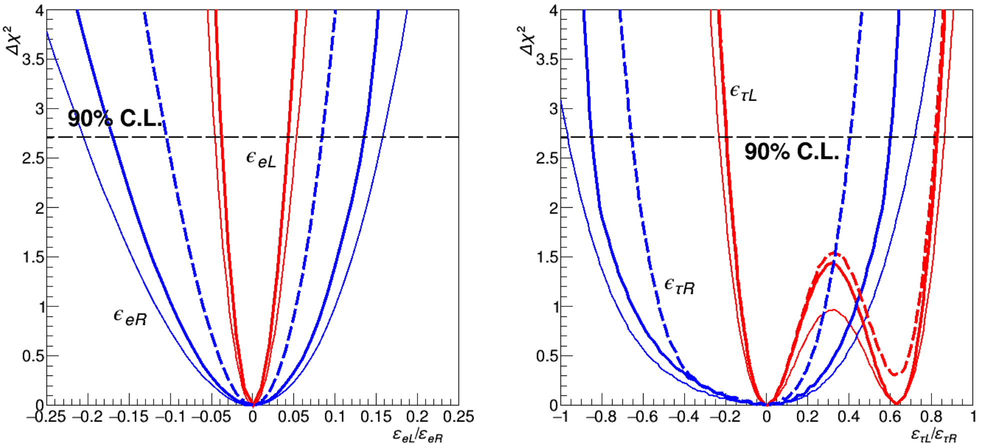

Figure 4.1: χ^2-profiles for $\varepsilon_e^{L/R}$ (left) and $\varepsilon_\tau^{L/R}$ (right). Thin solid line - Phase I w/ Kr-constraint, thick solid line - Phase II w/o Kr constraint, dashed line - Phase II with 18 % Kr-constraint.

smaller uncertainty of SSM ^{7}Be flux. Kr-constraint significantly improves the result for the right constants but does not influence the left ones.

In Fig. 4.1 (right) one may notice the presence of two local minima for ε_τ^L at 0.0 and 0.64. It means that there is a combination of the backgrounds together with NSI-modified electron recoil spectrum that also describes very well the data even if NSI parameter ε_τ^L is quite large. It is worth to notice that in the presence of the Kr-constraint to make the minimum at 0.0 slightly more preferable than 0.64.

The same analysis model could be applied for $\sin^2\theta_W$ measurement in low energy region with Borexino data, if one supposes the modification of all NSI parameters at the same time. The precision of this measurement is quite modest to test $\overline{\text{MS}}$ renormalization scheme being $\sim 10\%$: the error should be at least 10 times improved (see Fig. 1 from Ref. [134]).

Two dimensional χ^2 profiles

The contours in two-dimensional left-right space are much more informative. In Fig. 4.2 and 4.3 the comparison of Phase I with Kr-penalty (red line) and Phase II without Kr-penalty (green line) for $\varepsilon_e^{L/R}$ and $\varepsilon_\tau^{L/R}$ is shown. Also, the contour for Phase II with 18 % Kr-constraint is provided, which is, strictly speaking, not correct since the independent measurement for Kr in Phase II is different. Though it is a convenient choice for a comparison of two Phases since it was used for Phase I analysis. The contour 95 % C.L. (2 d.o.f.) corresponds to $\Delta\chi^2 = 5.99$.

Running ahead, let us note that insensitivity in a diagonal direction and, in particular, in the fourth quadrant of $\varepsilon_e^R - \varepsilon_e^L$ plot in Fig. 4.2 is due to correlation between ^{7}Be and ^{85}Kr spectra. This question will be investigated further, in real data analysis. Note that fixing Kr rate with a constraint reduces significantly the allowed region with a tendency to split it into two contours (blue dashed contour).

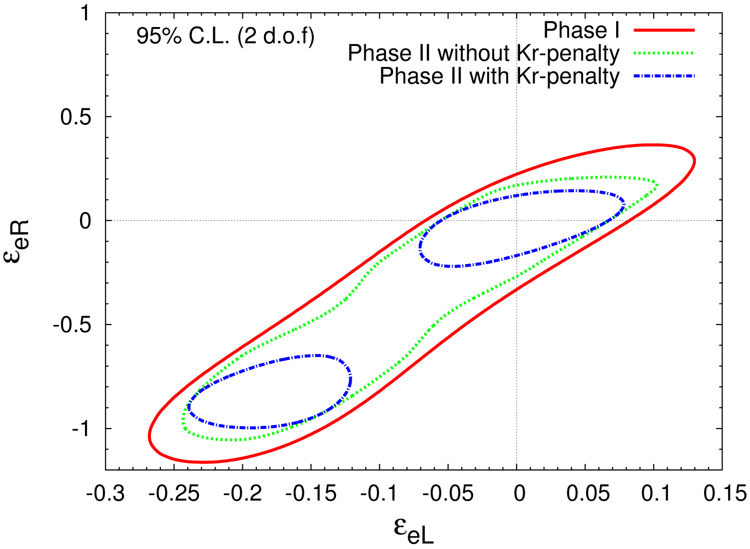

Figure 4.2: The bounds in $\varepsilon_e^{L/R}$ plane.

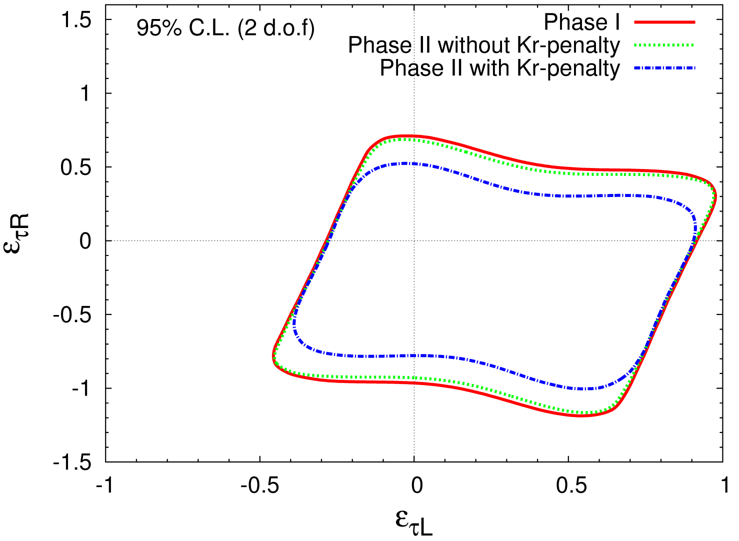

Figure 4.3: The bounds in $\varepsilon_\tau^{L/R}$ plane.

Analysis of Phase II Borexino data

Overview

The objective of this analysis is to set bounds on the NSI parameters $\varepsilon_e^{L/R}$ and $\varepsilon_\tau^{L/R}$. In contrast to the analysis of Ref. [6], in which the νe couplings were fixed to those of the SM and the count rates of pp, ${}^7\mathrm{Be}$, and pep neutrinos were fit to the data, we allow the couplings to float, assuming SSM neutrino fluxes at the source based on either the HZ- or LZ-SSM assumptions.

We have argued in the previous section that $\varepsilon_e^{L/R}$ and $\varepsilon_\tau^{L/R}$ affect neutrino propagation and detection: propagation through a shift in the matter-effect potential $V(x)$, leading to a modification in the expected ν_e survival probability $P_{ee}(E)$, and detection through shifts in the effective chiral coupling constants, leading to modifications in the electron recoil spectra $d\sigma_\alpha/dT$ ($\alpha = e, \tau$), Eq. (4.50).

Four solar neutrino components are considered in this analysis: pp, ${}^7\mathrm{Be}$, pep, and CNO.[1] The SSM [71, 132, 133, 5] predicts the respective energy spectra of these neutrinos, which we denote as $d\lambda_\nu/dE$, where the subscript ν labels the neutrino component.

The ${}^7\mathrm{Be}$-component plays a fundamental role in the analysis. Both the shape and the normalization of the electron-recoil spectrum is well-constrained in the fit. Together with the 6%-uncertainty in the ${}^7\mathrm{Be}$ neutrino flux, it provides the highest sensitivity to NSI's among all the neutrino components.

We do not consider ${}^8\mathrm{B}$ neutrinos for placing the bounds on NSI's. The rate of ${}^8\mathrm{B}$ neutrino events cannot be determined with the spectral fit: it is quite small and completely hidden by backgrounds in the energy region of the present analysis. Moreover, the relatively large 12%-uncertainty on the ${}^8\mathrm{B}$ neutrino flux predicted by SSM limits the utility of ${}^8\mathrm{B}$ in our approach.

Taking into account the oscillation of ν_e into ν_μ and ν_τ, the recoil spectrum for each solar neutrino component is given by

$$\frac{dR_\nu}{dT} = N_e \Phi_\nu \int dE\, \frac{d\lambda_\nu}{dE} \left[\frac{d\sigma_e}{dT} P_{ee}(E) + \left(c_{23}^2 \frac{d\sigma_\mu}{dT} + s_{23}^2 \frac{d\sigma_\tau}{dT} \right) (1 - P_{ee}(E)) \right] . \qquad (4.5)$$

Here, N_e is the number of electrons in the fiducial volume of the detector, and $s_{23}^2 \equiv \sin^2\theta_{23}$, $c_{23}^2 \equiv \cos^2\theta_{23}$. Φ_ν is the expected total flux of solar neutrino component ν at the Earth when neither oscillations nor NSI's are assumed, and $d\lambda_\nu/dE$ is a corresponding neutrino energy spectrum. $P_{ee}(E)$ is the solar-ν_e survival probability, into which NSI effects at propagation have been added. The effect of the NSI's at detection is included in the differential cross sections $d\sigma_e/dT$ and $d\sigma_\tau/dT$; $\varepsilon_e^{L/R}$ and $\varepsilon_\tau^{L/R}$ parameters are always combined in the recoil spectrum (4.53).

The dependence of the ${}^7\mathrm{Be}$ electron recoil spectrum dR_{Be7}/dT on the NSI's for several values of ε_e^R and ε_e^L is illustrated in Figure 4.4. Note that ε_e^L mostly modifies the normalization of the spectrum while ε_e^R modifies its slope. ε_τ^L and ε_τ^R require much larger magnitudes to achieve the same effects due to the smaller contribution of ν_τ to dR_{Be7}/dT.

Integrating Eq. (4.53), one obtains a relation between the total experimental event

---

[1] The direct detection of CNO neutrinos is yet to be achieved and is one of the remaining goals of Borexino. In the present analysis we look for deviations from the SSM + LMA-MSW predictions, so the CNO neutrino flux, together with the other three component fluxes, are simply fixed to those predicted by either the HZ- or LZ-SSM.

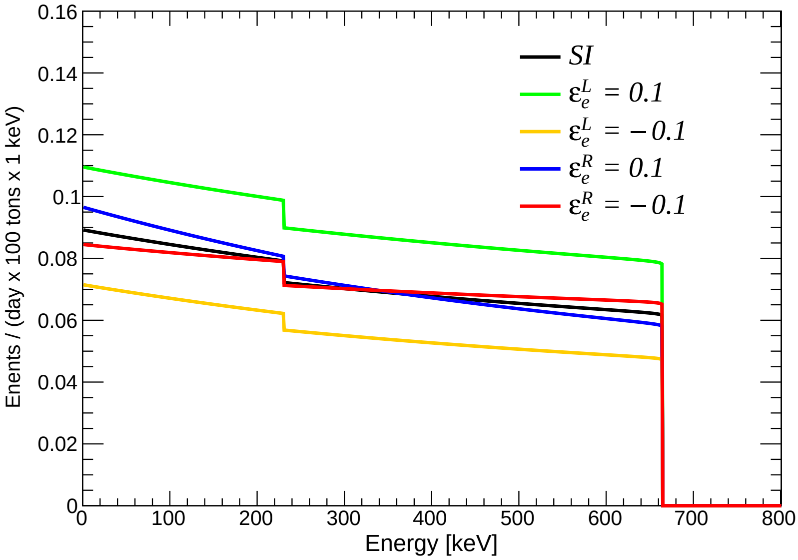

Figure 4.4: The distortion of the electron recoil spectrum, Eq. (4.53), for the two monochromatic ^{7}Be neutrino lines ($E_\nu = 0.384\,\mathrm{MeV}$ and $0.862\,\mathrm{MeV}$) due to non-zero values of ε_e^L and ε_e^R. The effect of limited energy resolution of the detector is not shown.

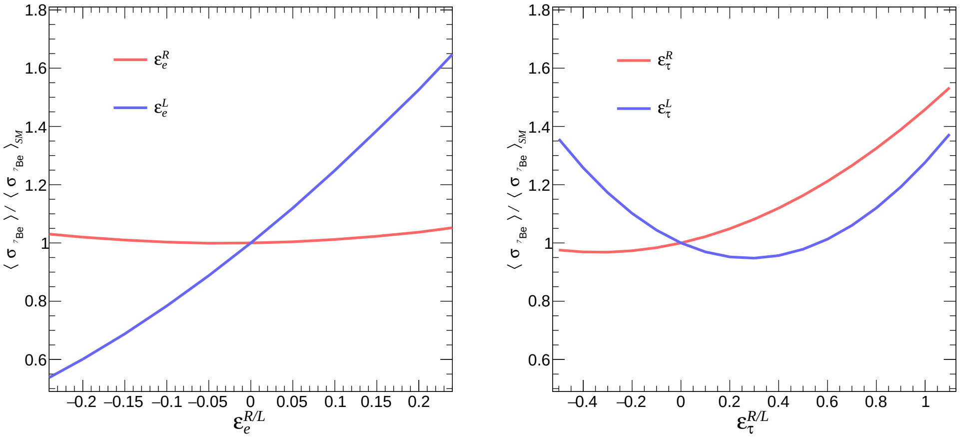

Figure 4.5: The relative change of the total cross section ratio $\langle\sigma_{^7\mathrm{Be}}\rangle/\langle\sigma_{^7\mathrm{Be}}\rangle_{\mathrm{SM}}$ as function of ε_e^R / ε_e^L (left panel) and ε_τ^R / ε_τ^L (right panel).

rate R_ν, solar neutrino flux Φ_ν, and the total cross section $\langle\sigma_\nu\rangle$:

$$R_\nu \;=\; \int \frac{dR_\nu}{dT}\,dT \;=\; N_e \Phi_\nu \langle\sigma_\nu\rangle\;. \tag{4.6}$$

NSI effects at propagation and detection are both included in the total cross section $\langle\sigma_\nu\rangle$. Denoting the total cross section in the absence of NSI's as $\langle\sigma_\nu\rangle_{\rm SM}$, we plot the change in the ratio $\langle\sigma_\nu\rangle/\langle\sigma_\nu\rangle_{\rm SM}$ for the ^{7}Be neutrinos due to the presence of ε_e^L and ε_e^R in Figure 4.5. Again, we see that ε_e^L affects the normalization of the cross section while ε_e^R does not. Thus ε_e^L is mostly constrained by the normalization of the cross section, while ε_e^R is mostly constrained by the shape of the recoil spectrum.

Detector Model and Parameter Choices

We performed the selection of the events according to Ref. [6], using a spherical fiducial volume with top and bottom parts truncated: $R < 2.8\,\mathrm{m}$, and the vertical coordinates $-1.8\,\mathrm{m} < z < 2.2\,\mathrm{m}$. To model the detector response, we use the analytical model of the Borexino detector discussed in detail in Ref. [55]. The model uses the number of triggered PMT's, $N_p^{dt_1}$, within the fixed time interval of $dt_1 = 230\,\mathrm{ns}$ as the estimator of the electron recoil energy T. Various model parameters have been fixed utilizing independent measurements, or tuned using the Borexino Monte Carlo, while some have been left free to float in the fit. The floating parameters include (i) the light yield which determines the energy scale, (ii) two parameters for resolution, (iii) two for the position and width of the ^{210}Po-α peak, and (iv) one for the starting point of the ^{11}C β^+-spectrum. The detector response function convoluted with the cross sections dR_ν/dT provides the functional form to be fit to the data.

The neutrino oscillation parameters are fixed to the central values of the global fit to all oscillation data given in Ref. [135].[2] For the $\varepsilon_e^{L/R}$ analysis, we only need

$$\delta m^2_{21} \;=\; m_2^2 - m_1^2 \;=\; 7.50^{+0.19}_{-0.17}\times 10^{-5}\,\mathrm{eV}^2\;, \tag{4.7}$$

$$\sin^2\theta_{12} \;=\; 0.306^{+0.012}_{-0.012}\;, \tag{4.8}$$

and

$$\sin^2\theta_{13} \;=\; 0.02166^{+0.00077}_{-0.00077}\;, \tag{4.9}$$

which are valid for any neutrino mass-hierarchy ordering. The survival probability $P_{ee}(E)$ is calculated with these inputs using the formalism of Ref. [60]. Note that for the $\varepsilon_e^{L/R}$ analysis $d\sigma_\mu/dT = d\sigma_\tau/dT$ when $\varepsilon_\tau^{L/R} = 0$, and Borexino is insensitive to the value of θ_{23}.

For the $\varepsilon_\tau^{L/R}$ analysis we also need to specify θ_{23}. The 1σ ranges given in Ref. [135] for Normal and Inverted Hierarchies are

$$\sin^2\theta_{23} \;=\; \begin{cases} 0.441^{+0.027}_{-0.021} & \text{NH} \\ 0.587^{+0.020}_{-0.024} & \text{IH} \end{cases} \tag{4.10}$$

It is easy to see that $\sin^2\theta_{23}$ is included linearly in expression (4.53), and the sensitivity to $\varepsilon_\tau^{L/R}$ is proportional to its value. To obtain a conservative limit, we fix $\sin^2\theta_{23}$ to the NH

---

[2] Strictly speaking, to use the Borexino data to constrain possible new physics effects we should not be comparing the data to the global average of Ref. [135], which includes both Borexino Phase-I and Phase-II data in its fit. However, the numerical difference from the global average of Ref. [136], which includes neither Borexino Phase I nor Phase II, is quite small and does not affect the present analysis.

value and propagate its uncertainty into systematic error together with other oscillation parameters.

Backgrounds

Radioactive contaminants lead to backgrounds that must be clearly understood to extract unambiguous conclusions from the Borexino data. The most recent fit of signal+background to the observed electron recoil spectrum can be found in Ref. [6], where the SM couplings were assumed and the event rates of the three neutrino components (pp, $^7\mathrm{Be}$ and pep) were allowed to float. An example fit to the experimental spectrum is shown in Figure 1.13. Full description of the Borexino spectral components and backgrounds can be found in Ref. [91]. Here, we focus on components which are the most relevant for the current analysis:

- At low-energies the β-emitter ^{14}C with $Q = 156$ keV is the main background for observing the pp neutrinos ($T_{\max} = 261$ keV).

  The ^{14}C contribution is constrained in the fit with an independent measurement by selection of events with low energy threshold. Since the rate of ^{14}C is high compared to the other components, pile-up events should be taken into account. The detailed procedures can be found in Ref. [100].

- The decays from ^{85}Kr (β^-, $Q = 687$ keV), ^{210}Bi (β^-, $Q = 1160$ keV) and ^{210}Po (α, $E = 5.3$ MeV) are the main backgrounds for the electron recoil spectra from the two mono-energetic neutrino lines $E_\nu = 384$ keV and $E_\nu = 862$ keV due to ^{7}Be electron capture.

  The ^{210}Po α-decay peak is located at low energies due to the ionization quenching effect in the liquid scintillator. Even though the polonium peak is very intense with respect to the other spectral components, its shape is very distinct and easily separable in the fit and therefore does not play a dominant role. No $\alpha{-}\beta$-discrimination [91] was applied to the experimental spectrum for polonium removal.

  The β spectra of ^{210}Bi and ^{85}Kr overlap with the ^{7}Be electron-recoil spectrum leading to a modification of its shape. This reduces the sensitivity to the right-handed NSI parameter ε_α^R. The background from ^{85}Kr is quite serious since the shape of its β-spectrum and its end-point are quite close to the step-like spectrum of ^{7}Be. Therefore, one may conclude that this is one of the main factors that determine the sensitivity of the detector to ^{7}Be neutrinos. ^{210}Bi and ^{85}Kr are also ones of the most critical backgrounds for pep and CNO neutrinos.

  In principle, this background could be constrained using an independent measurement though the coincidence reaction:

$$\begin{aligned} {}^{85}\mathrm{Kr} &\longrightarrow {}^{85m}\mathrm{Rb} + e^- + \bar{\nu}_e && (Q = 0.173\,\mathrm{MeV}), \\ {}^{85m}\mathrm{Rb} &\longrightarrow {}^{85}\mathrm{Rb} + \gamma && (Q = 0.514\,\mathrm{MeV},\ t^{1/2} = 10^{-6}\ \mathrm{s}). \end{aligned} \tag{4.11}$$

  However, these decays only occur with a tiny branching fraction: 0.43%. Moreover, the prompt signal, being very close to the detector threshold, has a small detection efficiency and could be easily mimicked by ^{14}C with similar Q-value. These factors made the detection of the coincidence quite problematic. It remains difficult to obtain a reliable estimate of the ^{85}Kr-concentration, and so far the only upper limit was set.

- Other backgrounds, necessary to the fit of the experimental spectrum, are cosmogenic ^{11}C, and external γ's from ^{208}Tl, ^{214}Bi and ^{40}K.

Fit Procedure

The fitting procedure consists of the multivariate maximization of the composite likelihood function $\mathcal{L}(\varepsilon, \vec{\theta}\,)$, specifically developed to be able to detect *pep* and CNO neutrinos hidden by the cosmogenic ^{11}C background:

$$\mathcal{L}(\varepsilon,\vec{\theta}\,) \;=\; \mathcal{L}^{TFC}_{sub}(\varepsilon,\vec{\theta}\,)\cdot\mathcal{L}^{TFC}_{tag}(\varepsilon,\vec{\theta}\,)\cdot\mathcal{L}_{PS-\mathcal{L}_{PR}}(\vec{\theta}\,)\cdot\mathcal{L}_{Rad}(\vec{\theta}\,). \tag{4.12}$$

Here, ε is the NSI parameter we would like to constrain, and the vector $\vec{\theta}$ collectively represents all the other model parameters of the fit, including the fluxes of the four solar neutrino components, the intensities of the backgrounds, detector response parameters, etc.

In order to deal with ^{11}C background, the dataset was divided into two parts by Three-Fold Coincidence technique (Refs. [130, 55]). The division is based on the probability for an event to be ^{11}C. It results in ^{11}C-depleted (TFC-subtracted) and ^{11}C-enriched (TFC-tagged) data samples. The first and the second factors of Eq. (4.12) represent two separate likelihoods for TFC-subtracted and TFC-tagged experimental spectra. They are a standard Poisson likelihood:

$$\mathcal{L}^{TFC}_{sub,\,tag}(\varepsilon,\vec{\theta}) = \prod_{i=1}^{N_E}\frac{\lambda_i(\varepsilon,\vec{\theta})^{k_i}\,e^{-\lambda_i(\varepsilon,\vec{\theta})}}{k_i!} \tag{4.13}$$

where N_E is the number of energy bins, $\lambda_i(\varepsilon,\vec{\theta})$ is the expected number of events in the i-th bin for a given set of parameters ε and $\vec{\theta}$, and k_i is the measured number of events in the i-th bin.

The residual β^+ events from ^{11}C can be discriminated by the algorithm incorporated into $\mathcal{L}_{PS-\mathcal{L}_{PR}}(\vec{\theta})$. To account for external backgrounds which penetrate into the fiducial volume, the fit of the spatial radial distribution of events is incorporated by $\mathcal{L}_{Rad}(\vec{\theta})$. The more detailed description of the likelihood function and the fitting procedure can be found in Section XXI of Ref. [91], and in Ref. [55].

We add penalty factors to $\mathcal{L}(\varepsilon,\vec{\theta}\,)$ to constrain the four neutrino fluxes to the SSM [71, 132, 133, 5]:

$$\mathcal{L}(\varepsilon,\vec{\theta}) \quad\rightarrow\quad \mathcal{L}(\varepsilon,\vec{\theta})\cdot\prod_{\nu}\exp\left[-\frac{(\theta_\nu - R^{SSM}_\nu)^2}{2\,\delta^2_{R^{SSM}_\nu}}\right], \tag{4.14}$$

where θ_ν represents the floating value of R_ν, $R^{\rm SSM}_\nu$ the prediction of the SSM based on either the HZ or LZ assumption, and $\delta_{R^{\rm SSM}_\nu}$ is its uncertainty stemming from theoretical uncertainties in the SSM, systematic error in the estimated number of target electrons N_e in the fiducial volume and oscillation parameters.

Performing a series of fits for different values of ε, one can obtain a likelihood probability distribution

$$p(\varepsilon) \;=\; \frac{\mathcal{L}(\varepsilon,\vec{\theta}_{\rm max}(\varepsilon))}{\int d\bar{\varepsilon}\,\mathcal{L}(\bar{\varepsilon},\vec{\theta}_{\rm max}(\bar{\varepsilon}))}\,, \tag{4.15}$$

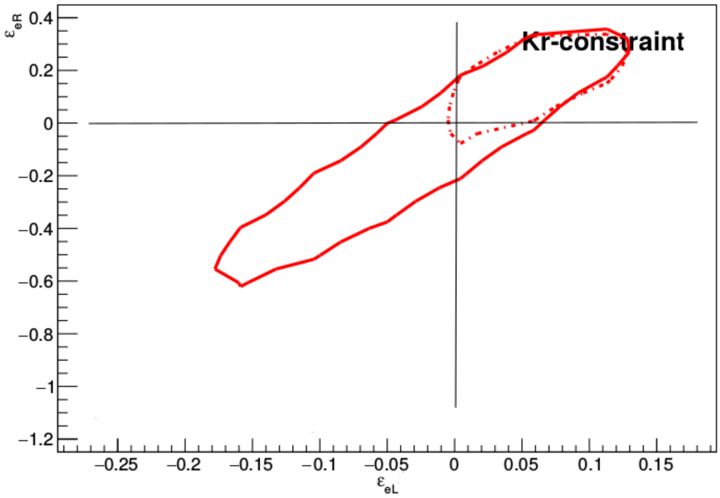

Figure 4.6: Bounds with Kr-constraint applied. Non-consistency of the rate measured with coincidence with the fitter-result rate leads to the systematic shift and statistically significant exclusion of the origin of coordinates that corresponds to the Standard Model physics. 95 % C.L. (2 d.o.f.)

where $\vec{\theta}_{\text{max}}(\varepsilon)$ is the set of values of $\vec{\theta}$ that maximizes the likelihood for that particular value of ε. The upper ε_{up} and lower ε_{low} bounds for a given confidence level (C.L.) can be numerically obtained by integrating the tails of this distribution:

$$\int_{-\infty}^{\varepsilon_{\text{low}}} d\varepsilon\, p(\varepsilon) \;=\; \int_{\varepsilon_{\text{up}}}^{\infty} d\varepsilon\, p(\varepsilon) \;=\; \frac{1-\text{C.L.}}{2}\;. \tag{4.16}$$

For the two dimensional case when two parameters $(\varepsilon_1, \varepsilon_2)$ are under investigation, the confidence region is formed by isocontour $p_0 = \text{const}$, defined though the integral over the excluded region:

$$\iint\limits_{p(\varepsilon_1,\varepsilon_2)<p_0} d\varepsilon_1 d\varepsilon_2\, p(\varepsilon_1, \varepsilon_2) \;=\; 1-\text{C.L.}\;, \tag{4.17}$$

where $p(\varepsilon_1, \varepsilon_2) < p_0$ stands for the region outside of the isocontour p_0.

^{85}Kr-constraint

Fig. 4.6 shows that with current Kr-coincidence measurement we can archive extrinsically strong bound that is highly preferable.

The amount of the Kr-coincidence events generally depends on the type of cuts applied and mass-time of the exposition. For the period that was used in the study (PeriodAll, $m = 156$ tons, $T = 1299$ days) three coincidence events ($k = 3$) was found with expected background $b = 0.47$. Detector efficiency was estimated to be $\epsilon_{det} = 13.6\%$ with systematic error $\sigma = 15\%$ (Ref. [137] and [138]).

The expected number of events could be expressed through the Kr-rate as (Ref. [138]):

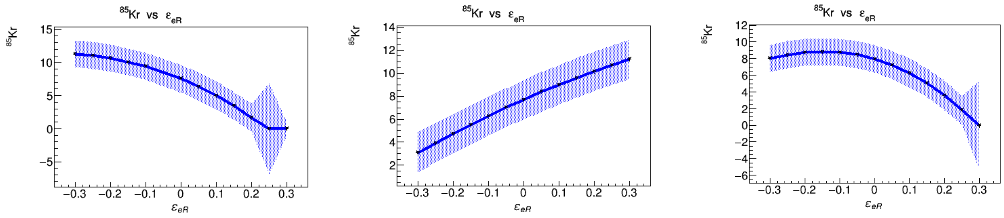

a) b) c)

Figure 4.7: Correlation of Kr with ε_e^R parameter for modification of ^{7}Be-spectrum only (a), *pp*-spectrum (b) only and combined $^7\mathrm{Be} + pp$ (c).

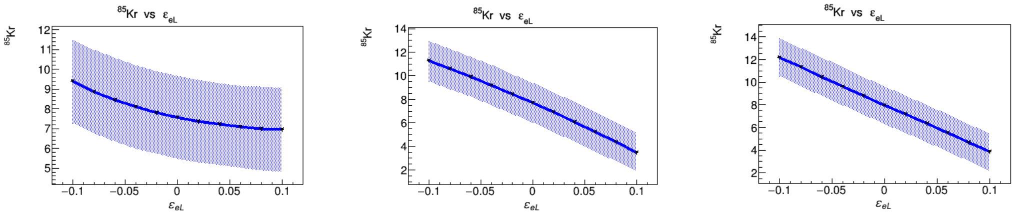

a) b) c)

Figure 4.8: Correlation of Kr with ε_e^L parameter for modification of ^{7}Be-spectrum only (a), *pp*-spectrum only (b) and combined $^7\mathrm{Be} + pp$ (c).

$$\lambda = RmT\epsilon_{BR}\epsilon_{det} \tag{4.18}$$

where $\epsilon_{BR} = 0.43\%$ is a reaction branching ratio.

To incorporate the Kr-penalty in the code the following log-likelihood function was implemented (Ref. [138], [139]):

$$-\,log(\mathcal{L}) = log(1+\sigma) - \frac{k}{1+\sigma}log(\frac{\lambda+b}{1+\sigma}) + log\Gamma(\frac{k}{1+\sigma}+1) + \frac{\lambda+b}{1+\sigma} \tag{4.19}$$

Fig. 4.7 and 4.8 demonstrate the correlation of the krypton rate and $\varepsilon_{R/L}$ for all three considered situations: ^{7}Be-spectrum only (a), *pp*-spectrum only (b) and combined $^7\mathrm{Be} + pp$ (c). Adding a *pp*-spectrum into analysis somehow changes the situation.

In Fig. 4.7, we can see that krypton behaves in the opposite way for ^{7}Be (a) and *pp* (b) cases. When we apply modifications to both lines, we expect that correlations somehow compensate each other. As one can see it happened for $\varepsilon_e^R < 0$: Krypton is at the constant level here. It makes Kr-constraint to be not relevant to the improvement of bound for negative size. For $\varepsilon_e^R > 0$ the rate goes to zero, but not so fast as compared to (a).

Fig. 4.8 shows that Kr-constraint could be highly relevant for ε_e^L: it changes dramatically in (b) and (c) cases. Kr is relevant for *pp*-case (b) more, then for ^{7}Be case. In case of combined analysis krypton (c) inheritances completely the behavior of the *pp*-case.

Such strong correlations suggest the use of the Kr-constraint. However, as it was mentioned before there is inconsistency in the event rates obtained by fast coincidence measurement (about 2 cpd per 100 t) and fitting procedure (about 8 cpd per 100 t). As a possible explanation of this could be an unidentified source of background at low energies that mimic Kr-presence in the fitted spectrum, but not contribute in the coincidence. Another reason could be in the systematic shift in detector efficiency calculation since the energy of the coincidence gamma quite small and close to the detector threshold.

This inconsistency, as well as a strong correlation of the *pp* and ^{7}Be rates with Kr, leads to the shift of the best-fit region far from zero which is quite suspicious.

Interestingly, constraint reduces the part of the contour at negative parameters while the part for the positive ones (first quadrant) remains unchanged. It could be explained by the fact that a zero value of Kr drives the sensitivity in the first quadrant since correlations with ε_L parameter. The Poissonian penalty has nothing to add in the likelihood at zero value, but it can contribute at large Kr rate values in the third quadrant. It suggests postponing the use of Kr-constraint until its status becomes clear.

Radiochemical constraint

Gallium experiments and results

The solar neutrino flux measured by radiochemical experiments is not sensitive to pure leptonic NSI at the production and detection points. A possible impact of pure leptonic NSI in propagation discussed in Sec. 1.2.3.

I used these measurements for the independent constraint on the total number of neutrino events observed in the detector. It became possible because the resent results of Borexino analysis included *pp*, ^{7}Be and *pep* neutrino simultaneously.

The analysis also included CNO spectrum though due to strong correlation in the spectrum with ^{210}Bi, its rate was not yet determined (Ref. [55]). With radiochemical constraint, it became possible to obtain the bounds which are independent on the SSM type (HZ or LZ).

The radiochemical detector's technique (Ref. [140], [141],[142], [4], [143]) exploits the reaction:

$$^{71}\text{Ga} + \nu_e \rightarrow {}^{71}\text{Ge} + e^-$$

for solar neutrino registration which was proposed by Kuzmin in Ref. [144]. The very delicate experimental technique consists of the chemical extraction of the ^{71}Ge atoms from the tens of tons Ga $-$ Ge-alloy (50 tons of Ga and 350 μg Ge for SAGE experiment) and syntheses of germane (GeH$_4$) which is then used to fill a proportional gas counter to reveal the ^{71}Ge-decays ($T_{1/2} = 11.43$ days). The reaction has a threshold 233 keV and sensitive to all neutrino fluxes including *pp*-neutrino flux. Since then several experiments (SAGE, Gallex, GNO) were conducted. They played an important role in understanding the neutrino deficit from the Sun. Combining the statistical and systematic uncertainties in quadrature and weighting the results of all Ga-based experiments one may obtain the count rate [3] (Ref. [140]).

$$R_{\text{Ga}} = 66.1(1 \pm 0.047)\ \text{SNU} = 66.1 \pm 3.1\ \text{SNU}$$

To interpret this result in terms of fluxes and cross sections we will use the formalism described in Ref. [140].

The total rate is a sum of the rates produced by each neutrino flux:

$$R^{\text{Ga}} = \sum_i R_i^{\text{Ga}} \tag{4.20}$$

where $i = \{pp, {}^7\text{Be}, pep, \text{CNO}, {}^8\text{B}\}$. Here the ^{13}N, ^{15}O and ^{17}F are united in CNO component and *hep* is not included as negligible.

Each contribution is proportional to the flux of i-component on the Earth $\phi_i^{\oplus}$ and the convolution of the cross section with the neutrino energy spectrum $< \sigma_i^{\oplus} >$:

$$R_i = \phi_i^{\oplus} \int_{E_{threshold}}^{\infty} \sigma(E) S_i^{\oplus}(E) dE = \phi_i^{\oplus} < \sigma_i^{\oplus} > \tag{4.21}$$

where $S_i^{\oplus}(E)$ - is a expected solar neutrino spectrum at the Earth level normalized by unity: $\int_0^{\infty} S_i^{\oplus}(E) dE = 1$. In fact the shape of $S_i^{\oplus}(E)$ *may* differ from the shape of the

---

[3] SNU unit corresponds to one neutrino capture per second in a target that contains 10^{36} atoms of a neutrino-absorbing isotope.

energy spectrum of neutrino at the Sun $S_i^{\odot}(E)$, since neutrinos with different energies have different "survival" probabilities $P_i^{ee}(E)$.

Differential fluxes at the Sun and Earth are connected in the following way:

$$\Phi^{♁}(E)dE = \Phi^{\odot}(E)dE \tag{4.22}$$

It could be rewritten as:

$$\phi_i^{♁} S_i^{♁}(E)dE = \phi_i^{\odot} S_i^{\odot}(E)P_i^{ee}(E)dE \tag{4.23}$$

Integrating over the energy and using the normalization of $S_i^{♁}(E)$ we obtain:

$$< P_i^{ee} >= \frac{\phi_i^{♁}}{\phi_i^{\odot}} = \int_0^{\infty} S_i^{\odot}(E)P_i^{ee}(E)dE \tag{4.24}$$

The ratio between amplitudes $\phi_i^{♁}$ and $\phi_i^{\odot}$ is denoted as:

$$< P_i^{ee} >= \frac{\phi_i^{♁}}{\phi_i^{\odot}} \tag{4.25}$$

and equation (4.23) could be rewritten in order to give us immediately a recipe for $S_i^{♁}(E)$ calculation:

$$S_i^{♁}(E) = \frac{S_i^{\odot}(E)P_i^{ee}(E)}{< P_i^{ee} >} \tag{4.26}$$

If one put the expression (4.23) into (4.21) one can obtain the expression:

$$R_i = \phi_i^{\odot} \int_{E_{threshold}}^{\infty} \sigma(E)S_i^{\odot}(E)P_i^{ee}(E)dE = \phi_i^{\odot} < \sigma_i^{\odot} > \tag{4.27}$$

where $\phi_i^{\odot}$ and $S_i^{\odot}(E)$ are flux and spectral shape predicted by SSM as well as P_i^{ee} (for MSW it is necessary to know in which part of the Sun neutrinos are produced).

Finally, comparing (4.21) and (4.27) we see that:

$$< \sigma_i^{♁} >= \frac{< \sigma_i^{\odot} >}{< P_i^{ee} >} \tag{4.28}$$

Calculation of the single rates and its uncertainties

Let us analyze Table IV from Ref. [140]. This table contains the calculation of the single rates in SNU as well as its uncertainties.

Following the formula (4.27) the single rate could be calculated as:

$$R_i = \phi_i^{\odot} < \sigma_i^{\odot} >= \phi_i^{\odot} < \sigma_i^{♁} >< P_i^{ee} > \tag{4.29}$$

Three factors contribute into the uncertainty of the single component determination: the uncertainty of the SSM flux $\phi^{\odot}$, cross-section σ uncertainty and the survival probability uncertainty related to oscillation parameters Δm_{12}^2, θ_{12} and θ_{13}. So far I provided the calculations that were analogous to the one from Ref. [140]. Further, I am going to discuss how they can be modified to build radiochemical constraint for Borexino analysis (Sec. 4.5.4). The uncertainties are not symmetrical and positive and negative values are calculated separately.

Let us calculate the uncertainty of the single component determination. It could be found as a quadratic sum of the all three relative uncertainties for the flux δ_ϕ, cross section δ_σ and oscillation probability δ_{Pee}:

$$\delta^2_{R_i} = (\frac{\Delta R_i}{R_i})^2 = \delta^2_\phi + \delta^2_\sigma + \delta^2_{Pee} \tag{4.30}$$

The total absolute uncertainty of the sum of components (expression (4.20)) could be calculated as the quadratic sum of the absolute uncertainties of a single components:

$$\Delta R^{Ga} = \sqrt{\sum_i (\Delta R_i^{Ga})^2} \tag{4.31}$$

The biggest absolute uncertainties are expected to be from the biggest contributors into the sum (in Table IV Ref. [140] they are given in percents). Here we consider GS98 model:

$$R_{pp} = 39.35\,\text{SNU} \;\; \Delta R_{pp} = {}^{+1.5}_{-1.9}\,\text{SNU}$$

$$R_{^7\text{Be}} = 18.73\,\text{SNU} \;\; \Delta R_{^7\text{Be}} = {}^{-1.4}_{+1.8}\,\text{SNU}$$

$$R_{^8\text{B}} = 4.64\,\text{SNU} \;\; \Delta R_{^8\text{B}} = {}^{+1.6}_{-0.86}\,\text{SNU}$$

Other components are negligible. Applying ex.(4.31) to these values one can find the total absolute uncertainty:

$$\Delta R^{\text{Ga}} = {}^{+2.9}_{-2.5}\,\text{SNU} \tag{4.32}$$

Further we will denote this total relative uncertainty as δ_R for Borexino analysis. It could be found as (for $R^{GS98}_{\text{Ga}} = 66.3\text{SNU}$):

$$\delta_R = \frac{\Delta R_{\text{Ga}}}{R^{GS98}_{\text{Ga}}} = {}^{+4.3}_{-3.8}\% \tag{4.33}$$

Radiochemical constraint for Borexino

Let us sum up details of the radiochemical approach that was used in the Borexino's analysis of the neutrino magnetic moment (Ref. [145]). The radiochemical constraint was applied in the form:

$$\sum_i \frac{R_i^{Brx}}{R_i^{SSM}} R_i^{Ga} = (66.1 \pm 3.1 \pm \delta_R \pm \delta_{FV})\text{SNU} \tag{4.34}$$

where R_i^{Ga} are expected gallium rates; the ratio $\frac{R_i^{Brx}}{R_i^{SSM}}$ of Borexino measured rate to its SSM prediction within the MSW-LMA oscillation scenario. The same SSM predictions (High Z) where used for Borexino and gallium expected rates to exclude the dependency from SSM predictions. The error δ_R includes the uncertainty from the estimation of single rates that are contributing into the gallium experiments and the error δ_{FV} is due to the uncertainty of fiducial volume selection for R_i^{SSM} (Ref. [145]).

Spectra *pep*, CNO give a negligible contribution into the magnetic moment analysis and may change the result only by a presence of their rate inside of the radiochemical constraint (4.34). They are fixed with SSM value (HZ and LZ). ^{8}B and hep (negligible) are not participating in the fit at all and also fixed with SSM value (HZ and LZ) giving different contributions again into the sum (4.34).

The error in expression (4.34) should also include errors of the Borexino rate estimation for R_i^{SSM} regarding the uncertainty on the oscillation probability because it also contains it. We will find the solution further to avoid double counting. As we will see the error for radiochemical will include only the uncertainty for the cross section, while the oscillation uncertainty will be related with expected Borexino rate (from the Ref. [55]) it is estimated to be $1-2\%$).

Proper calculation of the error related with survival probability

Since both radiochemical and Borexino experiment are performing the measurement on the Earth and therefore measure the same neutrino fluxes $\phi_i^{♁}$ one may think to try to avoid the uncertainties related to neutrino propagation from the production to detection point, that is probability $P_i^{ee}(E)$ that depends on the oscillation parameters and uncertainty of the flux $\phi_i^{\odot}$.

There are three sources of the error for the rates determination: SSM flux ϕ, σ cross section and oscillation parameters related with P_i^{ee}. In the expression (4.34) both expected values R_i^{SSM} and R_i^{Ga} in $R_i^{SSM}/R_i^{\text{Ga}}$ contain information about the oscillation probabilities $P_i^{ee}(E)$. This fact should be taken into account.

Total uncertainty of the sum of the rates is $+4.3\%$ -3.8 %. Hopefully, since we are using the ratio of the fluxes, we can exclude the contribution from the solar neutrino fluxes. The analysis shows that in case of no SSM uncertainty the total uncertainty of the sum of the rates is $+3.9\%$ -3.3 %. If we also exclude oscillation parameters, the uncertainty became only $+3.3\%$ -1.8 % (you can find this value in Table IV in the column σ as well). In this case, the uncertainty is determined only by the uncertainty of the cross section.

Such a reduction of uncertainty is quite desirable. We are not able to exclude the oscillation probability completely. However, we can try to reduce it, that may positively affect the result.

The first principal problem is related to the fact that Borexino experiment is sensitive to the all types of neutrino (so far we consider ^{7}Be spectrum only):

$$\sigma^{BRX}(E) = \sigma_e^{BRX}(E)P(E) + \sigma_{\mu\tau}^{BRX}(E)(1-P(E))$$

and the probability could not be removed from this expression. Radiochemical experiments, on the contrary, are sensitive only to electron neutrinos.

The calculated ratio of cross sections f could be found as (^{7}Be-case):

$$f = \frac{\sigma_{BRX}^{e}(E_0)}{\sigma_{Ga}(E_0)} + \frac{1-P(E_0)}{P(E_0)}\frac{\sigma_{BRX}^{\mu\tau}(E_0)}{\sigma_{Ga}(E_0)} \tag{4.35}$$

where $E_0 = 862$ keV.

Denoting $n = \sigma_{BRX}^{e}(E_0)/\sigma_{BRX}^{\mu\tau}$ it is easy to get:

$$f = \frac{\sigma_{BRX}^{e}(E_0)}{\sigma_{Ga}(E_0)}\Big(\frac{(n-1)P+1}{nP}\Big) \tag{4.36}$$

The contribution to the error related to survival probability in this case

$$\Delta f = |\frac{\partial f}{\partial P}|\Delta P \tag{4.37}$$

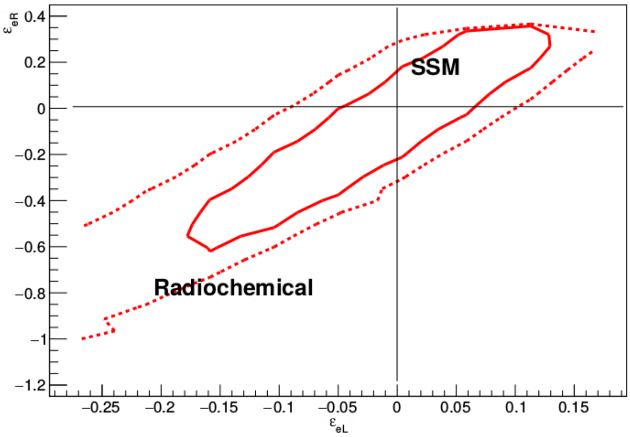

Figure 4.9: Comparison of the radiochemical and SSM constraints. 95 % C.L. 2 d.o.f.

with a partial derivative:

$$\frac{\partial f}{\partial P} = -\frac{1}{nP^2} \times \frac{\sigma^e_{BRX}(E_0)}{\sigma_{Ga}(E_0)} \tag{4.38}$$

Relative error $\frac{\Delta f}{f} = -0.686$ for $n = 4$ and $p = 0.55$.

Now let us obtain the error to be used in the radiochemical penalty term. Borexino observed rate for a given neutrino spectrum is

$$R_i^{Brx} = \phi_i^{\odot} \int_0^{\infty} \sigma_e^{Brx}(E) S_i^{\odot}(E) P_{ee}(E) = \phi_i^{\odot} < \sigma^{\odot}_{Brx,i} > \tag{4.39}$$

One can recalculate Borexino rates into the expected number of counts to be compared with the result of the radiochemical experiments as

$$R_{Brx} = k_{FV,i} \times \sum_i \frac{R_i^{Brx}}{R_i^{SSM}} R_i^{Ga} \tag{4.40}$$

FV contributes into all species and in the same manner with 1% estimated error:

$$k_{FV,i} = 1 \pm \delta_F V \tag{4.41}$$

The error δ_i of $\frac{R_i^{Ga}}{R_i^{SSM}}$ could be calculated using (4.37). The error of the sum is a linear combination:

$$(\delta_R)^2 = \sum_i (R_i^{Brx})^2 \delta_i^2$$

Note that the error depends on the rates R_i^{Brx} that are determined from the fit.

The radiochemical constraint was applied to gain the sensitivity to NSI and compared with HZ-SSM one (Fig. 4.9). It was found to be not so strong as SSM one and, therefore, SSM-constraint was only be considered for all the analysis.

Bounds on NSI and the measurement of $\sin^2\theta_W$

NSI Bounds

In this section, we present our results. Left panels of Figure 4.10 shows the one-dimensional log-likelihood profiles for ε_e^R (red curve) and ε_e^L (blue curve) assuming HZ- (top panel) and LZ-SSM (bottom panel). Right panels of Figure 4.10 portrays the same for ε_τ^R (red curve) and ε_τ^L (blue curve).

Let us first discuss the HZ-SSM case (top panels). One can see that the sensitivity of Borexino to the NSI parameter ε_e^L is more pronounced as compared to its sensitivity to ε_e^R (see top left panel of Figure 4.10). The main reason behind this is that the normalization of neutrino events is well determined by the fit, which in turn provides competitive constraints for ε_e^L. In contrast, the fit still permits quite a wide range for ε_e^R, since the possible modification in the shape of the event spectra due to non-zero ε_e^R can be easily mimicked by the principle background components (mainly ^{85}Kr) discussed above. Note that the minima of the one-dimensional log-likelihood profiles for ε_e^R (red line in left panel) and ε_τ^R (red line in right panel) are slightly deviated from zero, but, needless to mention that these deviations are statistically insignificant.

The one-dimensional log-likelihood profiles for both ε_τ^R and ε_τ^L look non-parabolic in the top right panel of Figure 4.10. In particular, ε_τ^L demonstrates one extra minimum around $\varepsilon_\tau^L \approx 0.6$, which is slightly disfavored at $\Delta\chi^2 \approx 1.5$ as compared to the global minimum at $\varepsilon_\tau^L = 0$. This minimum originates due to the approximate $\tilde{g}_{\alpha L} \leftrightarrow -\tilde{g}_{\alpha L}$ symmetry that Eq. (4.50) possesses, since the first term in Eq. (4.50) dominates over the third term [146]. Because of this symmetry, the value of $\tilde{g}_{\tau L}^2 = (g_{\tau L} + \varepsilon_\tau^L)^2$ is the same for $\varepsilon_\tau^L = 0$ and $\varepsilon_\tau^L = -2g_{\tau L} \approx 0.54$, and therefore, one may expect a local minimum in vicinity of the second point. The presence of the third term in Eq. (4.50) shifts the position of this local minimum slightly upward to $\varepsilon_\tau^L \approx 0.64$.

The profiles for the LZ-SSM case (Figure 4.10, bottom panels) are clearly shifted from zero and with respect to the HZ-SSM ones. The main reason for this is that LZ-SSM predicts smaller $\Phi_{^7\mathrm{Be}}$ compared to HZ-SSM. The smaller flux requires a bigger cross section $\langle\sigma_{^7\mathrm{Be}}\rangle$ for a given observed experimental rate $R_{^7\mathrm{Be}}$ (see Eq. 4.6). As Figure 4.5 illustrates, the total cross section linearly depends on ε_e^L. Therefore, the minimum for LZ-SSM should be shifted in positive direction of ε_e^L. For ε_τ^L the minima go in opposite directions due to the same reason. The only difference is that the cross section increases when ε_τ^L goes in negative direction for the first minimum and when ε_τ^L goes up for the second one (see Figure 4.5, right panel). Aforementioned shifts for ε_e^L and ε_τ^L profiles induce the shifts for ε_e^R and ε_τ^R as well. This will be easy to see later on considering two dimensional profiles (Figures 4.11 and 4.12).

The 90% C.L. (1 d.o.f.) bounds on the flavor-diagonal NSI parameters obtained using the Borexino Phase-II data are listed in Table 4.2. The first column shows the constraints assuming HZ-SSM for the neutrino fluxes. The second column presents the same considering LZ-SSM. These constraints are obtained varying only one NSI parameter at-a-time, while the remaining three NSI parameters are fixed to zero.

The third column exhibits the bounds obtained by phenomenological analysis with Borexino Phase-I data in Ref. [25]. All experimental limits from Borexino Phase-II are better than those previously obtained from the Borexino Phase-I data in Ref. [25]. For the sake of comparison, in the forth column, we present the global bounds from Ref. [22], where the authors analyzed the data from the Large Electron-Positron Collider (LEP) experiment, LSND and CHARM II accelerator experiments, and Irvine, MUNU and Rovno reactor experiments. The bounds found in the present analysis are quite stringent com-

	HZ-SSM	LZ-SSM	Ref. [25]	Ref. [22]
ε_e^R	$[-0.15, +0.11\,]$	$[-0.20, +0.03\,]$	$[-0.21, +0.16\,]$	$[0.004, +0.151\,]$
ε_e^L	$[-0.035, +0.032\,]$	$[-0.013, +0.052\,]$	$[-0.046, +0.053\,]$	$[-0.03, +0.08\,]$
ε_τ^R	$[-0.83, +0.36\,]$	$[-0.42, +0.43\,]$	$[-0.98, +0.73\,]$	$[-0.3, +0.4\,]$
ε_τ^L	$[-0.11, +0.67\,]$	$[-0.19, +0.79\,]$	$[-0.23, +0.87\,]$	$[-0.5, +0.2\,]$

Table 4.2: The first column shows the limits on the flavor-diagonal NSI parameters ε_e^R, ε_e^L, ε_τ^R and ε_τ^L as obtained in the present work using the Borexino Phase-II data and considering HZ-SSM for the neutrino fluxes. The second column displays the same considering LZ-SSM. These constraints are obtained varying only one NSI parameter at-a-time, while the remaining three NSI parameters are fixed to zero. The third column contains the bounds using 153.6 ton$\cdot$years of Borexino Phase-I data as obtained in Ref. [25] (for HZ-SSM case only). For the sake of comparison, we present the global bounds from Ref. [22] in the forth column. All limits are 90% C.L. (1 d.o.f.).

pared to the global ones. One may note that the best up-to-date bound for ε_e^L was obtained in this work.

We have considered above the sensitivity of the detector to NSI's applying the SSM-constraint on the neutrino fluxes. Remarkably, Borexino detector is sensitive to the modification of the shape of ^{7}Be electron recoil spectra even if the neutrino fluxes are not constrained by SSM model. Such analysis provides a limit:

$$-1.14 < \epsilon_e^R < 0.10 \quad (90\%\,\text{C.L.}) \tag{4.42}$$

As one may see the limit is highly asymmetric, with a large extension for the negative values of ε_e^R. Such a small sensitivity is induced by backgrounds (mostly ^{85}Kr) which can easily compensate the modification of electron-recoil spectra.

Now let us consider the two-dimensional case when the allowed region for NSI parameters $\varepsilon_e^{L/R}$ is plotted while ε_τ^L and ε_τ^R are fixed to zero (Figure 4.11). Two contours for HZ- (filled) and LZ-SSM (dashed) were obtained. Compared with other experiments sensitive to the same NSI's, the allowed contours for Borexino in the ε_e^L-ε_e^R plane have a distinct orientation, cf. Figure 4.11. The TEXONO experiment [21] is mostly sensitive to ε_e^R, while LSND [19, 20] is mostly sensitive to ε_e^L . Borexino's contour intersects the allowed regions for both experiments at a certain angle, and the three experiments complement each other. In principle, the overlap of Borexino with TEXONO results in two allowed regions. To exclude the second intersection, the incorporation of the LSND result is necessary.

As it was already explained in the analysis of one-dimensional profiles the contours for HZ- and LZ-SSM's are shifted along ε_e^L-axis. However, in one-dimensional case the shift for ε_e^R was obscure. Now, considering two-dimensional case it is evident that for a given shape of the contours such a shift in ε_e^L have to produce also the displacement for ε_e^R.

The contours for Borexino are extended along the direction

$$\varepsilon_e^R \;=\; k\,\varepsilon_e^L\;, \tag{4.43}$$

with $k \approx 3.75$, due to the presence of backgrounds, especially ^{85}Kr. As it was previously found in [25] and confirmed in the current study, this background easily absorbs the modification of shape and normalization of the ^{7}Be spectrum for a set of parameters that satisfy this expression. Note that the choice of the SSM modifies not only the measured neutrino rates but also the configuration of backgrounds that, in turn, produces an additional shift along (4.43).

For both HZ- and LZ-SSM cases, the bounds on the left parameter are stronger than the result from LSND. TEXONO [21] is a reactor antineutrino experiment and its bounds are obtained from $\overline{\nu_e}e$ scattering. For anti-neutrinos the roles of $\tilde{g}_{eL}$ and $\tilde{g}_{eR}$ are reversed, leading to a stronger bound on ε_e^R. Due to the approximate symmetry $\tilde{g}_e^R \leftrightarrow -\tilde{g}_e^R$ in the anti-neutrino scattering cross section, two separate contours form the allowed region of TEXONO around $\varepsilon_e^R = 0$ and $\varepsilon_e^R = -2g_{eR} = -2\sin^2\theta_W \approx -0.5$.

The result of Borexino in the ε_τ^L-ε_τ^R plane is shown in Figure 4.12. It is similar to that of LEP [22] in excluded area, but it occupies a slightly different region, favoring positive ε_τ^R and negative ε_τ^L. NSI's comparable with the SM neutral current interactions are still allowed.

The result for LZ-SSM is of particular interest. The shift of the minima discussed above and observed in Figure 4.10 (bottom right) transforms the allowed contour (Figure 4.12, dashed dark blue) into two separate regions, one of which is already almost completely excluded by LEP data. So, the remaining allowed region, in this case, is relatively small.

The dotted gray lines in Figures 4.11 and 4.12 indicate the range for the parameter ε' relevant for NSI's at propagation. The contours are almost entirely located between $\varepsilon' = -0.5$ and $\varepsilon' = 0.5$. As it was previously shown (see Figure 1.6), NSI's at propagation are not very pronounced for these magnitudes of ε' compare to the precision of the the measurements. Thus, the sensitivity of the detector is mostly determined by NSI's at detection.

$\sin^2\theta_W$ measurement

Finally, in addition to the analysis of NSI's, using the same data and analysis strategy, we constrain the value of $\sin^2\theta_W$ in the SM. Instead of introducing NSI's, we simply allow $\sin^2\theta_W$ in the SM-NC couplings to vary. The sensitivity of the analysis to $\sin^2\theta_W$ is mostly dominated by g_e^L while contributions of the other five coupling constants are almost negligible. For the HZ-SSM case, the analysis of a likelihood profile results in

$$\sin^2\theta_W = 0.229 \pm 0.026\,\text{(stat+syst)}\;,^4 \tag{4.44}$$

which is consistent with theoretical expectations [1] and comparable in precision with the value found by the reactor $\overline{\nu_e}e$ scattering experiment TEXONO [21]:

$$\sin^2\theta_W = 0.251 \pm 0.031\,\text{(stat)} \pm 0.024\,\text{(syst)}\;. \tag{4.45}$$

The most accurate determination of $\sin^2\theta_W$ by neutrino-electron scattering is from the $\nu_\mu e$ scattering experiment CHARM II [70]:

$$\sin^2\theta_W = 0.2324 \pm\; 0.0058\,\text{(stat)} \pm\; 0.0059\,\text{(syst)}\;. \tag{4.46}$$

---

[4] It has been brought to our attention that several naive analyses of published Borexino data have been performed in the literature claiming smaller error bars on $\sin^2\theta_W$ and the neutrino magnetic moment (e.g. in Khan, A.N. Journal of Physics G: Nuclear and Particle Physics. **46**(3), 2019), than respectively claimed here and in Ref. [145]. Unfortunately, these analyses ignore the effect of $\sin^2\theta_W$ and neutrino magnetic moment on the recoil-electron spectral shape (see also comment on page 24 in Ref. [147]).

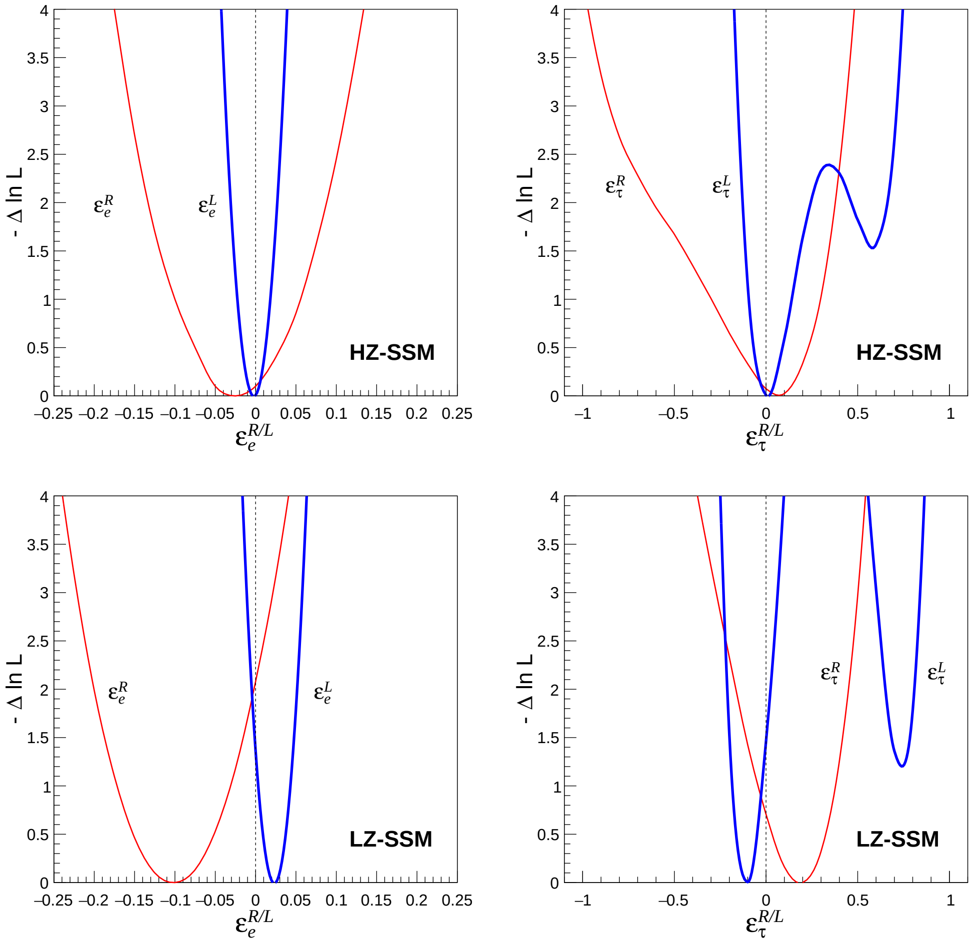

Figure 4.10: Left panels show the log-likelihood profiles for the NSI parameter ε_e^R (red line) and ε_e^L (blue line) assuming HZ (top panel) and LZ (bottom panel) SSM's. Right panels depict the same for ε_τ^R (red line) and ε_τ^L (blue line). The profiles were obtained considering one NSI parameter at-a-time, while remaining NSI parameters were fixed to zero.

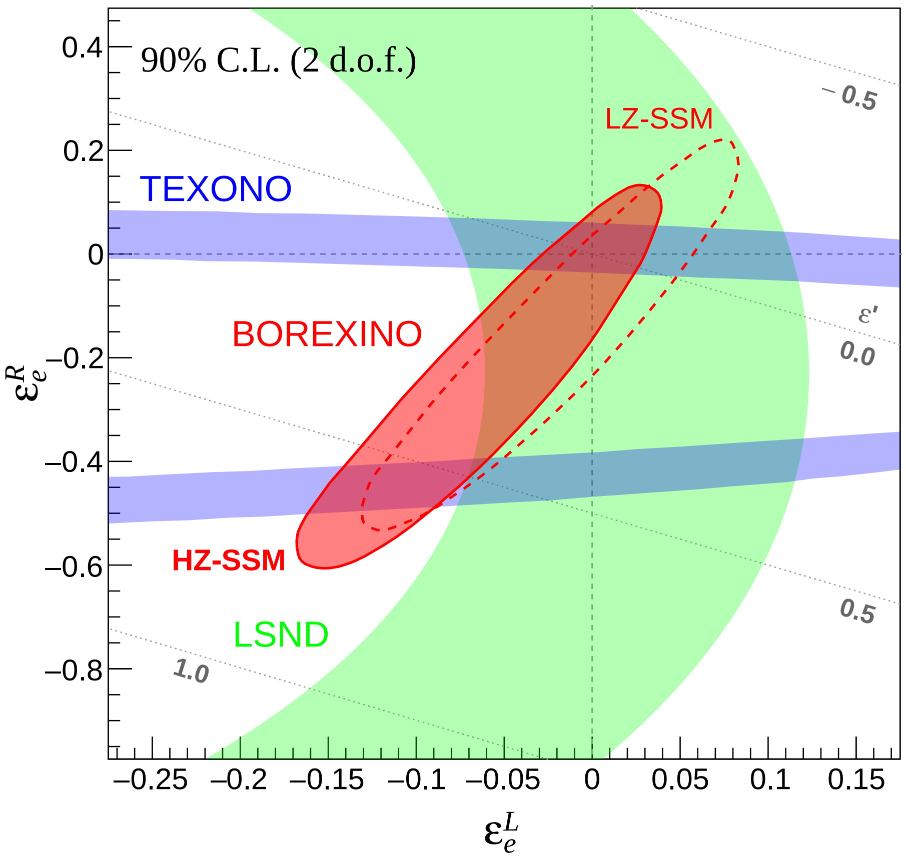

Figure 4.11: Allowed region for NSI parameters in $\varepsilon_e^{L/R}$ plane obtained in the present work. The parameters ε_τ^L and ε_τ^R are fixed to zero. Both HZ- (filled red) and LZ- (dashed red) SSM's were assumed. The bounds from LSND [19, 20] and TEXONO [21] are provided for comparison. All contours correspond to 90% C.L. (2 d.o.f.). The dotted gray lines represent the corresponding range of ε' parameter, relevant for NSI's at propagation.

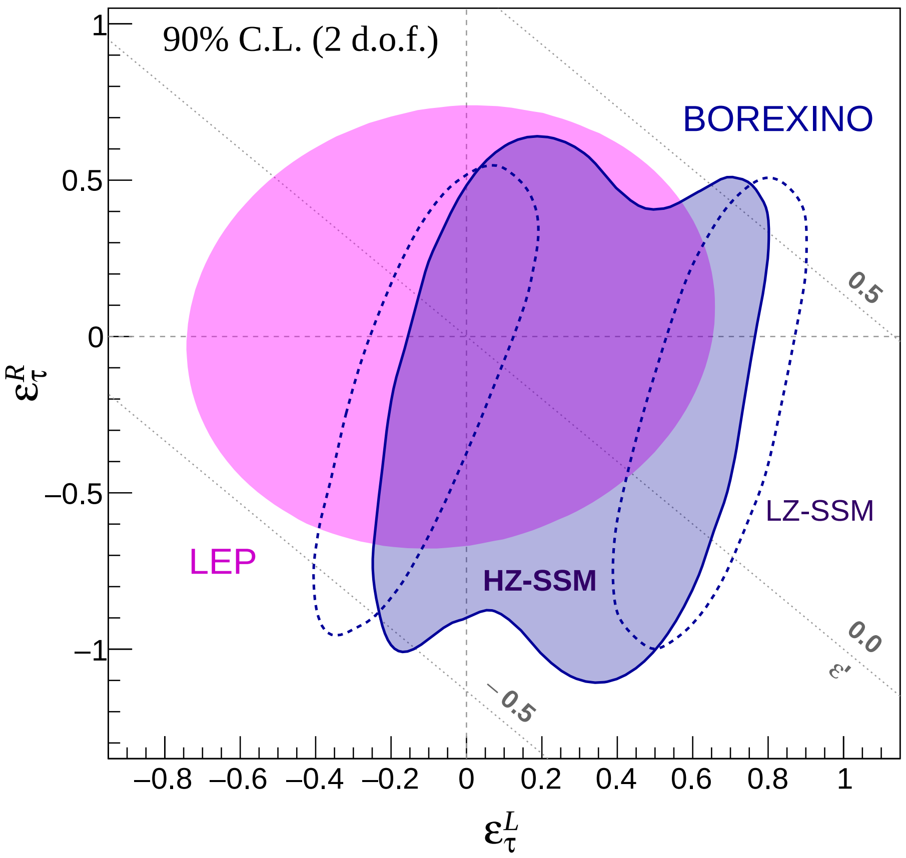

Figure 4.12: Allowed region for NSI parameters in $\varepsilon_\tau^{L/R}$ plane obtained in the present work. The parameters ε_e^L and ε_e^R are fixed to zero. Both HZ- (filled dark blue) and LZ- (dashed dark blue) SSM's were assumed. The contour from LEP [22] is provided for comparison. Both contours correspond to 90% C.L. (2 d.o.f.). The dotted gray lines represent the corresponding range of ε' parameter, relevant for NSI's at propagation.

Limits on $\nu_e \to \bar{\nu}_e$ conversion probability in the Sun due to SFP

Spin-flavor precession mechanism

The same analysis approach could be used to study $\bar{\nu}$-appearance in the Sun. The presence of anti-neutrinos in originally neutrino fluxes can be a consequence of neutrino electromagnetic interactions induced by the non-zero neutrino magnetic moment μ_ν (see [148] for a recent review of neutrino electromagnetic properties). Being roughly proportional to the neutrino mass [149], μ_ν is expected to be non-zero in the light of oscillation paradigm with massive neutrinos. Therefore, antineutrino detection can be applied to studies of neutrino electromagnetic properties.

Neutrinos with non-zero μ_ν interacting with strong magnetic fields in the Sun may undergo spin-flavor precession (SFP) which changes their helicity and, possibly, flavor [150]. Dirac neutrinos under SFP transit into a sterile right-handed state, while for Majorana neutrinos spin-flip is equivalent to $\nu_\alpha - \bar{\nu}_\beta$ conversion. Under the CPT conservation this process for Majorana neutrinos is necessarily accompanied by the flavor change, and thus, the appearance of $\bar{\nu}_e$ in the Sun can be described as a combined effect of SFP and neutrino oscillations:

$$\nu_e \xRightarrow{\text{SFP}} \bar{\nu}_\mu \xRightarrow{\text{oscillations}} \bar{\nu}_e \tag{4.47}$$

$$\nu_e \xRightarrow{\text{oscillations}} \nu_\mu \xRightarrow{\text{SFP}} \bar{\nu}_e \tag{4.48}$$

Method

The shape distortion of the electron recoil spectra observed by Borexino can be used as a probe of for $\nu_e/\bar{\nu}_e$-composition of incoming solar neutrino fluxes. Moreover, the conversion of neutrino into antineutrino should reduce the detected neutrino rate since the electron antineutrino cross section is substantially smaller than the one for electron neutrino. Therefore, by constraining solar neutrino fluxes with the prediction of the Standard Solar Model (SSM) [5], one can gain additional sensitivity to the conversion. It is worth mentioning that the reaction of elastic neutrino scattering is also sensitive to neutrino magnetic moment and was previously used in Ref. [145] to put a strong bound on its value.

The previous limit on neutrino-antineutrino conversion $p_{\nu\to\bar{\nu}}$ obtained by Borexino using the method described in this section is [151]:

$$p_{\nu\to\bar{\nu}} < 0.35\ (90\%\text{C.L.}) \tag{4.49}$$

In the present work, we improve this limit following the recent progress of Borexino in solar neutrino detection [6].

We assume that the MSW mechanism takes place while the $\nu \to \bar{\nu}$ conversion is a second-order process. As it was previously shown, the differential cross section of neutrino elastic scattering off electron for all neutrino flavors is given by the expression:

$$\frac{d\sigma_\alpha(E,T)}{dT} = \frac{2}{\pi} G_F^2 m_e \left[g_{\alpha L}^2 + g_{\alpha R}^2 \left(1 - \frac{T}{E}\right)^2 - g_{\alpha L} g_{\alpha R} \frac{m_e T}{E^2} \right], \tag{4.50}$$

where G_F is the Fermi constant, m_e - electron mass, and E and T are neutrino and recoil electron kinetic energies, correspondingly. The coupling constants at tree level are given by expressions:

$$
\begin{aligned}
g_{\alpha L} &= \begin{cases} \sin^2\theta_W + \frac{1}{2} & \text{for } \alpha = e, \\ \sin^2\theta_W - \frac{1}{2} & \text{for } \alpha = \mu, \tau, \end{cases} \\
g_{\alpha R} &= \sin^2\theta_W \qquad \text{for } \alpha = e, \mu, \tau.
\end{aligned} \tag{4.51}
$$

Note that ν_μ and ν_τ have the same cross section at tree level due to equal coupling constants.

The differential cross section for antineutrinos has the same form as (4.50) but the positions of g_L and g_R coupling constants are swapped, and their values for all three flavors are:

$$
g_L = \sin^2\theta_W - \frac{1}{2} \qquad g_R = \sin^2\theta_W, \tag{4.52}
$$

Electron neutrinos interact with electrons by both CC and NC while $\bar{\nu}_e$ by NC only and ν_e has approximately three times larger cross section than $\bar{\nu}_e$. Moreover, the swap of the coupling constants affects the second and the third energy-dependent terms in (4.50) and, therefore, distorts the shape of the spectrum.

Both $\nu_{\mu/\tau}$ and $\bar{\nu}_{\mu/\tau}$ interact with electrons by NC. Since $g^2_{\mu/\tau R} \approx g^2_{\mu/\tau L}$ the shape and normalization of the spectra are almost the same for neutrinos and anti-neutrinos and effect of the shape distortion is less pronounced compared to ν_e - case. Thus, the Borexino is sensitive to only $\nu_e \to \bar{\nu}_e$ conversion.

Taking into account antineutrino component due to $\nu - \bar{\nu}$ conversion, the observed spectra in the detector is given by the expression[5]:

$$
\frac{dR_\nu}{dT} = N_e \Phi_\nu \int dE \, \frac{d\lambda_\nu}{dE} \left[A_\nu (1 - p_{\nu\to\bar{\nu}}) + A_{\bar{\nu}} p_{\nu\to\bar{\nu}} \right] , \tag{4.53}
$$

where N_e is a number of electrons in the fiducial volume, Φ_ν and $\frac{d\lambda_\nu}{dE}$ are total neutrino flux and energy spectrum for a given neutrino type $\nu = pp$, ^{7}Be, pep, CNO; $P_{ee}(E)$ is a electron neutrino survival probability predicted by MSW-LMA and

$$
A_\nu = \frac{d\sigma_{\nu_e}}{dT} P_{ee}(E) + \frac{d\sigma_{\nu_{\mu/\tau}}}{dT} (1 - P_{ee}(E)) \tag{4.54}
$$

$$
A_{\bar{\nu}} = \frac{d\sigma_{\bar{\nu}}}{dT} \tag{4.55}
$$

The monochromatic ^{7}Be-line plays a dominant role in the analysis as the most sensitive to the spectral shape distortion and change of the normalization.

Solar neutrino fluxes Φ_ν were constrained with SSM with High-(HZ) and Low-(LZ) metallicity SSM's[5]. The uncertainties related with the fiducial volume determination and oscillation parameters, as the primary sources of the systematics, were found to be small compared to the uncertainties associated with SSM-flux prediction and were incorporated together with SSM-penalty terms.

The fitting procedure consists of the multivariate maximization of the composite likelihood function $L(p_{\nu\to\bar{\nu}}, \vec{\theta})$ described in [130, 145] for set of $p_{\nu\to\bar{\nu}}$ values. Then, the likelihood profile was analysed to determine the upper bound for $p_{\nu\to\bar{\nu}}$.

---

[5] For clarity, we present this formula in energy units, omitting the convolution with the energy response function of the detector

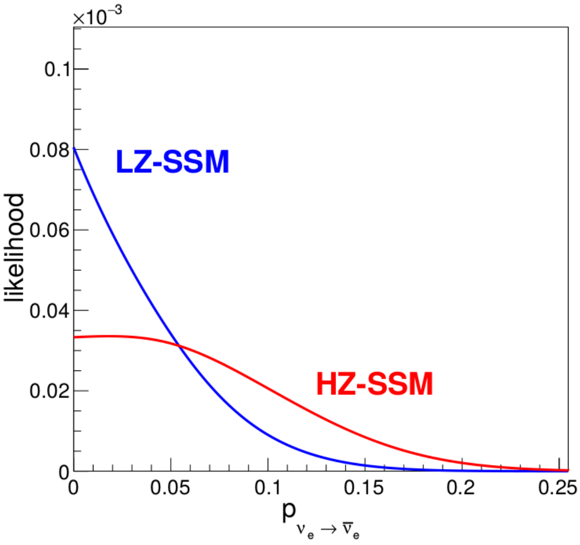

Figure 4.13: Likelihood profiles for $\nu \to \bar{\nu}$ conversion probability obtained with HZ- and LZ-SSM constraints.

Results

The corresponding likelihood profiles for HZ- and LZ-SSM are shown in Fig. 4.13. By numerical integration of the profiles in Fig. 4.13, one can obtain bounds for $p_{\nu\to\bar{\nu}}$ for HZ-SSM case:

$$p^{HZ}_{\nu\to\bar{\nu}} < 0.14 \, (90\%\text{C.L.}) \tag{4.56}$$

and for LZ-SSM:

$$p^{LZ}_{\nu\to\bar{\nu}} < 0.09 \, (90\%\text{C.L.}) \tag{4.57}$$

We can take (4.56) as a conservative final result that does not depend on the choice of SSM, providing an improvement by a factor of two with respect to the limit (4.49), previously obtained in [151].

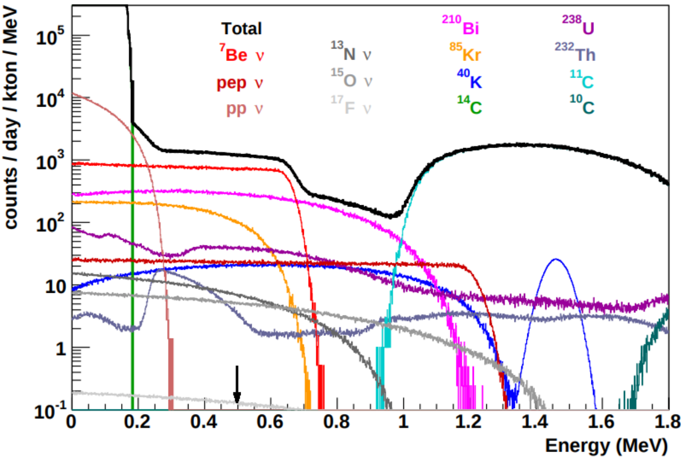

Figure 4.14: Expected solar neutrino spectra with backgrounds. The most optimistic purification result were supposed. Anticipated detector threshold ∼ 500 keV is indicated by black arrow. See the text for more details. (from Ref. [9])

JUNO solar neutrino program and sensitivity to NSI

In this subsection, the possibility to search for NSI's with JUNO is analyzed. In the introduction 1.2.8, NSI with reactor anti-neutrino were briefly reviewed. Here, we consider the analysis strategy with solar neutrinos that were used for Borexino to obtain the limits on $\varepsilon_e^{R/L}$ and $\varepsilon_\tau^{R/L}$. It is clear that the applicability of this analysis to JUNO depends on the successful realization of the solar neutrino program.

The simulated solar neutrino spectra with backgrounds for JUNO is presented in Fig. 4.14. In principle, the better energy resolution will make an advantage for solar neutrino studies since both signal and background spectra could be well-separated. However, there are several other critical factors: cosmogenic background, PMT dark count rate and radiopurity (Ref. [9], [152] and [153]). The detector will be located quite near to the surface with 3 events of muons per second in the whole detector. The cosmogenic background will have a serious impact unless special techniques are applied for its tagging and removal from the spectrum similar to the one used for Borexino. Effective discrimination of β^+ and β^- emitters will also become possible thanks to new topological track reconstruction algorithm (Ref. [154]). Especially it is important for ^{8}B detection since its spectrum is located in the energy range of the cosmogenic ^{10}C, ^{11}C and ^{11}Be. Dark count rate may significantly contribute into the resolution at low energies, degrading nominal energy resolution and reducing sensitivity to *pp* and ^{7}Be neutrino. Finally, strict radiopurity requirements should be fulfilled to reduce the contribution of background events from ^{238}U, ^{232}Th, ^{40}K and gaseous ^{85}Kr. In Fig. 4.14 one may see the interweaving of these backgrounds with electron recoil spectra. Here in Fig. 4.14 we consider the most optimistic case with $^{238}\text{U} = 10^{-17}$ g/g, $^{232}\text{Th} = 10^{-17}$ g/g, $^{40}\text{K} = 10^{-18}$ g/g and ^{85}Kr about 100 counts/day/kton. As it was found in previous chapter, the current purification procedure should be significantly improved to archive these levels.

One more important requirement is a detector threshold that is currently supposed to be about 500 keV. It makes impossible the detection of *pp* neutrino and reduces the low energy part of ^{7}Be spectrum significantly, leaving only the part near the shoulder.

Supposing this configuration of JUNO detector as final and applying finding of the analysis for Borexino it already possible to give some definitive conclusion about the ability to search for NSI with JUNO.

As in the case of Borexino ^{7}Be spectrum plays a primary role for the sensitivity. The left ε_e^L NSI parameter was associated with normalization of the spectrum and ε_e^R with its shape. Since their quite distinct behavior, we can analyze them separately.

The sensitivity to the normalization of the total spectra (in other words to the total cross section) mainly depends on two factors: the precision of the measurement of the ^{7}Be rate by a detector and uncertainty of the ^{7}Be flux from the Standard Solar Model. In the analysis χ^2 (likelihood function) was build incorporating χ^2_{fit} value of the comparison experimental spectra and detector model and $\chi^2_{SSM\ penalty}$ term for the neutrino flux:

$$\chi^2 = \chi^2_{fit} + \chi^2_{SSM\ penalty} \tag{4.58}$$

The "strength" of χ^2_{fit} term, that is its possibility to limit ε_e^L inversely proportional to the relative precision of the ^{7}Be measurement. The more precise measurement is the stronger ^{7}Be "" into experimental spectrum.

The "strength" of $\chi^2_{SSM\ penalty}$ is inversely proportional to the SSM model flux uncertainty.

Currently, SSM uncertainty (5 %) is larger than the precision of the (2.8 %) ^{7}Be-flux measurement. Therefore the sensitivity to NSI is dominated by the SSM constraint and improvement of the ^{7}Be precision does not refine the constraints. More precise measurement become relevant when the uncertainty of the SSM flux is reduced which in turn lead to the automatic improvement of the limits.

JUNO is not supposed to improve ε_e^L parameter even if more precise measurements of the ^{7}Be-flux will be performed unless the SSM uncertainty of the flux will be significantly reduced.

^{8}B neutrino could be also considered for NSI studies. Apart from the sensitivity at the detection point, since it is located in matter energy region and should be sensitive to NSI at propagation as well (see Sec. 1.2.3). However, it is untimely to derive any conclusion about expected sensitivity since the feasibility for ^{8}B measurement is still on the early stage of discussion (Ref. [9],[152], [153]).

Conclusions

In this chapter, we search for Non-Standard Interactions (NSI's) of the neutrino using Borexino Phase-II data. The NSI's considered were those of the Neutral-Current (NC) type that modify the $\nu_e e$ and $\nu_\tau e$ couplings while preserving their chiral and flavor structures.

Such NSI's can affect solar neutrinos at production, propagation, and detection. Neutrino production in the Sun can be affected via processes such as $\gamma e \to \nu\overline{\nu}e$, but the expected modification in the neutrino spectrum is at energies well below the detection threshold of Borexino ($\sim$50 keV) so this effect need not be considered. The NSI's considered also modify the solar neutrino survival probability $P_{ee}(E)$ via the LMA-MSW effect as the neutrinos propagate out through the matter of the Sun. However, this effect is dominant at ^{8}B neutrino energies but not particularly large at ^{7}Be neutrino energies, limiting the sensitivity of Borexino to such modifications. The dominant effect of the NSI's is at detection where the shape of the electron-recoil spectrum is sensitive to any change in the $\nu_e e$ and $\nu_\tau e$ couplings.

The solar neutrino fluxes were constrained to the prediction of the Standard Solar Model (SSM) with the LMA-MSW oscillation mechanism. SSM's with both high- (HZ) and low-metallicity (LZ) were considered. Systematic effects related to the characterization of the target mass of the detector and the choice of oscillation parameters were taken into account.

The modifications to the $\nu_e e$ and $\nu_\tau e$ couplings are quantified by parameters $\varepsilon_e^{L/R}$ and $\varepsilon_\tau^{L/R}$. The bounds to all four parameters were obtained in this analysis, and they all show marked improvement compared to the Borexino Phase-I analysis [25], regardless of the choice of metallicity in the SSM, *cf.* Table 4.2. The bounds are quite stringent compared to the global ones: the best to-date limit for ε_e^L was obtained.

The log-likelihood profiles and corresponding bounds for HZ- and LZ-SSM's are shifted with respect to each other due to different expected neutrino detection rates. The minima of HZ-profiles are less shifted from zero as a result of better agreement between the measured neutrino rates and HZ-SSM. For LZ-SSM, the deviations of the minima of the profiles from zero are more sizable but still statistically insignificant. The allowed contour of Borexino in the $\varepsilon_e^{L/R}$-plane is quite distinct with respect to other νe or $\overline{\nu}e$ scattering experiments, also sensitive to the same NSI's, such as TEXONO and LSND. Borexino is sensitive to both ε_e^R and ε_e^L parameters while TEXONO and LSND mostly constrain only ε_e^R or ε_e^L, respectively. Notably, in the case of $\varepsilon_\tau^{L/R}$ two local minima are observed. The distance between the minima is larger for LZ-SSM, resulting in the splitting of the 90 % C.L. allowed contour into two contours in the $\varepsilon_\tau^{L/R}$-plane.

This investigation reveals the principle role of ^{85}Kr-background in the analysis due to its correlation with ^{7}Be. Applying an independent measurement of Kr and constraining its expected rate reduces allowed region for $\varepsilon_e^{R/L}$ and ε_τ^R parameters. The role of Bi-background and its constraining was found to be insignificant.

The smaller, conservative, NH-value for θ_{23} was chosen for the $\varepsilon_\tau^{L/R}$-analysis. If instead, the neutrino mass hierarchy is identified as inverted in the future experiments, the contribution of the τ-neutrino into the cross section will be bigger and the bounds for $\varepsilon_\tau^{L/R}$ will be slightly improved. Finally, the most crucial factor which determines the sensitivity is the uncertainty of ν-fluxes predicted by SSM (primarily 6% for $\Phi_{^7\mathrm{Be}}$): their further reduction directly refines the bounds.

The detector is sensitive to ε_e^R, even without constraining the neutrino fluxes to the

SSM, purely via the modification to the electron-recoil spectral shape. However, it was found that backgrounds reduces this sensitivity dramatically by compensating for the modification to the spectra, especially for negative ε_e^R.

The same dataset and analysis approach could be used to constrain $\sin^2\theta_W$ and to place a limit on the probability of $\nu_e - \bar{\nu}_e$ conversion in the Sun. The resulting value of $\sin^2\theta_W$ is comparable in precision to that measured in reactor antineutrino experiments. Besides, the most robust limit was set for $\nu_e - \bar{\nu}_e$ conversion probability of solar neutrinos with energies lower than the threshold of inverse beta decay reaction $E_\nu < 1.8\,\mathrm{MeV}$.

The analysis of further possible improvements of NC NSI bounds in the context of JUNO potential showed a modest perspective. At the current situation, the sensitivity is mostly driven by the uncertainty of the SSM fluxes prediction. Therefore, the limits could be refined in the future together with SSM development.

Bibliography

[1] J. Erler and P. Langacker. Electroweak model and constraints on new physics. *the section on Reviews, Tables, and Plots in this Review*, 2008.

[2] R.N. Cahn et al. White paper: measuring the neutrino mass hierarchy. *arXiv preprint arXiv:1307.5487*, 2013.

[3] W. C. Haxton. Solar Neutrinos: Status and Prospects. *Ann. Rev. Astron. Astrophys.*, 51:21–61, 2013.

[4] J. N. Bahcall, A. Serenelli, and S. Basu. New solar opacities, abundances, helioseismology, and neutrino fluxes. *The Astrophysical Journal Letters*, 621(1):L85, 2005.

[5] N. Vinyoles, A. Serenelli, F. L. Villante, et al. A new Generation of Standard Solar Models. *Astrophys. J.*, 835(2):202, 2017.

[6] M. Agostini et al. Comprehensive measurement of *pp*-chain solar neutrinos. *Nature*, 562(7728):505–510, 2018.

[7] D Akimov et al. Observation of coherent elastic neutrino-nucleus scattering. *Science*, 2017.

[8] T. Ohlsson, H. Zhang, and S. Zhou. Non-standard interaction effects on neutrino parameters at medium-baseline reactor antineutrino experiments. *Physics Letters B*, 728:148–155, 2014.

[9] F. An et al. Neutrino Physics with JUNO. *J. Phys.*, G43(3):030401, 2016.

[10] F. Capozzi, E. Lisi, and A. Marrone. Neutrino mass hierarchy and electron neutrino oscillation parameters with one hundred thousand reactor events. *Phys. Rev.*, D89(1):013001, 2014.

[11] M. J. Berger. Xcom: photon cross sections database. *http://www. nist. gov/pml/data/xcom/index. cfm*, 2010.

[12] M. J. Berger. Estar, pstar, and astar: Computer programs for calculating stopping-power and range tables for electrons, protons, and helium ions. *NIST*, 1992.

[13] M. Agostini, A. Formozov, et al. The Monte Carlo simulation of the Borexino detector. *Astropart. Phys.*, 97:136–159, 2018.

[14] G. F. Knoll. *Radiation Detection and Measurement, 3rd ed.* John Wiley and Sons, New York, 2000.

[15] S. Ajimura et al. Technical Design Report (TDR): Searching for a Sterile Neutrino at J-PARC MLF (E56, JSNS2). 2017.

[16] T. Marrodán Undagoitia et al. Fluorescence decay-time constants in organic liquid scintillators. *Review of Scientific Instruments*, 80(4):043301, 2009.

[17] E. CAVALLÉ et al. Features of a liquid scintillator for reactor anti-neutrinos detection. *Tesi di laurea. Supervisors: Meroni, E. and Formozov, A.*, 2017.

[18] L. Swiderski et al. Electron response of some low-Z scintillators in wide energy range. *Journal of Instrumentation*, 7(06):P06011, 2012.

[19] S. Davidson, C. Pena-Garay, et al. Present and future bounds on nonstandard neutrino interactions, 2003.

[20] L. B. Auerbach et al. Measurement of electron-neutrino electron elastic scattering. *Phys. Rev.*, D63:112001, 2001.

[21] M. Deniz et al. Constraints on Non-Standard Neutrino Interactions and Unparticle Physics with Neutrino-Electron Scattering at the Kuo-Sheng Nuclear Power Reactor. *Phys. Rev.*, D82:033004, 2010.

[22] J. Barranco, O. G. Miranda, C. A. Moura, and J. W. F. Valle. Constraining non-standard neutrino-electron interactions. *Phys. Rev.*, D77:093014, 2008.

[23] F. Suekane. Neutrino oscillations. In *Lecture Notes in Physics, Berlin Springer Verlag*, volume 898. Springer, 2015.

[24] Z. Berezhiani et al. Probing nonstandard couplings of neutrinos at the Borexino detector, 2002.

[25] Sanjib Kumar Agarwalla, Francesco Lombardi, and Tatsu Takeuchi. Constraining Non-Standard Interactions of the Neutrino with Borexino. *JHEP*, 12:079, 2012.

[26] N. Bohr. Conservation laws in quantum theory. *Nature*, 138(3479):25, 1936.

[27] W Pauli. Rapports du septieme conseil de physique solvay. *Brussels (Gauthier Villars, Paris, 1934)*, 1933.

[28] E. Fermi. Versuch einer theorie der β-strahlen. i. *Zeitschrift für Physik*, 88(3-4):161–177, 1934.

[29] H. Bethe and R. Peierls. The "neutrino". *Nature*, 133(3362):532, 1934.

[30] F Reines and C.L. Cowan Jr. A proposed experiment to detect the free neutrino. *Physical Review*, 90(3):492, 1953.

[31] T. D. Lee and C. N. Yang. Question of parity conservation in weak interactions. *Phys. Rev.*, 104:254–258, Oct 1956.

[32] C. Wu et al. Experimental test of parity conservation in beta decay. *Physical review*, 105(4):1413, 1957.

[33] F. Boehm and P. Vogel. Physics of massive neutrinos, 1992.

[34] S. L. Glashow. Partial-symmetries of weak interactions. *Nuclear Physics*, 22(4):579–588, 1961.

[35] A. Salam and J. C. Ward. Electromagnetic and weak interactions. In *Selected Papers Of Abdus Salam: (With Commentary)*, pages 210–213. World Scientific, 1994.

[36] S. Weinberg. A model of leptons. *Physical review letters*, 19(21):1264, 1967.

[37] F.J. Hasert et al. Observation of neutrino-like interactions without muon or electron in the gargamelle neutrino experiment. *Nuclear Physics B*, 73(1):1–22, 1974.

[38] G. Arnison et al. Experimental observation of lepton pairs of invariant mass around 95 GeV/c^2 at the CERN SPS collider. *Physics Letters B*, 126(5):398–410, 1983.

[39] B. Adeva et al. A determination of the properties of the neutral intermediate vector boson Z. *Physics Letters B*, 231(4):509–518, 1989.

[40] G. Aad et al. Observation of a new particle in the search for the Standard Model Higgs boson with the ATLAS detector at the LHC. *Physics Letters B*, 716(1):1–29, 2012.

[41] G. Aad et al. Combined Measurement of the Higgs Boson Mass in p p Collisions at s= 7 and 8 TeV with the ATLAS and CMS Experiments. *Physical review letters*, 114(19):191803, 2015.

[42] B. Pontecorvo. Mesonium and antimesonium. *Zhur. Eksptl'. i Teoret. Fiz.*, 33, 1957.

[43] S.M. Bilenky. Neutrino oscillations: From a historical perspective to the present status. *Nucl. Phys.*, B908:2–13, 2016.

[44] B. Pontecorvo. Inverse beta processes and nonconservation of lepton charge. *Zhur. Eksptl'. i Teoret. Fiz.*, 34, 1958.

[45] B. Pontecorvo. Neutrino experiments and the problem of conservation of leptonic charge. *Sov. Phys. JETP*, 26(984-988):165, 1968.

[46] L. Wolfenstein. Neutrino oscillations in matter. *Physical Review D*, 17(9):2369, 1978.

[47] S.P. Mikheev and A. Yu. Smirnov. Resonance enhancement of oscillations in matter and solar neutrino spectroscopy. *Soviet Journal of Nuclear Physics*, 42(6):913–917, 1985.

[48] Y. Fukuda et al. Measurement of the flux and zenith-angle distribution of upward throughgoing muons by super-kamiokande. *Physical Review Letters*, 82(13):2644, 1999.

[49] Q. R. Ahmad et al. Direct evidence for neutrino flavor transformation from neutral-current interactions in the sudbury neutrino observatory. *Physical review letters*, 89(1):011301, 2002.

[50] S. Enomoto et al. First results from kamland: evidence for reactor antineutrino disappearance. *Physical Review Letters*, 90(2):021802, 2003.

[51] M.I. Vysotsky. Lectures on the theory of electroweak interactions. *Physics of Particles and Nuclei Letters*, 8(7):617–650, 2011.

[52] V. L. Ginzburg and L. D. Landau. Zh eksperim, i teor. *Fiz*, 20:1064, 1950.

[53] S.M. Bilenky. Neutrino in standard model and beyond. *Physics of Particles and Nuclei*, 46(4):475–496, 2015.

[54] M. Wurm et al. The next-generation liquid-scintillator neutrino observatory LENA. *Astropart. Phys.*, 35:685–732, 2012.

[55] M. Agostini, A. Formozov, et al. First Simultaneous Precision Spectroscopy of pp, ^{7}Be, and pep Solar Neutrinos with Borexino Phase-II. *arXiv 1707.09279*, 2017.

[56] J. N. Bahcall. The Luminosity constraint on solar neutrino fluxes. *Phys. Rev.*, C65:025801, 2002.

[57] C. Galbiati et al. First evidence of pep solar neutrinos by direct detection in Borexino, 2012.

[58] A. Serenelli, P. Scott, F. L. Villante, et al. Implications of solar wind measurements for solar models and composition, 2016.

[59] C. Pena-Garay and A. Serenelli. Solar neutrinos and the solar composition problem. 2008.

[60] P. C. de Holanda, W. Liao, and A. Yu. Smirnov. Toward precision measurements in solar neutrinos. *Nucl. Phys.*, B702:307–332, 2004.

[61] T. Ohlsson. Status of Non-Standard neutrino Interactions, 2013.

[62] T. Ohlsson. A brief status of Non-Standard neutrino Interactions, 2013.

[63] O. G. Miranda and H. Nunokawa. Non-Standard neutrino interactions: current status and future prospects, 2015.

[64] Z. Berezhiani et al. Vacuum oscillation solution to the solar neutrino problem in standard and nonstandard pictures. *Phys. Rev.*, D51:5229–5239, 1995.

[65] J. Tang and Y. Zhang. Study of nonstandard charged-current interactions at the moment experiment. *Physical Review D*, 97(3):035018, 2018.

[66] J. Kopp et al. Neutrino factory optimization for nonstandard interactions. *Physical Review D*, 78(5):053007, 2008.

[67] J. Kopp et al. Discovery reach for nonstandard interactions in a neutrino factory. *Physical Review D*, 76(1):013001, 2007.

[68] J. Kopp. *New phenomena in neutrino physics*. PhD thesis, 2009.

[69] Edoardo Vitagliano, Javier Redondo, and Georg Raffelt. Solar neutrino flux at keV energies. *JCAP*, 1712(12):010, 2017.

[70] P. Vilain et al. Precision measurement of electroweak parameters from the scattering of muon-neutrinos on electrons. *Phys. Lett.*, B335:246–252, 1994.

[71] John N. Bahcall. Neutrino - Electron Scattering and Solar Neutrino Experiments. *Rev. Mod. Phys.*, 59:505, 1987.

[72] A. Bolanos et al. Probing non-standard neutrino-electron interactions with solar and reactor neutrinos. *Phys. Rev.*, D79:113012, 2009.

[73] Y. Farzan and M. Tortola. Neutrino oscillations and Non-Standard Interactions. 2017.

[74] M. Deniz et al. Constraints on Non-Standard Neutrino Interactions and Unparticle Physics with Neutrino-Electron Scattering at the Kuo-Sheng Nuclear Power Reactor, 2010.

[75] D. Z. Freedman. Coherent effects of a weak neutral current. *Physical Review D*, 9(5):1389, 1974.

[76] J. Liao and D. Marfatia. Coherent constraints on nonstandard neutrino interactions. *Physics Letters B*, 775:54–57, 2017.

[77] Y. Li and Y. Zhou. Shifts of neutrino oscillation parameters in reactor antineutrino experiments with non-standard interactions. *Nuclear Physics B*, 888:137–153, 2014.

[78] M. C. Gonzalez-Garcia et al. New CP violation in neutrino oscillations. *Phys. Rev.*, D64:096006, 2001.

[79] S. Antusch et al. Unitarity of the Leptonic Mixing Matrix. *JHEP*, 10:084, 2006.

[80] G. Bellini et al. Precision measurement of the ^{7}Be solar neutrino interaction rate in Borexino. *Phys. Rev. Lett.*, 107:141302, 2011.

[81] S. T. Petcov and M. Piai. The LMA MSW solution of the solar neutrino problem, inverted neutrino mass hierarchy and reactor neutrino experiments. *Phys. Lett.*, B533:94–106, 2002.

[82] S. Choubey, S. T. Petcov, and M. Piai. Precision neutrino oscillation physics with an intermediate baseline reactor neutrino experiment. *Phys. Rev.*, D68:113006, 2003.

[83] Z. Djurcic, A. Formozov, et al. JUNO Conceptual Design Report. *arXiv: 1508.07166*, 2015.

[84] G. Ranucci. Status and prospects of the juno experiment. In *Journal of Physics: Conference Series*, volume 888, page 012022. IOP Publishing, 2017.

[85] SENSE. Sense - a roadmap for the ideal low light level sensor development is a project funded by the european commission under future and emerging technologies open coordination and support action. `https://www.sense-pro.org/`, 2018. Online; accessed 09-Febraury-2018.

[86] M. Balcerzyk et al. YSO, LSO, GSO and LGSO. A study of energy resolution and nonproportionality. *IEEE Transactions on Nuclear Science*, 47(4):1319–1323, 2000.

[87] F. Capozzi, E. Lisi, and A. Marrone. Neutrino mass hierarchy and precision physics with medium-baseline reactors: Impact of energy-scale and flux-shape uncertainties. *Phys. Rev.*, D92(9):093011, 2015.

[88] O.Yu. Smirnov. Energy and spatial resolution of a large-volume liquid-scintillator detector. *Instruments and Experimental Techniques*, 46(3):327–344, 2003.

[89] S. M Pimblott et al. Energy loss by nonrelativistic electrons and positrons in

polymers and simple solid hydrocarbons. *The Journal of Physical Chemistry B*, 104(41):9607–9614, 2000.

[90] J. Čížek et al. Positron annihilation in flight: experiment with slow and fast positrons. In *Journal of Physics: Conference Series*, volume 505, page 012043. IOP Publishing, 2014.

[91] G. Bellini et al. Final results of Borexino Phase-I on low energy solar neutrino spectroscopy, 2014.

[92] J. B. Birks. *The Theory and Practice of Scintillation Counting: International Series of Monographs in Electronics and Instrumentation*, volume 27. Elsevier, 2013.

[93] V. I. Tretyak. Semi-empirical calculation of quenching factors for ions in scintillators. *Astropart. Phys.*, 33:40–53, 2010.

[94] C. Aberle et al. Light output of double chooz scintillators for low energy electrons. *Journal of Instrumentation*, 6(11):P11006, 2011.

[95] P.A. Cherenkov. Doklady akad. nauk sssr. volume 2, page 451, 1934.

[96] GEANT collaboration. Physics reference manual. *Version: geant4*, 10(9), 2016.

[97] I.E. Tamm and I.M. Frank. Coherent radiation of fast electrons in a medium. In *Dokl. Akad. Nauk SSSR*, volume 14, pages 107–112, 1937.

[98] X.F. Ding et al. Measurement of the fluorescence quantum yield of bis-msb. *Chinese Physics C*, 39(12):126001, 2015.

[99] F. P. An et al. New Measurement of Antineutrino Oscillation with the Full Detector Configuration at Daya Bay. *Phys. Rev. Lett.*, 115(11):111802, 2015.

[100] P. Mosteiro et al. Low-energy (anti)neutrino physics with Borexino: Neutrinos from the primary proton-proton fusion process in the Sun, 2015.

[101] U. K. Akhimov. *Fotonie metodi registrazii izluchenii.* JINR, Dubna, 2006.

[102] D.L. Horrocks. Pulse height-energy relationship of a liquid scintillator for electrons of energy less than 100 keV. *Nuclear Instruments and Methods*, 30(1):157–160, 1964.

[103] F.H. Zhang et al. Measurement of the liquid scintillator nonlinear energy response to electron. *Chin. Phys.*, C39(1):016003, 2015.

[104] C. Dorfer. Characterization of the Nonlinear Light Emission by the Liquid Scintillator Used in the Daya Bay Experiment.

[105] S.V. Bakhlanov et al. A measurement method of a detector response function for monochromatic electrons based on the Compton scattering. *Nuclear Instruments and Methods in Physics Research Section A: Accelerators, Spectrometers, Detectors and Associated Equipment*, 821:13–16, 2016.

[106] Application-Note-AN34. Experiment 7: High-Resolution Gamma-Ray Spectroscopy. New York.

[107] S. Croft and D.S. Bond. A determination of the Fano factor for germanium at 77.4 K from measurements of the energy resolution of a 113 cm^3 HPGe gamma-ray spectrometer taken over the energy range from 14 to 6129 keV. *International journal of radiation applications and instrumentation. Part A. Applied radiation and isotopes*, 42(11):1009–1014, 1991.

[108] R. Dossi, A. Ianni, G. Ranucci, and O. Yu. Smirnov. Methods for precise photoelectron counting with photomultipliers. *Nucl. Instrum. Meth.*, A451:623–637, 2000.

[109] Hamamatsu. Photomultiplier tubes: Basics and applications. *Hamamatsu Photonics KK, Iwata City*, pages 438–0193, 2006.

[110] J. E. Gaiser. Charmonium spectroscopy from radiative decays. Technical report, 1982.

[111] W. R. Leo. *Techniques for nuclear and particle physics experiments: a how-to approach.*

Springer Science & Business Media, 2012.

[112] P. Lombardi, M. Montuschi, A. Formozov, et al. Distillation and stripping pilot plants for the JUNO neutrino detector: design, operations and reliability. *NIM A*, 2019.

[113] D. D'Angelo et al. Recent Borexino results and prospects for the near future. *EPJ Web Conf.*, 126:02008, 2016.

[114] X. Hua-Lin et al. Oxygen quenching in a lab based liquid scintillator and the nitrogen bubbling model. *Chinese Physics C*, 34(5):571, 2010.

[115] JUNO DOCDB 753-v1. *(Internal note)*.

[116] Y. Xu, W. Wang, and Z. Yu. A proposal to evaluate JUNO material radioactive levels using a modified Daya Bay detector. *(DOCDB Internal note)*, 2015.

[117] X. Dongmei. Maximum likelihood reconstruction for the Daya Bay Experiment. 2014.

[118] W. Wu and Z. Yu. Background analysis of replacement LS. *(DOCDB Internal note)*, 2017.

[119] K. Abe et al. Solar Neutrino Measurements in Super-Kamiokande-IV. *Phys. Rev.*, D94(5):052010, 2016.

[120] T. Araki et al. Measurement of neutrino oscillation with KamLAND: Evidence of spectral distortion. *Phys. Rev. Lett.*, 94:081801, 2005.

[121] S. Abe et al. Precision Measurement of Neutrino Oscillation Parameters with KamLAND. *Phys. Rev. Lett.*, 100:221803, 2008.

[122] L. Wolfenstein. Neutrino Oscillations and Stellar Collapse. *Phys. Rev.*, D20:2634–2635, 1979.

[123] S. P. Mikheyev and A. Yu. Smirnov. Resonance Amplification of Oscillations in Matter and Spectroscopy of Solar Neutrinos. *Sov. J. Nucl. Phys.*, 42:913–917, 1985. [,305(1986)].

[124] S. P. Mikheev and A. Yu. Smirnov. Resonant amplification of neutrino oscillations in matter and solar neutrino spectroscopy. *Nuovo Cim.*, C9:17–26, 1986.

[125] Michele Maltoni and Alexei Yu. Smirnov. Solar neutrinos and neutrino physics. *Eur. Phys. J.*, A52(4):87, 2016.

[126] Marco Pallavicini et al. Solar neutrino detectors as sterile neutrino hunters. *J. Phys. Conf. Ser.*, 888(1):012018, 2017.

[127] Francesco Capozzi, Ian M. Shoemaker, and Luca Vecchi. Solar Neutrinos as a Probe of Dark Matter-Neutrino Interactions. *JCAP*, 1707(07):021, 2017.

[128] Rouven Essig, Mukul Sholapurkar, and Tien-Tien Yu. Solar Neutrinos as a Signal and Background in Direct-Detection Experiments Searching for Sub-GeV Dark Matter With Electron Recoils. *Phys. Rev.*, D97(9):095029, 2018.

[129] G. Alimonti et al. The Borexino detector at the Laboratori Nazionali del Gran Sasso. *Nucl.Instrum.Meth.*, A600:568–593, 2009.

[130] G. Bellini et al. Final results of Borexino Phase-I on low energy solar neutrino spectroscopy. *Phys. Rev.*, D89(11):112007, 2014.

[131] C. Arpesella et al. Direct Measurement of the Be-7 Solar Neutrino Flux with 192 Days of Borexino Data. *Phys. Rev. Lett.*, 101:091302, 2008.

[132] John N. Bahcall and Roger K. Ulrich. Solar Models, Neutrino Experiments and Helioseismology. *Rev. Mod. Phys.*, 60:297–372, 1988.

[133] John N. Bahcall, M. H. Pinsonneault, and Sarbani Basu. Solar models: Current epoch and time dependences, neutrinos, and helioseismological properties. *Astrophys. J.*, 555:990–1012, 2001.

[134] Sanjib Kumar Agarwalla and Patrick Huber. Potential measurement of the weak mixing angle with neutrino-electron scattering at low energy. *JHEP*, 08:059, 2011.

[135] Ivan Esteban, M. C. Gonzalez-Garcia, Michele Maltoni, Ivan Martinez-Soler, and Thomas Schwetz. Updated fit to three neutrino mixing: exploring the accelerator-reactor complementarity. *JHEP*, 01:087, 2017.

[136] F. Capozzi, E. Lisi, A. Marrone, D. Montanino, and A. Palazzo. Neutrino masses and mixings: Status of known and unknown 3ν parameters. *Nucl. Phys.*, B908:218–234, 2016.

[137] S. Zavatarelli. Krypton/Thoron/Radon . *(Borexino DOCDB Internal note)*, 2017.

[138] X.F. Ding. Poissonian Kr penalty. *(Borexino DOCDB Internal note)*, 2017.

[139] G. Bohm and G. Zech. *Introduction to statistics and data analysis for physicists*. DESY, Hamburg, 2014.

[140] J. N. Abdurashitov et al. Measurement of the solar neutrino capture rate with gallium metal. III: Results for the 2002–2007 data-taking period, 2009.

[141] J. N. Abdurashitov et al. Measurement of the solar neutrino capture rate with gallium metal. *Phys. Rev.*, C60:055801, 1999.

[142] J. N. Bahcall. Gallium solar neutrino experiments: Absorption cross-sections, neutrino spectra, and predicted event rates. *Phys. Rev.*, C56:3391–3409, 1997.

[143] V. N. Gavrin and B. T. Cleveland. Radiochemical solar neutrino experiments. *Nucl. Phys. Proc. Suppl.*, 221:90–97, 2011.

[144] V. A. Kuzmin. Detection of solar neutrinos by means of the 71Ga(nu, e-)71Ge reaction. *Sov. Phys. JETP*, 22:1051–1056, 1966. [Zh. Eksp. Teor. Fiz.49,1532(1965)].

[145] M. Agostini et al. Limiting neutrino magnetic moments with Borexino Phase-II solar neutrino data. *Phys. Rev.*, D96(9):091103, 2017.

[146] A. Bolanos, O. G. Miranda, A. Palazzo, M. A. Tortola, and J. W. F. Valle. Probing non-standard neutrino-electron interactions with solar and reactor neutrinos. *Phys. Rev.*, D79:113012, 2009.

[147] Oleg Smirnov. Solar neutrino from pp-chain and other results of Borexino, June 2018.

[148] Carlo Giunti and Alexander Studenikin. Neutrino electromagnetic interactions: a window to new physics. *Rev. Mod. Phys.*, 87:531, 2015.

[149] Robert E. Shrock. Electromagnetic Properties and Decays of Dirac and Majorana Neutrinos in a General Class of Gauge Theories. *Nucl. Phys.*, B206:359–379, 1982.

[150] Kazuo Fujikawa and Robert E. Shrock. Magnetic moment of a massive neutrino and neutrino-spin rotation. *Phys. Rev. Lett.*, 45:963–966, Sep 1980.

[151] G Bellini, J Benziger, S Bonetti, M Buizza Avanzini, B Caccianiga, L Cadonati, F Calaprice, C Carraro, A Chavarria, A Chepurnov, et al. Study of solar and other unknown anti-neutrino fluxes with borexino at lngs. *Physics Letters B*, 696(3):191–196, 2011.

[152] G. Salamanna. Solar, supernova, atmospheric and geo neutrino studies using JUNO detector. *PoS*, ICHEP2016:1239, 2017.

[153] G. Salamanna. Solar neutrinos with the JUNO experiment. In *5th International Solar Neutrino Conference Dresden, Germany, June 11-14, 2018*, 2018.

[154] B. S. Wonsak et al. Topological track reconstruction in unsegmented, large-volume liquid scintillator detectors. *JINST*, 13(07):P07005, 2018.

[155] M. Grassi, A Formozov., et al. Charge reconstruction in large-area photomultipliers. *Journal of Instrumentation*, 13(02):P02008, 2018.

[156] M. Agostini, A. Formozov, et al. Comprehensive measurement of the solar neu-

trino spectrum from the proton-proton nuclear fusion chain with Borexino. *Nature*, 2018.

[157] A. Formozov, G. Bellini, et al. Constraints on Non-Standard Neutrino Interactions from Borexino Phase-II. *Journal of High Energy Physics (in preparation)*, 2018.

[158] A. Formozov. The measurement of liquid scintillator nonlinear response and intrinsic energy resolution. *ICPPA-2018 proceedings; (peer review)*, 2018.

[159] A. Formozov et al. The measurement of nonlinear responce and intrinsic energy resolution for low energy electrons in linear alkylbenzene. *JINST (in preparation)*, 2019.

[160] M. Agostini, A. Formozov, et al. Improved measurement of ^{8}B solar neutrinos with 1.5 kt y of Borexino exposure. *arXiv preprint arXiv:1709.00756*, 2017.

[161] A. Formozov. On the role of radiative losses in energy scale of large liquid scintillator and water Cerenkov detectors. *arXiv, 1808.07458*, 2018.

[162] A. Formozov, S. Agarwalla, and C Sun. The Study of Non-Standard Interactions With Borexino. *Presented at: Recent developments in neutrino physics and astrophysics*, September 2017.

List of Publications

Refereed publications

M. Agostini, A. Formozov, et al. The Monte Carlo simulation of the Borexino detector. *Astropart. Phys.*, 97:136–159, 2018

M. Grassi, A Formozov., et al. Charge reconstruction in large-area photomultipliers. *Journal of Instrumentation*, 13(02):P02008, 2018

M. Agostini, A. Formozov, et al. Comprehensive measurement of the solar neutrino spectrum from the proton-proton nuclear fusion chain with Borexino. *Nature*, 2018

P. Lombardi, M. Montuschi, A. Formozov, et al. Distillation and stripping pilot plants for the JUNO neutrino detector: design, operations and reliability. *NIM A*, 2019

Publications in preparation

A. Formozov, G. Bellini, et al. Constraints on Non-Standard Neutrino Interactions from Borexino Phase-II. *Journal of High Energy Physics (in preparation)*, 2018

A. Formozov. The measurement of liquid scintillator nonlinear response and intrinsic energy resolution. *ICPPA-2018 proceedings; (peer review)*, 2018

A. Formozov et al. The measurement of nonlinear responce and intrinsic energy resolution for low energy electrons in linear alkylbenzene. *JINST (in preparation)*, 2019

Preprints

Z. Djurcic, A. Formozov, et al. JUNO Conceptual Design Report. *arXiv: 1508.07166*, 2015

M. Agostini, A. Formozov, et al. Improved measurement of ^{8}B solar neutrinos with 1.5 kt y of Borexino exposure. *arXiv preprint arXiv:1709.00756*, 2017

M. Agostini, A. Formozov, et al. First Simultaneous Precision Spectroscopy of *pp*, ^{7}Be, and *pep* Solar Neutrinos with Borexino Phase-II. *arXiv 1707.09279*, 2017

A. Formozov. On the role of radiative losses in energy scale of large liquid scintillator and water Cerenkov detectors. *arXiv, 1808.07458*, 2018

Posters

A. Formozov, S. Agarwalla, and C Sun. The Study of Non-Standard Interactions With Borexino. *Presented at: Recent developments in neutrino physics and astrophysics*, September 2017

Acknowledgments

This work could not be possible without the collaborative effort of many people. Foremost, I would like to express my sincere gratitude to my supervisors, Lino Miramonti, Oleg Yu. Smirnov and Alexander G. Olshevskiy, for their advisement in a large amount of both scientific and personal problems. Without their support and guidance, I would never achieve the altitude at which I've found myself right now.

I cannot express enough thanks to my reviewers: Bayarto K. Lubsandorzhiev for inspiration in low-light detection and PMT-instrumentation, his sharp critique and comments, and Franceso Vissani for a very close x-ray look through the text, remarks and encouragement in doing science. I did my best to improve the quality of the manuscript.

I would like to say *Grazie mille* to the whole Milano group: to Emanuela Meroni for her great support in the laboratory activities, data analysis and vivid discussions, Gioacchino Rannuci in many aspects of science and project management, Gianpaolo Bellini for the opportunity to work on NSI and his review of the results, Davide Basilico and Alessandra Re for being supportive and great co-workers, Marco Giammarchi for the art of asking questions, Irene Bolognino, Davide D'Angelo, David Bravo, Silvia Caprioli and Laura Collica for wonderful working atmosphere, Paolo Lombardi for providing full access to the lab as well as Augusto Brigatti, Sergio Parmeggiano for great working days, Paolo Saggese for assistance with computing issues, and Ruben Pompilio for the fundamental support and showing the beauty of engineering. Comments on the present work and publication provided by Barbara Caccianiga were profound and invaluable. I appreciate Silvia Rognoni for her always kind attitude. Also, I appreciated discussions with Vito Antonelli and with Marco Torri on various things in neutrino physics and modern science in general. I also appreciate the wonderful opportunity provided by Lorenzo Caccianiga to show to young generation what is going on in experimental particle physics right now. I had got a unique experience working together with all of you.

I can not avoid acknowledging the fundamental contribution that was made by people from Joint Institute for Nuclear Research, Dubna, especially by the analysis group of Oleg Yu. Smirnov and his team: Alina Vishneva, Maxim Gromov, Kirill Fomenko, Denis Korablev, Albert Sotnikov as well as other people from Dzelepov Laboratory of Nuclear Problems: Maxim Gonchar, Nikolay V. Anfimov, Tatiana A. Antoshkina and Dmitry V. Naumov. I also should express my attitude to Fabio Mantovani, Marica Baldoncini, Giovanni Fiorentini, Michele Montuschi, Barbara Ricci and Virginia Strati from beloved Ferrara group, and Monica Sisti and Davide Chiesa from the University of Milano-Bicocca. I would like to acknowledge the friendship and support I have re-

ceived from Yury Malyshkin, Stefano M. Mari, Cristina Martellini, Giulio Settanta and say *spasibo* to Giuseppe Salamanna from Roma Tre.

I want to thank Oleg Yu. Smirnov for inspiring me to measure the intrinsic energy resolution and the group of Milan for serious support of my effort. I would like to point out at the significant contribution of Charles University and personally thank Vit Vorobel and Viktor Pec, Rupert Leitner, Tadeas Dohnal for their progress in the measurement of the scintillator non-linearity, broad interest and for the enthusiasm to collaborate. I also appreciate TUM's Hans Theodor Josef Steiger and Lothar Johann Nikolaus Oberauer for useful discussions and competitive atmosphere. The big role was played by the group of St. Petersburg Nuclear Physics Institute, especially by Ilia Drachnev and Alexander Derbin. I received great feedback from Jülich group: Yaping Cheng, Christoph Genster, Michaela Schever and Livia Ludhova. Thanks to Marco Grassi for the discussion on non-linearity measurement with a cup of coffee and Mariangela Settimo for providing PMT samples. Thanks to Salvatore Costa and Arseniy V. Rybnikov for a great time during PMT-testing in China. I want to emphasize the achievements of Elia Cavallé in our lab during his Triennale thesis.

Regarding liquid scintillator purification activity, I would like to thank again Paolo Lombardi and his team, including people from Milan as well as Jari Joutsenvaara, Wilfried Depnering and Alessandro Mengucci. Understanding the chemical properties of the scintillator was not possible without Fausto Ortica from Dipartimento di Chimica, Biologia e Biotecnologie, Perugia, and Igor B. Nemchenok, from JINR, Dubna. The co-working with Chinese colleagues, especially in the group of Tao Hu, Li Zhou and Yu Boxiang, was extraordinarily productive and enlightening in many intercultural aspects. We highly appreciated their hospitality. The collaboration with Zeyuan Yu on liquid scintillator radiopurity studies was priceless for me.

I would like to thank Tatsu Takeuchi, Sanjib Kumar Agarwalla and Chen Sun for a lot of hard collaborative work and discussions on NSI's. It was an exceptional opportunity. I am also thankful to Zurab Berezhiani for the discussion at the initial stage of the research and giving a perspective on beyond Standard Model physics. Thanks to Mariia Redchuk, Zara Bagdasarian, Ömer Penek, Sindhujha Kumaran for providing support in the analysis and always a great time together; Bedrich Roskovec for the review of a presentation and discussion on the role of NSI's. I benefited tremendously from the help of XueFeng Ding, Simone Marcocci and Nicola Rossi. I am very much thankful to Daniele Guffanti for looking at the manuscript and several suggestions, and to Chiara Ghiano for her hospitality in Gran Sasso and help underground. I.N.F.N. Genova played a big role in the analysis and review of the results, namely: Alessio Caminata, Marco Pallavicini, Gemma Testera and Sandra Zavatarelli. Suggestions of Aldo Ianni and Igor Machulin on $\sin^2\theta_W$ measurement were very useful. Thanks to Marcin Misiaszek for critique of the theoretical aspects of the work and Björn Wonsak, David Meyhöfer, Henning Rebber and Caren Hagner for their kind welcome in Hamburg and guidance at the ultimate stage of the work. Thanks to Andrea Pocar for his particular interest and the review.

I express my gratitude to the whole Borexino and JUNO collaborations for the provided opportunities. It was a great pleasure to work with all of you, bright and extraordinary people.

I would like to honor the memory of Raju S. Raghavan [6], one of the Founding Fathers of the Borexino experiment, for inspiration and showing how to do innovation in science.

I appreciate the financial support received from INFN (Borsa di studio per neolaureati) and the University of Milan (Borsa di studio dottorato di ricerca). The work was

---

[6] In Memory of Raju Raghavan, (1937-2011)

partially supported by RFBR grant 17-02-00305A and Humboldt-Research Fellowship for Experienced Scientists.

The significant role in setting up the doctorate was done by Andrea Zanzani and Doctorate School's directors Francesco Ragusa and Matteo Paris in the University of Milan. Besides, I would like to thank Olga V. Fotina, International (represented by Natalia N. Nikiforova) and Doctorate offices in Lomonosov Moscow State University and Vladimir V. Leontiev, Natalia P. Smirnova and Izabella F. Vdovina from SINP MSU, Dubna for their strong administrative guidance and support.

Finally, I would like to thank my parents and sister, close friends and beloved Sara for their unlimited support. They always believe in me.